Universiteit Utrecht

MSc THESIS

Comparison of the domain-state-corrected multispecimen method with the microwave and Thellier-Thellier methods using historical lavas from La Palma, Spain

MARILYN MONSTER

Supervised by:
L.V. de Groot, MSc
Dr. M.J. Dekkers
Prof.dr. C.G. Langereis

17th of August, 2011

Comparison of the domain-state-corrected multispecimen method with the microwave and Thellier-Thellier methods using historical lavas from La Palma, Spain

Author:	Marilyn Wilhelmina Leonora Monster
Student number:	3482472
E-mail:	m.w.l.monster@gmail.com M.W.L.Monster@students.uu.nl
Supervisors:	L.V. de Groot, MSc Dr. M.J. Dekkers Prof.dr. C.G. Langereis
Faculty:	Geosciences, Utrecht University
Section:	Palaeomagnetism
Research carried out at:	Paleomagnetic Laboratory 'Fort Hoofddijk' Budapestlaan 17 3584 CD Utrecht The Netherlands
Date:	17th of August, 2011

Front page: The 1949 lava flow (western branch) at La Palma flowing from the crater all the way to the ocean. Photograph taken by Lennart de Groot.

ABSTRACT

Reliable palaeointensities (PIs) are necessary to determine the full vector variation of Earth's magnetic field as a function of geological time and hence to provide constraints for geodynamo models. Knowledge of PIs also has implications for cosmic abundance ratios, as the strength of Earth's magnetic field influences the amount of radiation entering the atmosphere. Most current palaeointensity determination methods are based on the classic Thellier-Thellier protocol. These protocols are usually fairly laborious and are characterised by rather low success rates.

A new method of determining palaeointensities was proposed by Dekkers and Böhnel in 2006. This 'multispecimen parallel differential pTRM method' (MSP-DB) is based on the linearity of pTRM with inducing field, a property that is independent of domain state. It uses multiple specimens to ensure that all specimens have experienced the same magnetic history. However, especially for intermediate grain sizes the MSP-DB protocol seems to overestimate palaeointensities. For this reason, Fabian and Leonhardt (2010) proposed a new, domain-state-corrected protocol (MSP-DSC), which uses three additional steps in comparison to the original DB protocol to isolate the overprinted pTRM, make an estimate of the domain state and detect alteration. Both the MSP-DB and the DSC protocols were tested on historical lavas from La Palma and compared to Thellier-Thellier and microwave results obtained using the Aitken protocol and pTRM checks.

Nine flows were sampled, including the 1949 and 1971 flows, which were sampled at five and three sites respectively. These 20th-century flows are particularly important, as their PI results can be compared to IGRF values. Palaeomagnetic directions determined using thermal and alternating-field demagnetisation for the 20th-century sites were within error of their IGRF values. All samples were within the pseudo-single-domain (PSD) range, but their hysteresis ratios varied widely, from close to the single-domain (SD) range to very near the multi-domain (MD) range. Curie temperatures varied from 80 to 540 ^{o}C, showing a lot of variation between sites within one flow and between different flows.

When applying the MSP-DB protocol, the three 20th-century sites with high Curie temperatures (540 °C) all yielded PI underestimates within 10% of the IGRF value, whereas the sites with low (135 °C) to very low (80 °C) Curie temperatures yielded large under- or overestimates (up to 50%), perhaps fortuitously. The overestimates were reduced considerably by the MSP-DSC protocol, but were still quite high. Underestimates were some times corrected upward, usually related to a reduction in scatter. The Thellier-Thellier method yielded technically acceptable plots for ten out of fifteen sites. Two of the 20th-century sites failed, three yielded large underestimates (up to 27%) and three sites yielded results within 10% of the IGRF value. The microwave method yielded acceptable results for nine out of thirteen measured sites. Three of the 20th-century sites failed, the other five yielded results within 12% of the IGRF values.

Comparing results from the three different methods indicates that if two or three methods agree to within a few percent, the obtained PI is close to the actual PI. For sites for which the three methods do not agree, the microwave method yielded the best results. Plotting the obtained PIs against time shows a lower PI (38 μT) 1.09 kyr ago and a decrease from 44 μT in 1585 to 38-41 μT for the 20th-century sites.

CONTENTS

LIST OF FIGURES

LIST OF TABLES

LIST OF ABBREVIATIONS

AF	Alternating field
DC	Direct current
IEF	Intensity error fraction: $\text{IEF} = \frac{\text{calculated PI - IGRF}}{\text{IGRF}}$
IGRF	International Geomagnetic Reference Field
IZZI	In-field/zero-field, zero-field/in-field; protocol used in Thellier-type experiments
MD	Multi-domain
MSP	Multispecimen protocol
MSP-DB	Multispecimen protocol, Dekkers-Böhnel
MSP-DSC	Domain-state-corrected multispecimen protocol
MSP-FC	*f*-corrected multispecimen protocol
NRM	Natural remanent magnetisation
PI	Palaeointensity
PSD	Pseudo-single domain
pTRM	Partial thermoremanent magnetisation
SD	Single domain
SQUID	Superconducting quantum interference device
TRM	Thermoremanent magnetisation
UTM	Universal Transverse Mercator coordinate system

1 INTRODUCTION

To determine the full vector variation of Earth's magnetic field as a function of geological time, we need to know how the intensity of the field varied in the past. These palaeointensities (PIs) could tell us, for example, if there is a relation between reversal frequency and the strength of the geomagnetic field. Retrieving these PIs, however, is not straightforward.

In the classic Thellier-Thellier method (Thellier and Thellier, 1959), a rock's natural remanent magnetisation (NRM) is progressively replaced by a set of laboratory partial thermoremanent magnetisations (pTRM) to successively higher temperatures in a known field. Lower-temperature steps can be repeated to verify that the specimen's ability to acquire a thermal remanence has not changed due to alteration (e.g. Tauxe, *Essentials*). Because of the large number of steps, the Thellier-Thellier method is fairly laborious. A variation on the Thellier-Thellier method is the microwave method, in which high-frequency microwaves are used to directly excite the magnetic spin systems within the magnetic grain, instead of heating the whole bulk sample as in the classic Thellier-Thellier method. Because the bulk sample experiences less heating, alteration during the experiment should be reduced (e.g. Hill and Shaw, 2007).

A different method of determining PIs was proposed by Dekkers and Böhnel (2006). This 'multispecimen parallel differential pTRM method' (MSP-DB) is based on the linearity of pTRM with inducing field, a property that is independent of domain state. As long as no alteration occurs, it should be suitable for all magnetic grains. To ensure all samples have the same magnetic history, each sample undergoes just one treatment. An ancient TRM is overprinted by an artificial pTRM pointing in the same direction as the TRM at a single low measurement temperature, which must be higher than the highest demagnetising temperature of the viscous component.

Experiments using this method on synthetic samples and Icelandic and Mexican lavas showed that this method is very promising and in some cases yields better results than the classic Thellier-Thellier method (e.g. Dekkers and Böhnel, 2006; Böhnel *et al*., 2009; Michalk *et al*., 2008). However, it has one big problem: it seems to systematically overestimate palaeointensities, especially for intermediate-sized grains (e.g. Michalk *et al*, 2010).

Fabian and Leonhardt (2010) proposed a protocol to estimate and correct this overestimation (MSP-DSC, where DSC is short for 'domain-state-corrected'). This protocol uses three additional steps per specimen compared to MSP-DB, in which the overprinted pTRMs are isolated, an estimate of the domain state is made, and chemical or magnetic alteration is detected. These extra steps do cause a potential problem: whereas in the MSP-DB method all samples undergo just one treatment, which ensures they have the same magnetic history, this is not the case for the MSP-DSC method. Application of this new protocol on synthetic samples seems to indicate that the MSP-DSC protocol reduces the overestimate and data scatter.

The aim of my MSc project was to apply these three different methods of determining PIs — Thellier-Thellier, microwave and multispecimen — to real samples and compare their results. Cores were drilled at La Palma, one of the Canary Islands. The sampled lava flows include two that are within the range of the International Geomagnetic Reference Field (IGRF), so that it was possible to compare the calculated PIs with the intensity values

from the reference field. Chapters 2 and 3 describe the geological setting and sampling. Preliminary analyses were carried out before the PI experiments; methods and results can be found in sections 4.1 and 4.2, respectively. The PI experiments are described in Chapter 5. Results from Chapters 4 and 5 are discussed in Chapter 6, starting with possible sources of error, followed by a discussion of the PI experiments themselves. My results are summarised in Chapter 7. Finally, the appendices contain Curie diagrams, susceptibility-versus-temperature diagrams and NRM decay curves for all sites and all PI results. Appendix VI gives more information on the Scilab code I wrote to process the multispecimen data.

2 GEOLOGICAL SETTING[1]

The Canary Islands are a chain of oceanic volcanic islands off the coast of Morocco. They rest on Jurassic oceanic lithosphere and were generated by magmatic processes related to a hotspot fixed under a plate slowly progressing eastward. (**Fig. 2.1**.)

Except for Fuerteventura and Lanzarote, each island forms an independent edifice. As illustrated by **fig. 2.2**, these edifices developed on increasingly deep ocean floor. The eastern islands — Lanzarote-Fuerteventura, Gran Canaria — and La Gomera are deeply eroded, whereas Tenerife is at its peak of volcanic growth and the two westernmost islands — La Palma and El Hierro — are still in the juvenile stage of development.

Fig. 2.2 also highlights an important change that occurred after the formation of La Gomera: the east-west trending single line of volcanic islands seems to have split into a north-south trending dual line, with La Palma and El Hierro developing contemporaneously.

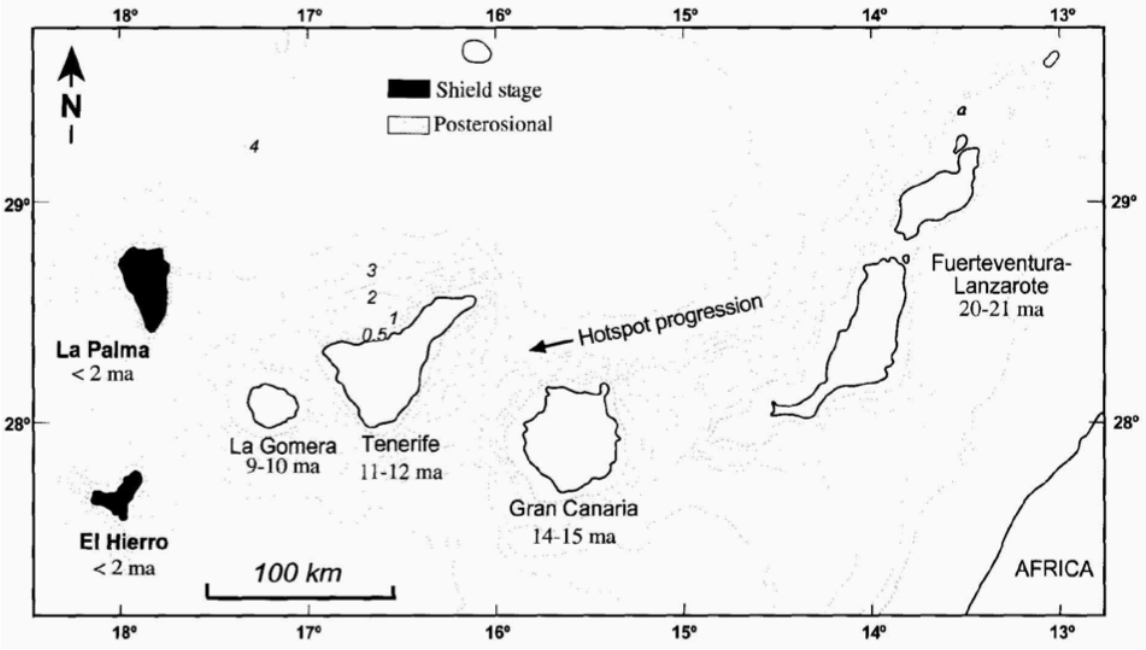

Fig. 2.1 Map of the Canary Island, showing the progression of the hotspot relative to the plate and the oldest ages for the emerged volcanism. (Carracedo et al., 2001)

La Palma is the fifth largest (706 km^2) and second highest (2,423 m above sea level) of the Canaries and is located on the M25 magnetic anomaly. It is elongated in the north-south direction and is made up of two main polygenetic stratovolcanoes: the conical northern shield and the elongated Cumbre Vieja volcano at the southern part of the island. A saddle separates the two volcanoes, forming the Valle de Aridane depression.

Rainfall is relatively high (up to 900 mm in the summit areas), leading to high erosion rates that have caused deep barrancos in the northern shield. Compared to some tropical oceanic islands, however, the rainfall is low, which means the island is less vegetated and rock outcrops are abundant and fresh.

[1] A detailed description of the geology and volcanology of La Palma can be found in Carracedo et al. (2001).

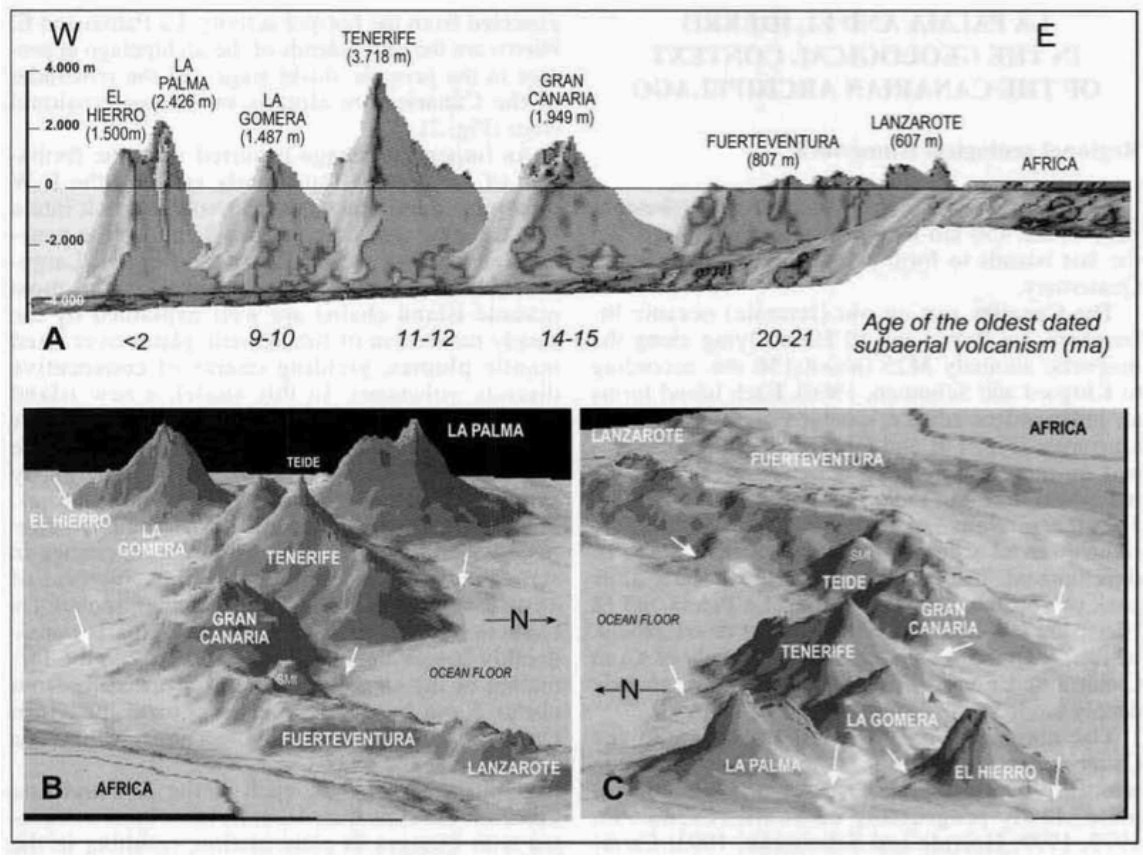

Fig. 2.2 Computer-generated 3-D images of the Canary Islands. (Carracedo *et al*., 2001) A) Cross section showing age against height of the different islands. B) Views from the east and west of the archipelago.

In the development of the island, several stages can be distinguished. A submarine volcanic seamount formed during the Pliocene and was uplifted up to 1,500 m by intense magmatic and dyke intrusions. Between 1.77 and 1.20 Ma the Garafía volcano was built to a height of ~2,500-3,000 m. The south flank collapsed at about 1.20 Ma in a gravitational landslide, due to rapid growth and progressive instability.

The Taburiente volcano was built by the eruptive activity following this collapse and filled the landslide depression. From about 0.78 Ma (the Matuyama-Brunhes boundary), volcanism was increasingly concentrated in three rifts (northwest, northeast and north-to-south) and subsequently in a central edifice at the geometrical centre of the volcanic shield. Of these three rifts, the southern Cumbre Nueva rift was more developed than the other two and formed a north-south trending ridge. As the rift grew, it became progressively more unstable, culminating in a gravitational landslide of the western flank at about 560 ka, which formed the Valle de Aridane depression. Around this time, incision and retrogressive erosion began to form the Caldera de Taburiente. Both the rift and the caldera are clearly visible in the satellite image shown in **fig. 2.3**.

After the collapse, most of the volcanic activity in the northern shield was concentrated in the interior of the new collapse basin, where the Bejenado stratovolcano formed rapidly. About 0.4 Myr ago, the activity of the northern shield ceased and volcanism moved to the new Cumbre Vieja volcano at the south of the island. The summit of the Cumbre Vieja consists of a row of eruptive vents and fissures, which form a north-south trending rift zone. According to Carracedo (2001), this rift will most likely develop in a similar way to

the Cumbre Nueva rift that preceded it: progressively developing and becoming increasingly unstable. Faults generated by the 1949 eruption have been interpreted as possible detachment of the western flank of the volcano, leading to wild speculation that the western part of La Palma could drop into the ocean any time and cause a devastating tsunami.[2] This, however, seems unlikely.[3]

I mainly sampled historical flows and some sub-recent ones (≤ 3.2 ka), which all originate from the Cumbre Vieja volcano, the only active volcano during the past 123 kyr. Most of the eruptions of the Cumbre Vieja volcano are Strombolian and phreato-Strombolian he Cumbre Vieja lavas are from the alkali series. The bulk of the sequence is formed by very homogeneous basalts (Carracedo *et al*., 2001).

Fig. 2.3 Satellite image of La Palma (from Google Maps), clearly showing the Caldera de Taburiente and the north-south trending Cumbre Nueva rift.

[2] E.g. this article in *The Independent* (1996): "Science: Lethal shockwave from an island in the sun" (http://www.independent.co.uk/news/science/science-lethal-shockwave-from-an-island-in-the-sun-1338618.html) or "Mega-tsunami: wave of destruction", featured in BBC's *Horizon* broadcast on 12 October 2000.

[3] E.g. Carracedo et al. (2001); Mader (2001); Keulemans (2006). For a collection of evidence against a La Palma tsunami, see e.g. La Palma Tsunami (http://www.lapalma-tsunami.com).

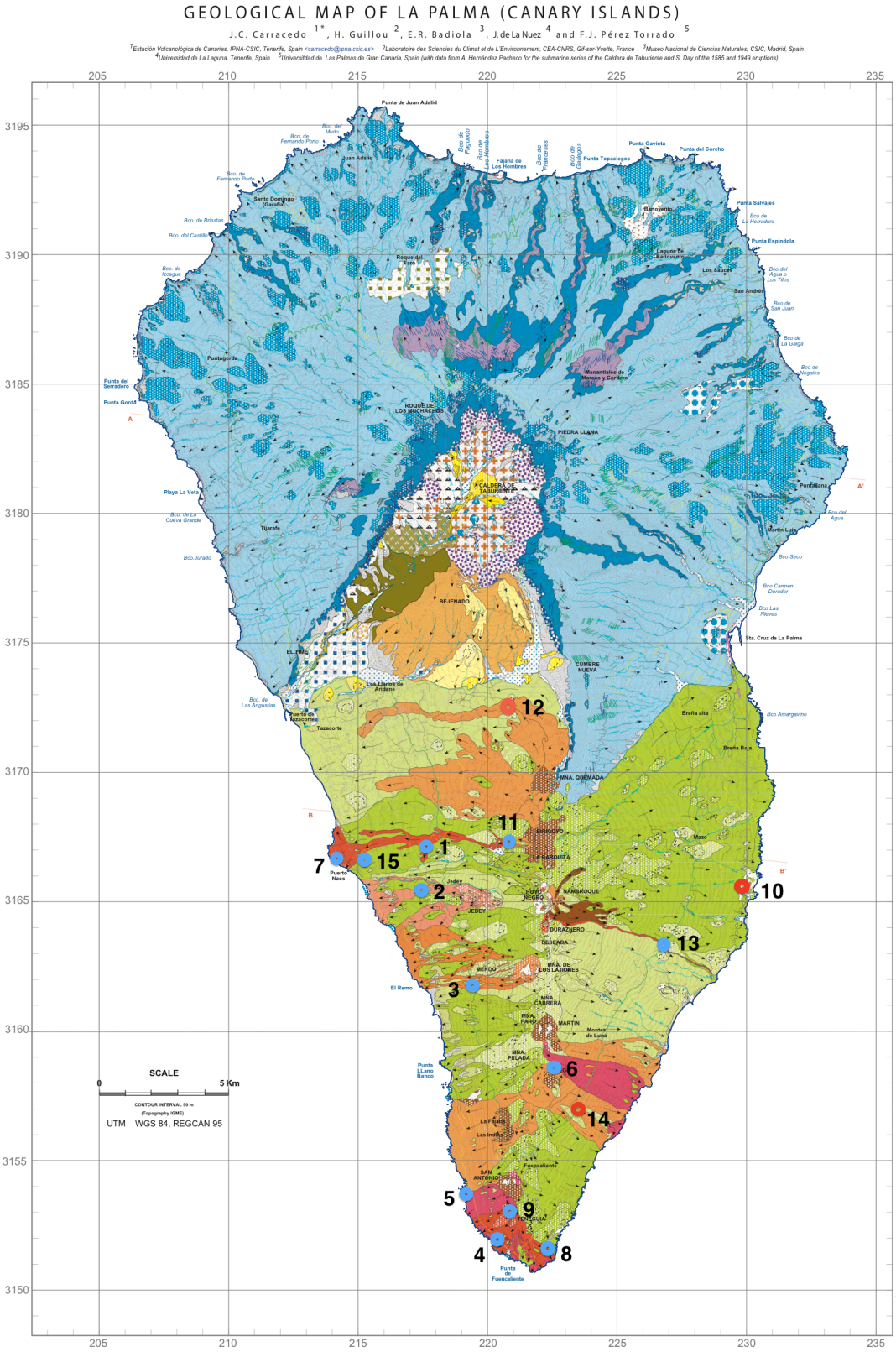

Fig. 2.4 Geological map of La Palma (adapted from Carracedo *et al*.). Sampling locations are indicated by dots: blue for historical flows and red dots for carbon-dated flows. Site numbers are indicated next to the dots.

3 SAMPLING

Fieldwork was carried out on La Palma, one of the Canary Islands. Ages and locations of the sampled sites are summarised in **table 3.1**. For each site, at least 14 cores of one-inch (2.54 cm) diameter were drilled using a water-cooled petrol-powered drill. Cores were numbered and orientated. Declination and inclination of the core were measured relative to an arrow drawn on the core (see **fig. 3.1**) using an orientation device. Cores were usually drilled near the top of the flow and in solid parts of the flow. For site 4 (1971, west), cores were drilled in three rows (see **fig. 3.2**) to assess the influence of cooling rate, which is different for varying distances from the top of the lava flow.

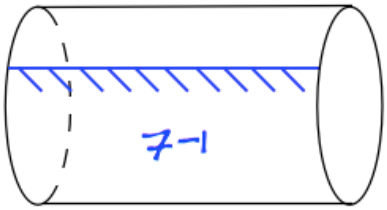

Fig. 3.1 Cores were marked and numbered and orientated relative to the arrow. The arrow is pointing into the rock.

The flows were so magnetic that in some cases the declination measured using a magnetic compass showed a significant deviation. For this reason, declinations were — if possible — also measured using a solar compass. Using these declinations and the exact time and location of the measurement, the declination of a core could be determined using the program `sundec.exe`. Deviations of up to 20° were observed. The solar compass could not be used at site 8 (1971, east) and for several samples at sites 7 (1949, sea) and 9 (1971, crater) because they were in the shadows.

The flows exhibiting such strong magnetisation raises a another potential problem: a lava flow may not only have been influenced by the Earth's magnetic field at the time of emplacement but also by the field generated by underlying older flows. According to Valet and Soler (1999), who measured the total magnetic field above the surface of 12 lava flows on La Palma and Tenerife, directions can differ by up to 15% and intensity changes may even reach 20%, depending on the location above the flow. These deviations are linked to topographic features at the surface of the flows. To assess the influence of these processes, the two flows within the IGRF range were sampled at multiple locations. The three rows drilled at site 4 (1971, west) allow to assess the effect of the crustal field, which would be expected to be largest near the lower surface of the flow.

Fig. 3.2 Photograph of site 4 (1971, west), showing the three drilling rows.

Table 3.1 Site numbers, coordinates and associated ages. Ages AD, except for sites 10 and 14, which were carbon-dated. Ages from Carracedo et al (2001). E.g. Klügel et al. (1999) give 1430-40 AD as age for site 12. Coordinates were measured in the Universal Transverse Mercator (UTM) system and converted to latitude and longitude using RCN Utilities & Tools[1] (Montana University and Yellowstone National Park). Interesting characteristics or drilling conditions are noted.

Site number	Age	UTM	Lat. (°N)	Long. (°W)
1	1949	28R 0217622 UTM 3167203	28.6011	-17.8875
	A'a flow.			
2	1585	28R 0217376 UTM 3165247	28.5834	-17.8895
3	1712	28R 0219413 UTM 3161779	28.5526	-17.8679
	Near an overhead power line.			
4	1971	28R 0220339 UTM 3151984	28.4645	-17.8560
	Drilled in three rows at varying distances from the top of the flow.			
5	1677	28R 0219204 UTM 3153723	28.4799	-17.8680
6	1646	28R 0224141 UTM 3158590	28.5248	-17.8188
7	1949	28R 0213892 UTM 3166897	28.5975	-17.9255
	Difficult drilling conditions: unstable footing. Very close to the ocean.			
8	1971	28R 0222053 UTM 3151531	28.4607	-17.8384
	Solar compass readings could not be obtained.			
9	1971	28R 0220881 UTM 3153047	28.4742	-17.8507
	Very soft, vesicular rock. Cores broke easily and were difficult to mark. Solar compass readings could not be obtained for all cores.			
10	1.09 ± 0.05 ka (C-14)	28R 0229806 UTM 3165709	28.5902	-17.7627
	Very vesicular samples, which broke easily and were difficult to mark. Very little material. Samples drilled at two locations, about 2.5 m apart.			
11	1949	28R 0220775 UTM 3167210	28.6018	-17.8553
12	1470-92 (C-14)	28R 0220737 UTM 3172548	28.6499	-17.8570
13	1949	28R 0226832 UTM 3163391	28.5687	-17.7925
14	3.2 ± 0.01 ka (C-14)	28R 0223341 UTM 3156914	28.5094	-17.8266
	Location from Carracedo et al. (1999) ambiguous; drilling site chosen based on characteristics of the lava (tephraic).			
15	1949	28R 0215216 UTM 3166630	28.5954	-17.9119

[1] http://www.rcn.montana.edu/resources/tools/coordinates.aspx?nav=11&c=UTM&md=83&mdt=NAD83/WGS84&z=28&e=0215216&n=3166630&h=N

4 PRELIMINARY ANALYSES

Rock magnetic, thermal and palaeomagnetic analyses were carried out prior to the PI experiments to assess the chemical composition and the magnetic properties of the different sites. For example, knowing alteration temperatures — the temperature at which the sample's magnetic properties change — is of prime importance, because they provide a maximum temperature that can be used in Thellier-Thellier and multispecimen experiments.

4.1 Methods

4.1.1 Alternating-field demagnetisation

The robotised 2G DC SQUID (superconducting quantum interference device) magnetometer at Fort Hoofddijk is used for AF demagnetisation. In AF demagnetisation, an oscillating field is applied to a specimen in a magnetically shielded environment (residual field in the order of nT). The rationale behind of AF demagnetisation is that components with short relaxation times τ (i.e. low stability remanence components) also have low coercivities. The grain moments with coercivities below the peak AF will track the field. As the peak field gradually decays, these 'unblocked' moments will be stuck; half of them along one direction of the AF and half along the other direction, which means their net contribution to the remanence will be zero.

The robotised set-up can take up to 96 specimens at one time, which are processed in about 24 hours. These specimens are glued into cubes, which are placed in twelve rows of eight samples. The robot places eight specimens on a tray, step-wise demagnetises them using an alternating field in three directions and measures them in three orthogonal positions (e.g. x_1, x_2 and x_3) using a DC SQUID magnetometer.

For each site, about ten specimens of 1 inch (2.54 cm) diameter and length 1 to 1.5 cm were AF demagnetised. The results were corrected for the drilling direction and plotted in Zijderveld diagrams, in which the vector magnetisation is projected onto two orthogonal planes (e.g. Dunlop, 1979). It was assumed that the lavas were in their original positions when they were sampled, which means that their stratigraphic coordinates are equal to their geological coordinates. If available, core declinations determined using a solar compass are preferred. This was impossible for site 8 (1971, east) and several cores drilled at sites 7 (1949, sea) and 9 (1971, crater). Site 8 was corrected by adding the average difference between magnetic and solar compass readings for site 4 (1971, west), which was +3.9°. Sites 7 and 9 were corrected using the average correction found cores that could be oriented using a solar compass, i.e. +1.7 for site 7 and +17.9 for site 9. Using the computer program `Paldir.exe`, directions were determined from the obtained Zijderveld diagrams. Plotting the NRM-normalised scalar magnetisation against temperature yielded AF NRM decay curves.

4.1.2 Thermal demagnetisation

Samples were thermally demagnetised by placing them in a field-free oven and heating them to progressively higher temperatures. Fort Hoofddijk has got two ovens for thermal

demagnetisation, one of which can be used with an applied DC field for PI experiments. The aim is to keep the samples at the desired temperature for at least 10 minutes, which translates to putting the samples in the oven for 40 to 50 minutes, depending on the temperature. Samples were cooled in the oven using a fan. Depending on the maximum temperature, cooling down to 30°C took between 20 and 30 minutes. The vector magnetisation of samples was measured using a SQUID magnetometer.

For most sites three specimens were thermally demagnetised at 100, 140, 180, 220, 260, 300, 340, 380, 440, 500, 530, 560 and 720°C. For site 4, two specimens per drilling row were thermally demagnetised. Magnetite with some titanium has a Curie temperature of about 540°C; at 720°C (nearly) everything should be demagnetised, including haematite.

As in AF demagnetisation, the vector magnetisation — corrected for the specimen's declination and inclination — was plotted in Zijderveld diagrams and directions determined using `Paldir.exe`. Plotting the NRM-normalised scalar magnetisation against temperature yielded thermal NRM decay curves.

4.1.3 Curie balance

The Curie temperature T_c of a specimen, which is the temperature above which spontaneous magnetisation ceases, can be determined using a Curie balance. Fort Hoofddijk's Curie balance takes small amounts (generally 10-20 mg) of specimen ground into small pieces, which are placed in a glass sample holder and covered by some glass wool to couple it to the holder, which is inserted into the Curie balance horizontally.

The sample is placed near the pole piece of a strong electromagnet and is pulled in by the field gradient. This force is counteracted with a restoring force of equal magnitude by a voice coil. The current required to keep the specimen stationary is proportional to its magnetisation. The output of the voice coil is plotted against temperature, while the sample is heated to successively higher temperatures (up to 720 °C) and then cooled back to room temperature (e.g. Tauxe, *Essentials*). T_c is determined using the 'intersecting tangent method' (e.g. Grommé *et al*., 1969), as illustrated in **fig. 4.1a**.

The Curie balance at Fort Hoofddijk can also be used to determine the temperature at which a specimen alters chemically due to heating T_{alt}. This is done by cycling back to a lower temperature before increasing the temperature again. If alteration has occurred, the magnetisation as a function of temperature when cycling to a lower temperature will be different from the magnetisation measured when the sample was heating up. A good example for this is shown by the Curie diagram of Site 7, see **Appendix I**. **Fig. 4.1a-b** show the intersecting tangents method of determining the Curie temperature of a specimen and an example of strong alteration made visible by cycling back to lower temperatures.

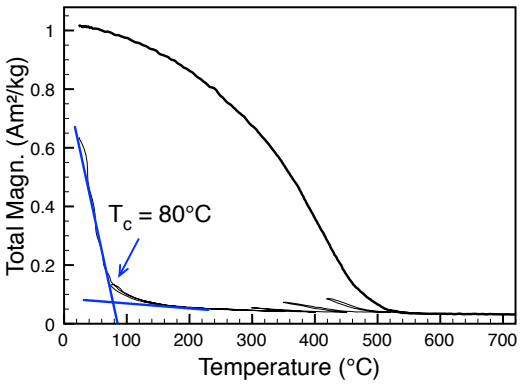

Fig. 4.1a The intersecting tangent method of determining T_c.

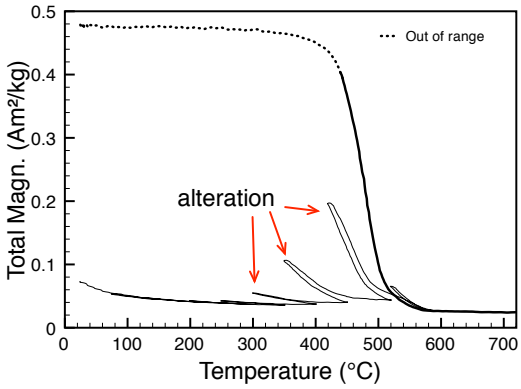

Fig. 4.1b Chemical alteration, as made visible by cycling to successively higher temperatures. The flatness of the highest part of the cooling curve indicates that the specimen's magnetisation went out of range (dashed line).

4.1.4 Kappabridge

Susceptibility-versus-temperature diagrams can be measured using a Kappabridge. (KLY-3). Magnetic susceptibility is defined as the ratio of the induced magnetisation to an inducing magnetic field, i.e. it is a measure of the magnetic response of a material to an applied magnetic field. In the Kappabridge, such a field is produced by a coil that also serves as a sensor. It compares the electronic characteristics of the circuit with and without the specimen in the coil. The magnetic susceptibility of the specimen is determined from the change. Susceptibility can be measured as a function of temperature by placing the specimen in a heating coil. When the Curie temperature is reached, the specimen will only exhibit paramagnetic susceptibility and its susceptibility will drop inversely with temperature. (E.g. Hunt, 1994; Tauxe, *Essentials*.)

The Kappabridge uses very low fields (~300 A/m) and measures the initial susceptibility: it assesses the 'elasticity' of magnetisation. Like the Curie balance, the Kappabridge cycles to progressively higher temperatures and then back to 50°C. It takes several grammes of finely ground specimen. Measuring an empty sample holder revealed an offset of -163 in the measured susceptibility, for which the measurements were corrected.

4.1.5 MicroMag

The MicroMag is an alternating gradient force magnetometer (AGM) and can be used to measure hysteresis loops and back-field curves for small specimens (chips of 1-10 mg). From the hysteresis loop, the coercive field H_c, the saturation remanent magnetisation M_r and the saturation magnetisation M_s can be determined (**fig. 4.2a**); from the back-field curve the coercivity of remanence H_{cr} can be determined (**fig. 4.2b**). The ratios M_r/M_s and H_{cr}/H_c are sensitive to remanence state and the source of magnetic anisotropy and thus give information about grain size and shape. The two ratios can be plotted against each other in a Day plot, which is used to assess domain state. Day plots are divided into regions of

nominally single-domain (SD), pseudo-single-domain (PSD) and multi-domain (MD) behaviour (Day, Fuller and Schmidt, 1977).

Before the actual measurements, the MicroMag was calibrated using a calibration sample of pure nickel with a known saturation magnetic moment of 571 μemu. Results were normalised by mass, and a slope correction and a correction for pole saturation were applied. For all sites, three to six samples were measured, depending on the amount of scatter in the data. All sites were measured prior to heating; sites that showed relatively little scatter were also measured after heating to the temperature used in the MSP experiment to assess whether heating has a noticeable effect on the domain state. As the specimens are heated to a temperature below their chemical alteration temperature, changes in domain state could be important in explaining discrepancies between the calculated PI and the expected PI from the IGRF.

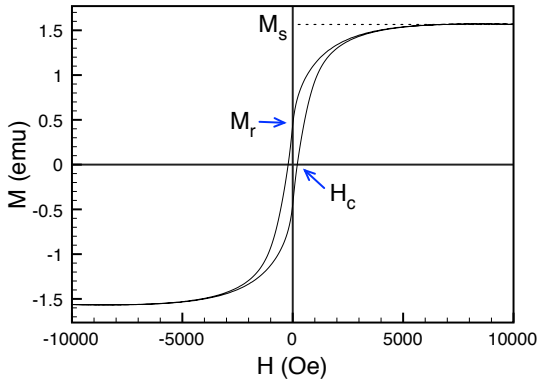

Fig. 4.2a Hysteresis loop showing the parameters M_s, M_r and H_c.

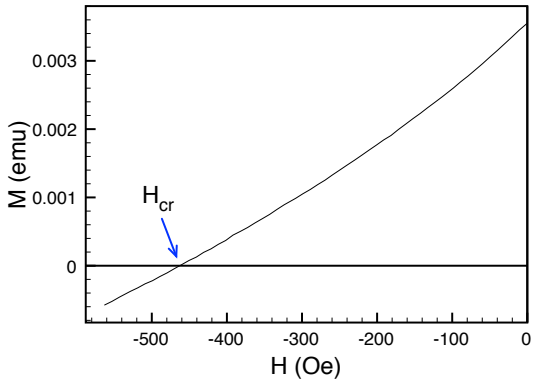

Fig. 4.2b Back-field curve showing the parameter H_{cr}.

4.2 Results

4.2.1 Demagnetisation

For all sites except site 4, between 7 and 12 specimens were AF demagnetised. For site 4, 16 specimens were AF demagnetised. Zijderveld diagrams (**fig. 4.3**) for the AF demagnetisation show no overprint at all, or small overprints that are removed by 5 mT. The diagrams show linear demagnetisation behaviour of the NRM toward the origin. AF NRM decay curves (**figs. A1.1-15c**) show varying behaviour between sites. In most cases, specimens within one site show very similar behaviour (e.g. **fig. 4.4a**), but sites 3, 9 and 12 — and to a lesser extent sites 6 and 10 — show quite a lot of within-site scatter (e.g. **fig. 4.4b**). For sites 6, 10 and 12 the shapes of the curves are very similar, suggesting that a different normalisation (e.g. by weight instead of NRM) may improve the results. At an AF field of 100 mT, the NRM is generally reduced to about 10-15% of the initial NRM value, with the exception of sites 7 (< 5%), 9 (5-30%), 12 (20-40%) and 14 (about 20%).

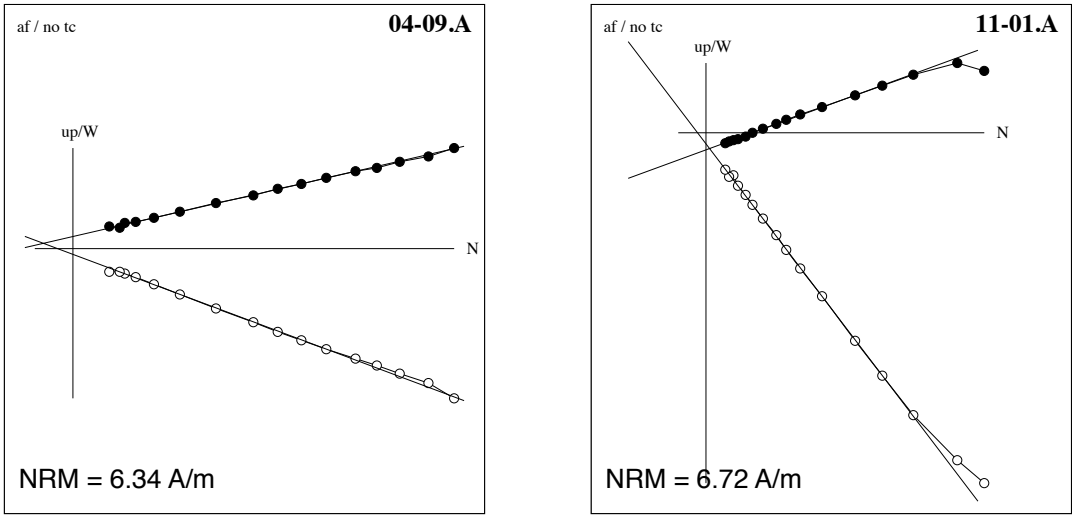

Fig. 4.3 Two representative AF demagnetisation curves. *Left:* Site 4 (1971, west). *Right:* Site 11 (1949, crater) shows a small overprint, which is removed by 5 mT. Steps: 2.5, 5, 7.5, 10, 15, 20, 25, 30, 40, 50, 60, 70, 80, 90 and 100 mT.

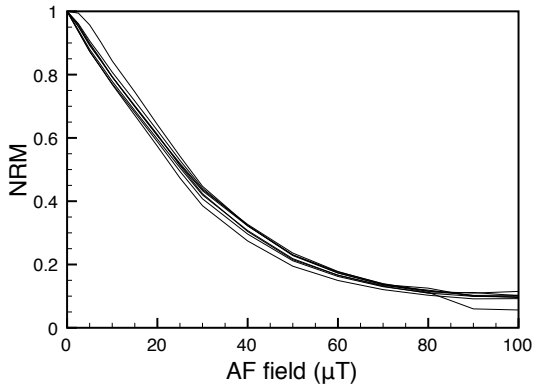

Fig. 4.4a AF NRM decay curve for site 2 (1585), which shows very homogeneous behaviour.

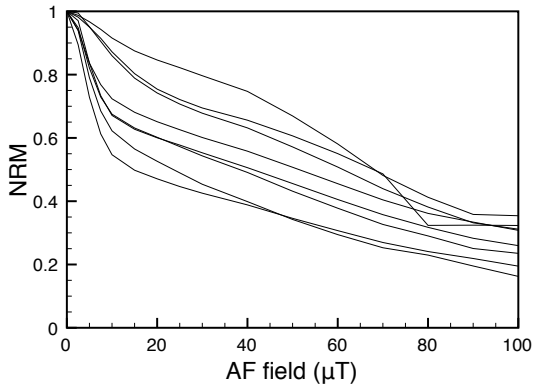

Fig. 4.4b AF NRM decay curve for site 12 (1470-92). The plot shows a substantial amount of within-site variation, but the shapes of the curves are similar.

For all sites, 3 specimens were thermally demagnetised, with the exception of site 4, for which 2 specimens per drilling row were thermally demagnetised. Results were plotted in Zijderveld diagrams (**fig. 4.5**). Because the specimens were measured manually, scatter is larger than in the AF Zijderveld diagrams, which makes it more difficult to detect small, low-temperature overprints. Another problem is that even though the specimens were less than half of the standard specimen size, a number of specimens — mainly those of sites 2, 3, 6, 9, 10, 11 and 12 — were so magnetic, that the DC SQUID magnetometer went out of range. Because of this, several or in some cases nearly all temperature steps could not be measured. Nevertheless, for all sites except sites 2 and 9, at least one specimen could be measured and directions determined from the Zijderveld diagrams.

Thermal NRM decay curves (**figs. A1.1-15b**) are generally homogeneous within one site, but show very different behaviour between different sites. Site 11's NRM, for example, decreases sharply until at 200°C only 10-20% of its NRM is left (**fig. 4.6a**). Site 10, on the other hand, retains > 80% of its NRM at a temperature of 350°C, after which its magnetisation rapidly decreases. NRM intensities are in the order of 1-10 A/m. For all sites, the NRM is reduced to < 10% (usually even < 5%) at 560°C. In some NRM decay curves, alteration is visible as a temporary increase in magnetisation as the temperature increases. Site 7 (**fig. A1.7b**) is the best example of this. **Fig. 4.5** (right) shows a Zijderveld diagram of site 7, in which the alteration manifests as partial self-reversal: the NRM increases during a few temperature steps before decreasing again towards the origin (indicated by the blue arrows).

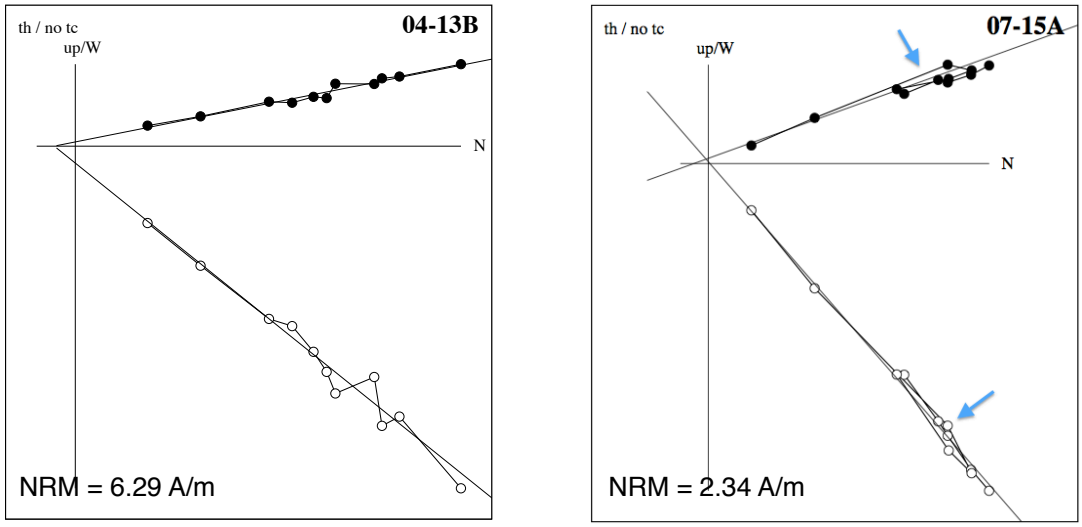

Fig. 4.5 Two thermal demagnetisation curves. *Left:* Site 4 (1971, west). *Right:* Site 7 (1949, sea) shows remagnetisation (indicated by the arrows), associated with the strong alteration visible in the Curie and Kappabridge diagrams. Steps: 100, 140, 180, 220, 260, 300, 340, 380, 440, 500, 530, 560 and 720°C.

Directions were determined from the AF and thermal demagnetisations. In general, directions obtained from AF and thermal demagnetisations were consistent, see e.g. **fig. 4.7a-c**. Directions obtained for the 20th-century flows were compared with directions from the IGRF (**figs 4.8** and **4.9**) and were found to be consistent to within a few degrees. The substantial scatter observed for site 7 (1949, sea) may have been caused by the difficult

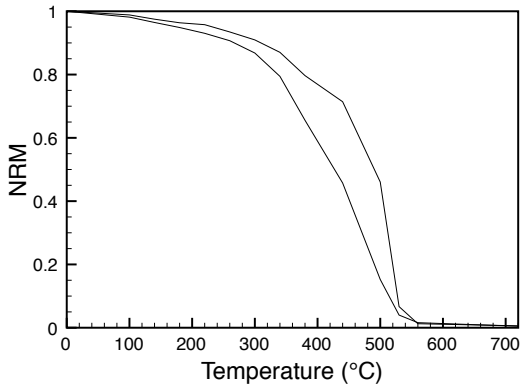

Fig. 4.6a Thermal NRM decay curve for site 10 (1.09 ± 0.05 ka), which retains > 80% of its NRM at a temperature of 350°C.

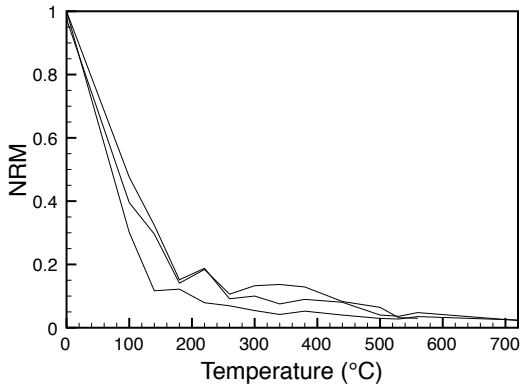

Fig. 4.6b Thermal NRM decay curve for site 11 (1949, crater), which has lost most of its NRM at 100°C.

drilling conditions. Specimens from site 9 were very vesicular, making it difficult to see the markings and thus contributing to the fairly large scatter in the results.

Fig. 4.10 shows the average directions and their α_{95} confidence intervals for all sites and the IGRF for La Palma at present, as summarised in **table 4.1**. The average directions obtained for the two 17th-century flows (1646 and 1677) are close together, as was to be expected. Site 2 (1585) is very close to the two 17th-century flows in both declination and inclination. Site 3 (1712), on the other hand, has the same inclination (54°) as site 5 (1677), but its declination differs by 20°. Site 3 was located near an overhead power line, which may have been an influence.

Another possible influence may be that the rocks themselves are very magnetic: declinations obtained using a magnetic compass and using a solar compass can differ up to 20°. These large differences are in agreement with work by Valet and Soler (1999), which indicates that directions measured above the surface of lava flows at La Palma and Tenerife may differ by up to 15°. These deviations are linked to topographic features at the surface of the flows. Therefore, it is not unlikely that newly deposited lava flows are not only influenced by Earth's magnetic field, but also by the field generated by the lava flows below it.

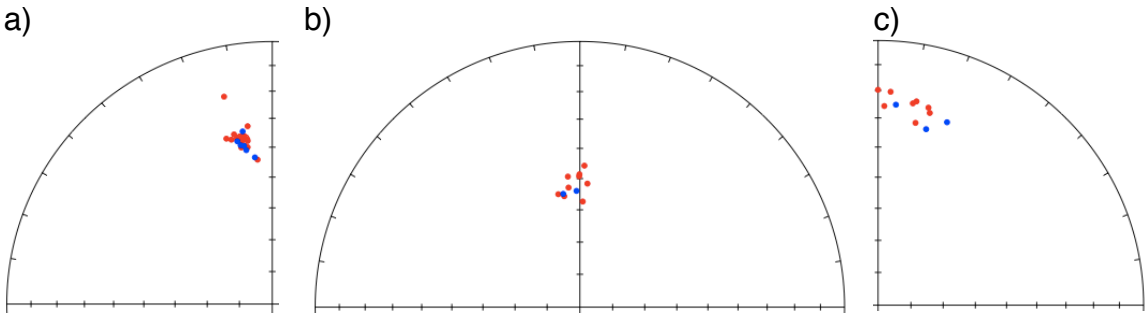

Fig. 4.7 Equal area plots showing declinations and inclinations obtained through AF (red symbols) and thermal (blue symbols) demagnetisation for **a)** site 4 (1971, west), **b)** site 6 (1646) and **c)** site 12 (1470-1492). In general, directions obtained through thermal and AF demagnetisation are consistent.

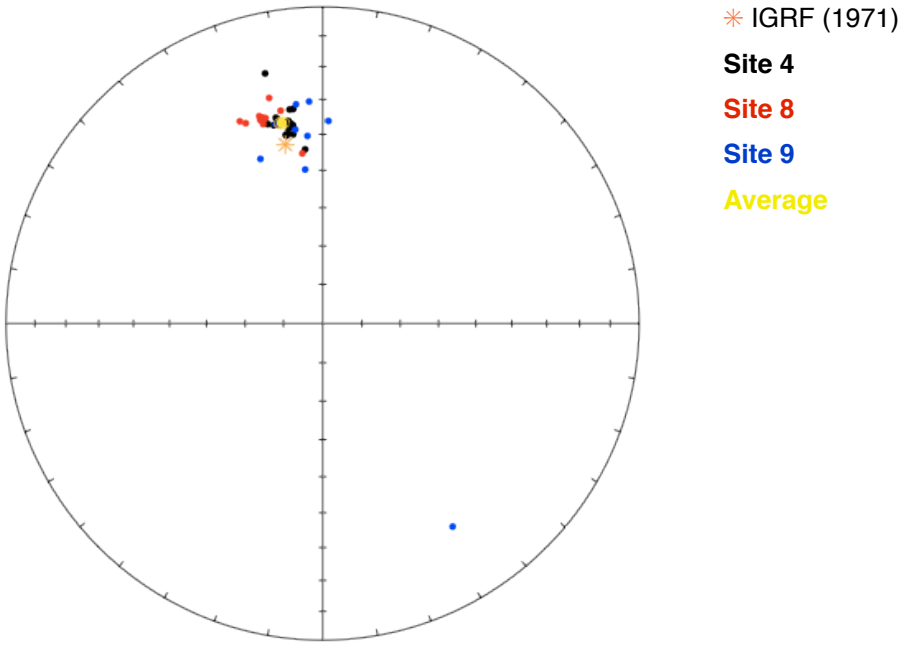

Fig. 4.8 Directions obtained from all 1971 sites using AF and thermal demagnetisation. The average direction and its α_{95} are shown in yellow; the IGRF value for 1971 is indicated by the orange asterisk. The obtained directions are fairly consistent with the IGRF value. The outlier (site 9) was probably aligned

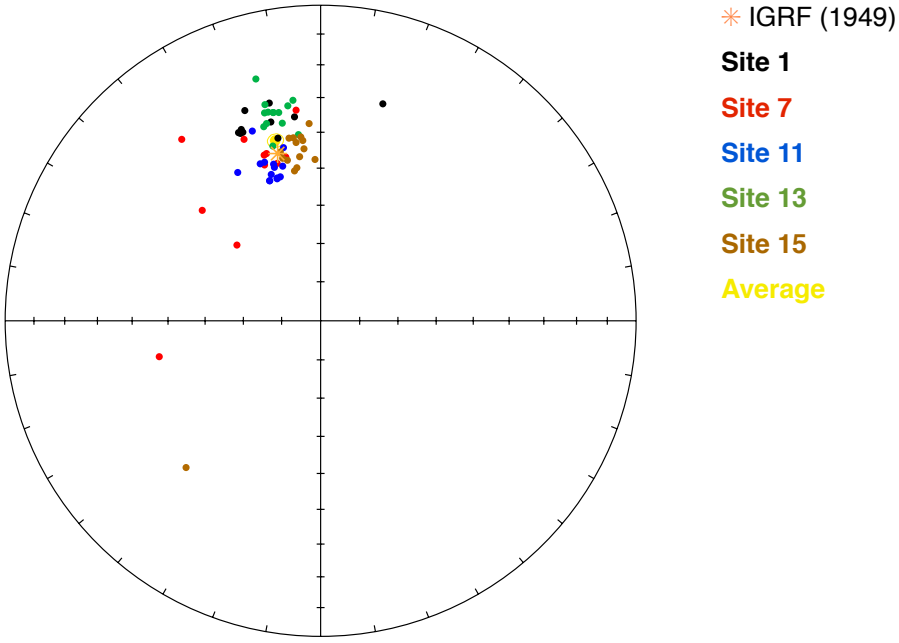

Fig. 4.9 Directions obtained from all 1949 sites using AF and thermal demagnetisation. The average direction and its α_{95} are shown in yellow; the orange asterisk indicates the IGRF value for 1949. Especially site 7 shows a lot of scatter — possibly caused by the difficult drilling conditions — but in general the directions obtained are fairly consistent with the IGRF value.

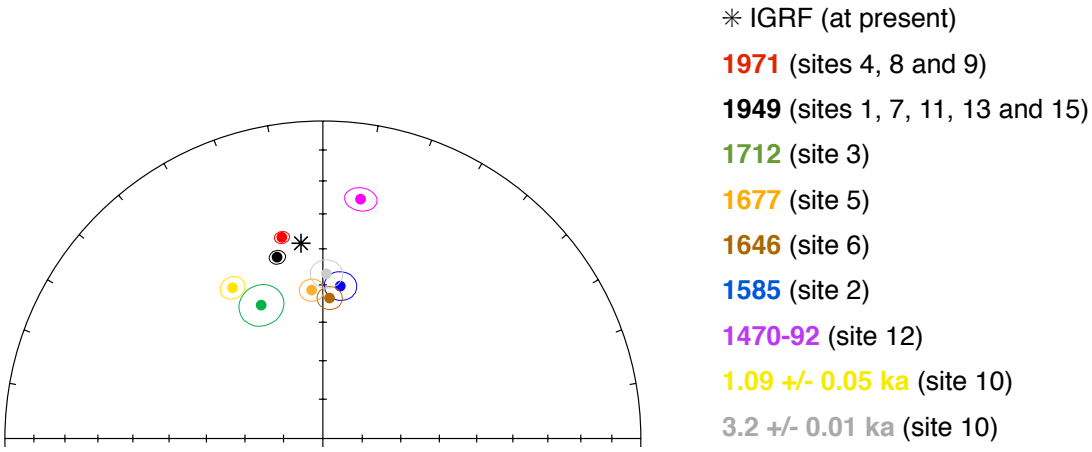

Fig. 4.10 Average directions (based on AF and thermal demagnetisation) and their α_{95} intervals. The black asterisk indicates the current IGRF value of the field direction at La Palma.

Table 4.1 Directions obtained from AF and thermal demagnetisation. Site 8 (1971, east) and part of site 9 (1971, crater) could not be oriented using a solar compass. Results marked 'm' were obtained using magnetic compass readings; results marked 'c' were obtained using a correction (see **Section 4.1.1**). Values in degrees.

	IGRF		**Measured**			
Site	**Dec**	**Inc**	**Dec**	**Inc**	**α_{95}**	**N**
1 (1949)	345.5	45.6	345.8	35.1	9.2	10
2 (1585)	-	-	6.4	49.0	5.3	8
3 (1712)	-	-	333.7	54.0	3.5	11
4 (1971)	348.1	41.8	349.4	35.5	2.4	21
5 (1677)	-	-	359.7	54.0	3.5	11
6 (1646)	-	-	357.5	51.6	3.1	10
7 (1949)	345.5	45.6	333.2	40.8	22.4	11
8 (1971) m	348.1	41.8	267.5	32.4	5.7	11
8 (1971) c	348.1	41.8	346.5	32.2	2.2	11
9 (1971) m	348.1	41.8	352.9	39.5	14.4	6
9 (1971) c	348.1	41.8	355.3	37.0	7.9	6
10 (1.09 ka)	-	-	328.7	44.4	3.7	10
11 (1949)	345.5	45.6	342.1	49.0	1.5	14
12 (1470-92)	-	-	8.2	24.1	4.3	11
13 (1949)	345.5	45.6	347.0	32.2	3.0	14
14 (3.2 ka)	-	-	1.3	46.5	5.4	11
15 (1949)	345.5	45.6	351.3	45.6	2.2	14

4.2.2 Curie and alteration temperatures

Measurements on a Curie balance (magnetisation-versus-temperature) yield information on both T_c and T_{alt}, as illustrated by **fig. 4.9** for sites 4 (1971, west) and 11 (1949, crater). These two sites represent the two main groups that can be distilled from the Curie diagrams: one group that, like site 4, shows a more or less linear decay (broad spectrum) and a high T_c (540°C) and one group that, like site 11, shows a very low T_c (80-135°C), indicating high Ti content. An 'intermediate group' (T_c of 200 to 475°C) consisting of sites 3, 10, 12 and 14 can also be discerned. Curie diagrams for all sites can be found in **Appendix I** (**figs A1.1-15a**).

Cycling the temperature allows to assess the reversibility of the signal. Substantial changes in the signal for the same temperatures during a cycle are indicative of chemical alteration (e.g. **fig. 4.11** and **fig. A1.7a**). Eight sites first show chemical alteration between 300 and 350°C, three sites between 350 and 400°C, one site (site 7) between 200 and 250°C and for site 14 no alteration is visible at all in its Curie diagram. **Table 4.2** shows alteration and Curie temperatures for all sites. As the actual T_{alt} is within an interval, the alteration temperatures given in **table 4.2** represent the highest temperature that is certainly 'safe', i.e. no chemical alteration occurs below that temperature.

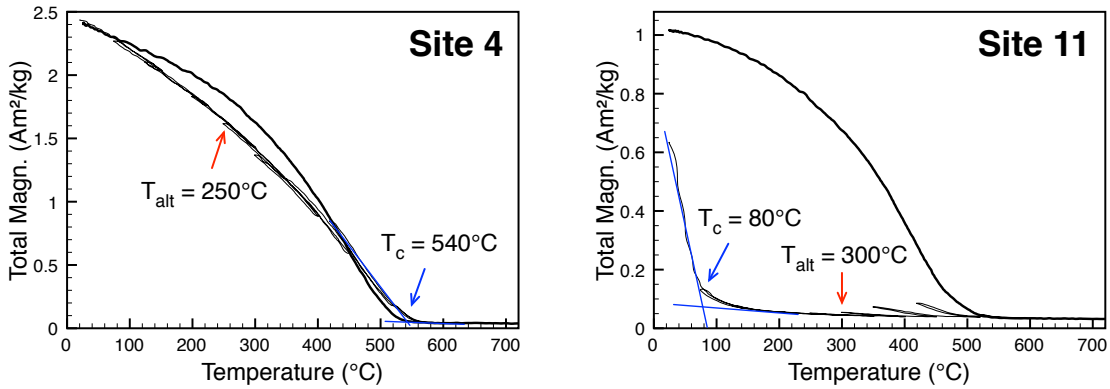

Fig. 4.11 Curie balance plots of two representative sites. *Left:* Site 4 (1971 flow), broad spectrum and high T_C. *Right:* Site 11 (1949 flow), very low T_C.

Alteration temperatures can also be assessed using susceptibility-versus-temperature diagrams, using a Kappabridge. This was done for sites for which the alteration temperature could not clearly be discerned in the Curie diagrams. However, most of the plots did not show a clear alteration temperature. A slight downgoing trend with each cycle can be observed (e.g. **fig. 4.12**, left), but this is caused by drift of the equipment. Alteration and Curie temperatures from the susceptibility-versus-temperature diagrams can be found in **table 4.3**; the diagrams themselves can be found in **Appendix II**. To be on the safe side, the lowest alteration temperatures indicated by either the Curie diagrams or the Kappabridge measurements were used to determine the set-temperatures for the MSP experiments. Curie temperatures measured using the Kappabridge generally agreed with those measured on the Curie balance, except for site 3, whose values differ by 80°C.

Table 4.2 Alteration and Curie temperatures. The alteration temperatures in the table represent the highest temperature below which no alteration occurs; the actual alteration temperature cannot be pinpointed exactly but lies in a temperature range, e.g. 300-350°C for site 2.

Site	T_{alt} (°C)	T_c (°C)
1 (1949)	350	540
2 (1585)	300	540
3 (1712)	300	210
4 (1971)	300	540
5 (1677)	250	120
6 (1646)	300	540
7 (1949)	200	90
8 (1971)	300	135
9 (1971)	300	540
10 (1.09 ka)	350	475
11 (1949)	300	80
12 (1430)	300	280
13 (1949)	250	100
14 (3.2 ka)	> 500	370
15 (1949)	250	90

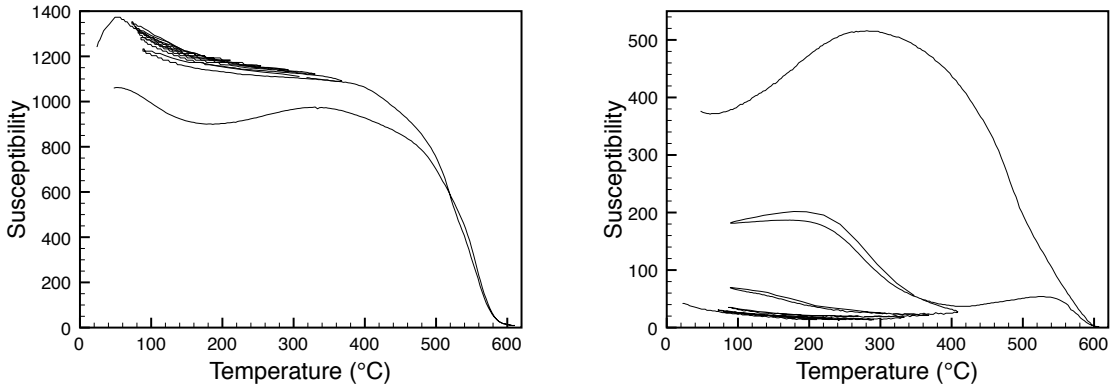

Fig. 4.12 Susceptibility-versus-temperature plots. *Left:* Site 4 (1971, west) shows alteration between 320-360°C and a Curie temperature of ~ 500°C. *Right:* Site 7 (1949, sea) shows strong alteration when cycling back from 320°C.

Table 4.3 Alteration temperatures from susceptibility-versus-temperature diagrams.

Site	T_{alt} (°C)	T_c (°C)
1 (1949)	360-600	~ 500
2 (1585)*	unclear	unclear
3 (1712)*	360-600	~ 120
4 (1971)	320-360	~ 500
7 (1949)	280-320 (possibly 240-280)	< 100
13 (1949)	320-360	unclear
14 (3.2 ka)	360-600	~ 350

* Measurement incomplete because of a technical malfunction.

Measurements on the Curie balance and the Kappabridge showed widely varying behaviour between sites, even between those from the same lava flow, e.g. the western part of the 1949 flow (sites 1, 7, 11 and 15). The 1949 eruption can be divided into different phases: until July 10 Llano del Banco erupted tephritic a'a lava, but from July 10 onwards, basanites were erupted, most of which was carried directly to the sea. (Klügel *et al*., 1999.) Site 1 was located in a'a lava, whereas sites 7 and 15 were located near the sea, which explains the differences between site 1's Curie diagram on the one hand and those of sites 7, 11 and 15 on the other hand.

4.2.3 MicroMag

The hysteresis loops and back-field curves show pseudo-single-domain behaviour for all sites. The values of the hysteresis parameters vary widely between sites, some times even within one flow, as shown by the large standard deviations in **table 4.4**. varying from 0.036 ± 0.011 Am^2/kg (site 7, 1949) to 2.8 ± 0.68 Am^2/kg (site 1, 1949). For all sites, the average hysteresis ratios M_r / M_s and H_{cr} / H_c were plotted against each other in a Day plot (**fig. 4.13**). The error bars show the standard deviation for each site. All sites plot within the PSD range, with sites 7 (1949, sea) and 9 (1971, crater) closest to SD and site 14 (3.2 ± 0.01 ka) closest to MD. The sites closest to MD (11, 12, 8, 5 and 14) seem to show more scatter than the sites closer to SD, especially in the H_{cr} / H_c ratio. The large variation within some sites may be due to inhomogeneity as the MicroMag only uses tiny samples, some times no larger than a single crystal.

Table 4.4 Variation in the hysteresis parameters

Parameter	Min. value	Max. value
M_r (mA m^2/kg)	10.5 ± 3.2 (site 7)	562.8 ± 137.9 (site 1)
M_s (Am^2/kg)	0.036 ± 0.011 (site 7)	2.8 ± 0.68 (site 1)
H_c (kA/m)	3.9 ± 0.95 (site 5)	18.3 ± 2.5 (site 9)
H_{cr} (kA/m)	8.1 ± 0.87 (site 3)	31.4 ± 1.9 (site 9)

To assess a possible change in domain state caused by heating, hysteresis loops and back-field curves were also generated for grains of specimen that had been used in MSP experiments. This was only done for sites that showed relatively little scatter. For sites 1, 4, 7, 8, 9 and 15 the deviation between the calculated PI and the palaeofield from the IGRF was known (see **Section 5.2.1**), enabling comparison between a change in domain state and the results from the MSP experiments. Site 14 shows a fairly large scatter, but was interesting to measure because according to Fabian and Leonhardt (2010) MD grains should yield smaller overestimates than PSD grains, which may indicate no or a small change in domain state due to heating.

Results are plotted in **fig. 4.14**. With the exception of site 1 (1949), there seems to be a trend toward more SD behaviour after heating. In particular site 7 (1949, large overestimate in MSP) and 9 (1971, MSP close to IGRF) show a significant change. For the two sites closest to MD — sites 8 (1971) and 14 (3.2 ± 0.01 ka) — it is mainly the H_{cr} / H_c

ratio that seems to change, although especially for site 14 the change is not significant because of the large standard deviation of the results.

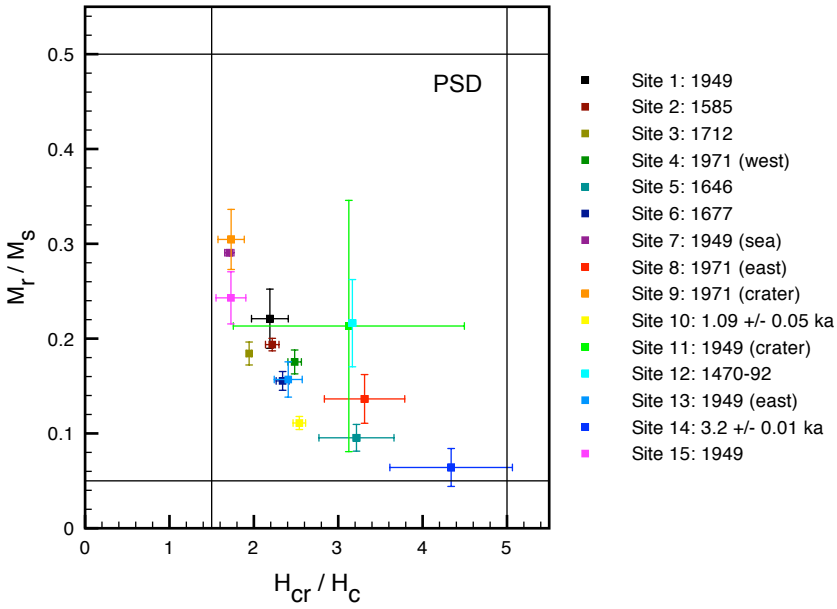

Fig. 4.13 Day plot, before heating.

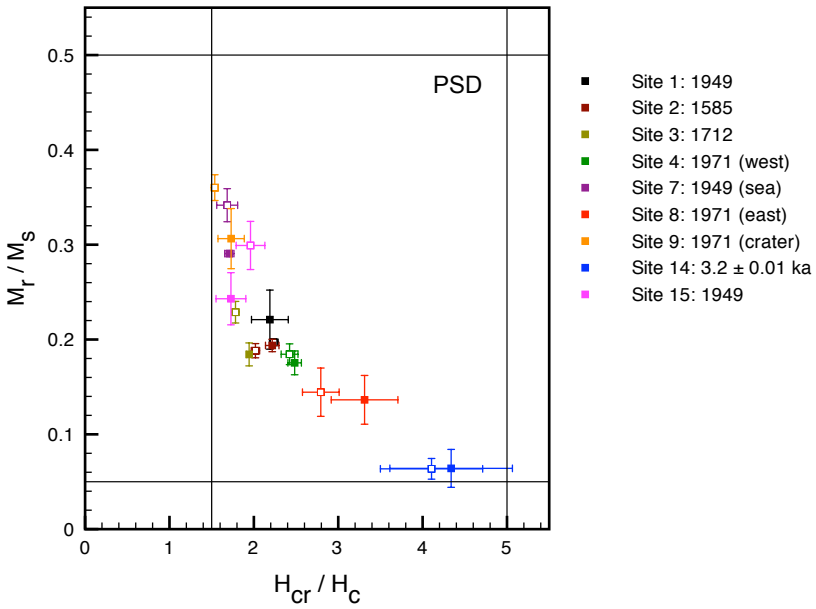

Fig. 4.14 Day plot showing nine sites before (closed symbols) and after heating (open symbols).

4.2.4 Summary

AF and thermal demagnetisation revealed no or only small overprints, which were removed at 5 mT or 100°C. This is important to know before carrying out a PI experiment, because no (or small) directional overprints imply that the intensity stored in the specimen

has not significantly been overprinted by a more recent field, either. Site 7 showed strong alteration, getting more rather than less magnetic during several temperature steps. This alteration was also clearly visible in magnetisation-versus-temperature and susceptibility-versus-temperature diagrams.

Results from the Curie balance and Kappabridge yielded important information on alteration temperatures. Specimens should not alter chemically during PI experiments, so the alteration temperature provides a maximum bound on temperatures used in MSP and Thellier-Thellier-type measurements. Curie diagrams further showed two main groups: one group that has low Curie temperatures (80-120°C) and one that has a broad spectrum and high Curie temperatures (540°C).

Hysteresis loops and back-field curves measured on the MicroMag revealed that all sites are within the PSD range, which is particularly interesting for the MSP-DSC experiment, because PSD particles are predicted to cause the largest overestimate (see **Sections 5.1.3.2** and **5.2.3.2**). Measuring specimens that had been heated to assess whether the domain state changes during an MSP experiment showed a trend toward more SD behaviour.

Based on the results from the preliminary rock magnetic analyses, the following temperatures were chosen for the MSP experiments:

Table 4.5 Curie and alteration temperatures and the temperatures chosen for the MSP experiments.

Site	T_c (°C)	T_{alt} (°C)	T_{MSP} (°C)
1 (1949)	540	350	200
2 (1585)	540	300	200
3 (1712)	210	300	100
4 (1971)	540	300	200
5 (1677)	120	250	100
6 (1646)	540	300	200
7 (1949)	90	200	100
8 (1971)	135	300	100
9 (1971)	540	300	200
10 (1.09 ± 0.05 ka)	475	350	200
11 (1949)	80	300	100
12 (1430)	280	300	200
13 (1949)	100	250	200
14 (3.2 ± 0.01 ka)	370	> 500	200
15 (1949)	90	250	100

5 PALAEOINTENSITIES

5.1 Methods

For low fields such as the Earth's, common mechanisms by which rocks become magnetised (i.e. thermal, in the case of lavas) are approximately linearly related to the ambient field:

$$M_{NRM} = v_{anc} B_{anc} \tag{5.1}$$

where M_{NRM} is the natural remanent magnetisation, B_{anc} the strength of the ancient field and v_{anc} a constant of proportionality. For a laboratory field, a similar equation can be written:

$$M_{lab} = v_{lab} B_{lab} \tag{5.2}$$

If the two constants of proportionality are the same, determining the palaeointensity is straightforward:

$$B_{anc} = \frac{M_{NRM}}{M_{lab}} B_{lab} \tag{5.3}$$

However, in practice it is much more difficult to determine PIs. For example, the proportionality 'constant' v may not be constant at all, or the specimen may have suffered from alteration, due to weathering or during the experiment. Other things that may influence the measurement are anisotropy of the specimen, viscous overprints or its grain size — for PSD and MD grains blocking and unblocking temperatures may not be the same.

5.1.1 Thellier-Thellier method

Theory

In the classic Thellier-Thellier method (Thellier and Thellier, 1959), a specimen's natural remanent magnetisation (NRM) is progressively replaced by a laboratory partial thermoremanent magnetisation (pTRM)[1]. This method relies on two assumptions: firstly that pTRMs acquired by cooling between any two temperature steps are independent of those acquired between any other two temperature steps) and secondly that the total TRM is the sum of all the independent pTRMs).

There are various ways to replace a specimen's NRM with a pTRM. The original method uses two infield heatings ('in-field/in-field' or II) for each temperature step, which are antiparallel to each other. This method implicitly assumes that a magnetisation acquired by cooling from a given temperature is entirely replaced by reheating to the same temperature (i.e. its blocking temperature T_b is equal to its unblocking temperature T_{ub}). Other protocols are the Coe protocol (Coe, 1967), in which a heating step in zero field is followed by an in-field step (ZI) and the Aitken protocol (Aitken *et al*., 1988), which is the other way around (IZ). So-called 'pTRM checks', in which a lower-temperature in-field

[1] I used an 'in-field pTRM', in which the specimen is heated and cooled in-field.

step is repeated, can be incorporated into these three protocols to assess chemical alteration between temperature steps. Methods such as the IZZI method (e.g. Tauxe and Staudigel, 2004) attempt to detect and correct for MD behaviour and the effect of pTRM tails; in case of IZZI by alternating between IZ and ZI steps and adding in both pTRM checks (by repeating in-field steps) and pTRM tail checks (by repeating zero-field steps) (Yu & Tauxe, 2005).

If no chemical alteration has occurred, the pTRM gained between the pTRM check and the preceding zero-field step should be equal to the pTRM gained during the original temperature step. The results are plotted in Arai plots, which plot the NRM remaining after each temperature step against the pTRM gained during that same step. pTRM checks are plotted against the NRM remaining of the original temperature step, i.e. if the pTRM check is at 100°C, it is plotted against the NRM remaining obtained after the zero-field step at 100°C. This allows to directly compare the pTRM gained during the check step with pTRM gained during the original temperature step.

Because the Aitken protocol seemed to work best during preliminary microwave experiments (see **Section 5.2.1**) and it is more straightforward to carry out than the quite complicated IZZI protocol, I used the Aitken parallel protocol. The different steps (in-field, zero-field and pTRM checks) are illustrated in **fig. 5.1**.

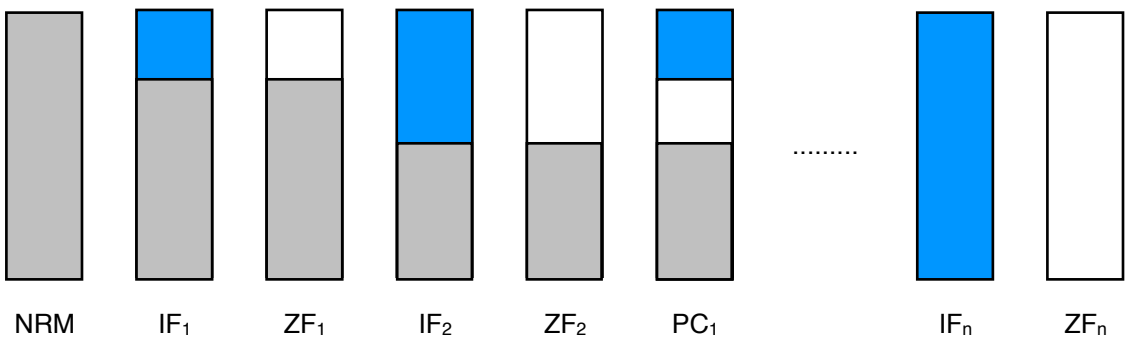

Fig. 5.1 Schematic illustration of the Aitken PI protocol. IF_i represent the in-field steps, ZF_i the zero-field steps and PC_1 represents a pTRM check. The grey shaded area represents the NRM remaining, the white area the part of the specimen that has been unblocked at that temperature step and the blue shaded area the pTRM gained. These figures are for SD particles, for which blocking and unblocking temperatures are equal.

The pTRM gained and the NRM remaining can then be calculated as follows:

$$\text{pTRM gained} = \frac{IF_i - ZF_i}{NRM} \tag{5.4}$$

$$\text{NRM remaining} = \frac{ZF_i}{NRM} \tag{5.5}$$

where IF_i represents the i^{th} in-field step and ZF_i the i^{th} zero-field step. If the field is applied parallel to the NRM, these can be subtracted as scalars; otherwise one has to apply vector subtraction. pTRM checks are calculated by subtracting the preceding zero-field step from the in-field check step and normalising by the NRM:

$$\text{pTRM check} = \frac{\text{IF}_{check} - \text{ZF}_{previous}}{\text{NRM}} \qquad (5.6)$$

Finally, the PI is determined by calculating a linear regression through the data points and multiplying the slope of that line by the laboratory field. If H_{lab} is equal to the palaeofield, the slope should be 1, i.e. a full pTRM acquired in the laboratory field should equal the NRM if $H_{lab} = H_{anc}$.

Thellier-Thellier-type methods are widely used, but they suffer from several drawbacks. Alteration may have influenced the specimen's ability to acquire a pTRM, which means v_{lab} and v_{anc} are no longer equal. And for larger grain sizes (PSD and MD) the unblocking temperature T_{ub} and the blocking temperature T_b may not be equal, which can lead to so-called pTRM tails. There are two types of pTRM tails. The first are high-temperature tails, in which part of the specimen that should not have unblocked yet at temperature T does gain a (less effective) pTRM. This pTRM tail is not removed by reheating to the same temperature in zero field (**fig. 5.2a**.). The second are low-temperature tails, in which part of the specimen that has been unblocked at T does not gain a pTRM (**fig. 5.2b**.). This is illustrated in more detail by **fig. 5.7** in **Section 5.1.3.2**. These effects may show as sagging in the Arai plots (e.g. site 13 in **Appendix III**).

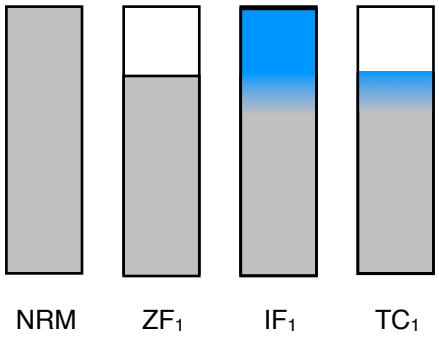

Fig. 5.2a Illustration of a high-temperature tail and a pTRM tail check (TC) in an experiment using the Coe protocol. Part of the pTRM gained is not removed by reheating to the same temperature in zero field.

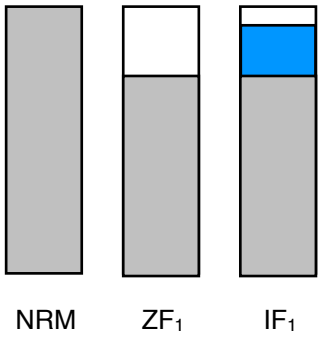

Fig. 5.2b Illustration of a low-temperature tail in an experiment using the Coe protocol. Because $T_b > T_{ub}$, only part of the unblocked area gains a pTRM.

Experiment

I used samples of diameter 1 inch and height 1 to 1.5 cm, which is about half of the standard specimen size, to prevent the SQUID magnetometer going out of range. Specimens of sites that were still likely to go out of range based on thermal demagnetisation experiments (sites 2, 3, 6, 8, 9, 10, 11, 12 and 13) were made even smaller by drilling 16-18 mm diameter specimens out of the original specimens.

In the microwave experiments (see **Section 5.1.2**) the Aitken protocol at a laboratory field lower than the expected palaeofield seemed to yield the best results, so to facilitate easy comparison between the two methods, I used the Aitken protocol (IZ) and a laboratory field of 30 μT. In principle the specimens do not have to be aligned in a certain direction to the field, but work by Yu, Tauxe and Genevey (2004) indicates that the Aitken protocol yields the best results when the specimens are aligned parallel to the field. Aligning the specimens this way also allows to use scalar instead of vector subtraction to

calculate the pTRM gained after each temperature step. **Fig. 5.3** shows the method used to align the specimens.

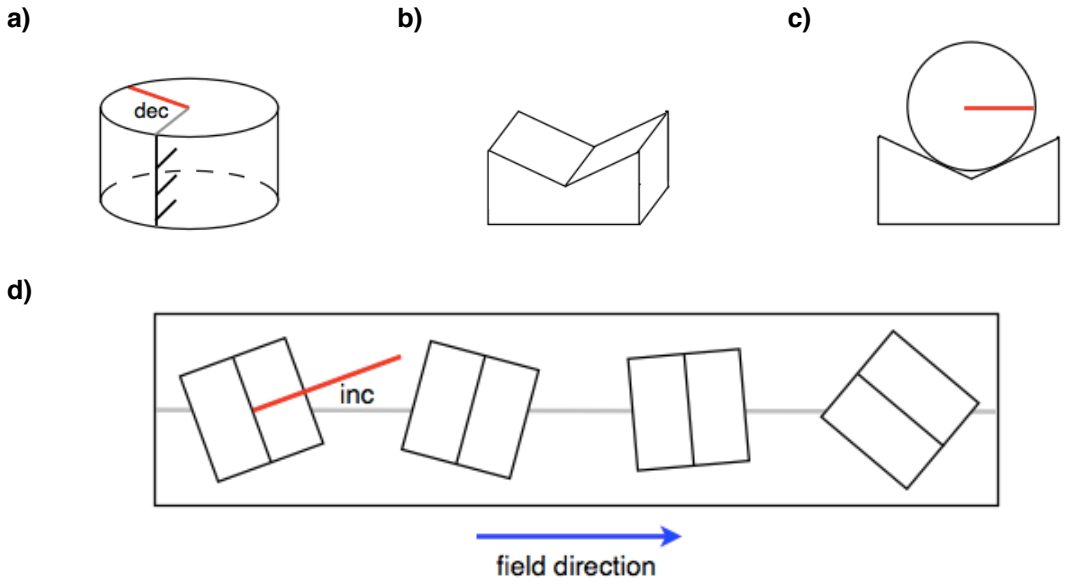

Fig. 5.3 This figure shows how a specimen is aligned parallel to the field in the oven. **a)** The declination is shown as the angle between the grey and red lines. **c)** The specimen is rotated on a holder as shown in **b)** so that the declination is horizontal. **d)** The blocks (maximum ten) are rotated so that angle between the grey and red lines is equal to the measured inclination.

The temperature steps (**table 5.1**) depended on the characteristics of the site under study; larger steps for sites with high Curie temperatures and smaller steps for sites with (very) low Curie temperatures. pTRM checks were performed after each second temperature step. The results are plotted in Arai plots, with the NRM remaining after each temperature step on the vertical axis and the pTRM gained after each step on the horizontal axis (e.g. **fig. 5.4**). PIs were calculated by multiplying the slope of the linear regression through the data points by H_{lab}.

Table 5.1 Temperature steps used in the Thellier-Thellier experiment, in °C. IF: in-field; ZF: zero field; CHECK: pTRM check.

Step	**A** 1, 4-T, 9, 10	**B** 2, 4-M, 4-B, 14	**C** 7, 11, 15	**D** 5, 8, 13	**E** 3, 6, 12
NRM	Room temp.	Room temp.	Room temp.	Room temp.	Room temp.
IF 1	60	60	60	60	60
ZF 1	60	60	60	60	60
IF 2	100	100	80	80	100
ZF 2	100	100	80	80	100
IF 3	~~145~~	145	100	100	145
ZF 3	~~145~~	145	100	100	145
CHECK	60	60	60	60	60

Step	A 1, 4-T, 9, 10	B 2, 4-M, 4-B, 14	C 7, 11, 15	D 5, 8, 13	E 3, 6, 12
IF 4	190	190	130	130	190
ZF 4	190	190	130	130	190
IF 5	235	235	160	160	235
ZF 5	235	235	160	160	235
CHECK	145	145	100	100	145
IF 6	290*	-	200	200	-
ZF 6	290*	-	200	200	-
IF 7	-	-	240	240	-
ZF 7	-	-	240	240	-
CHECK	190	-	160	160	-

* Only sites 1 and 10, because site 4 has a lower alteration temperature. (See **4.2.2**.)

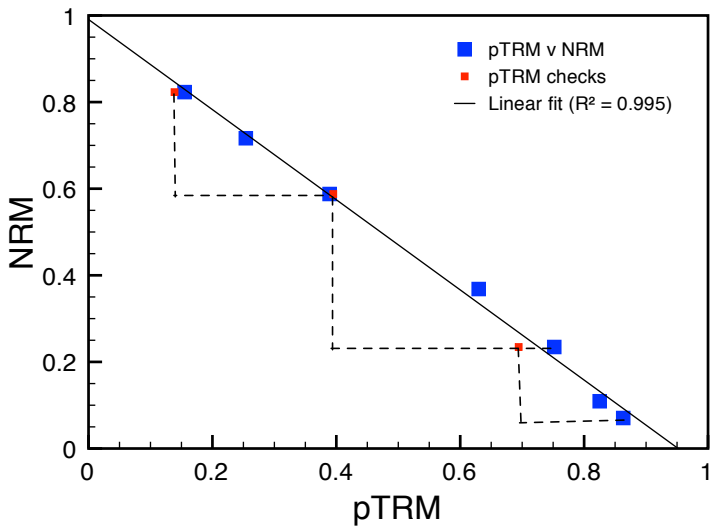

Fig. 5.4 Example of an Arai plot. The NRM remaining is plotted against the pTRM gained after each step (large blue squares). The small red squares indicated pTRM checks, performed after every second temperature step. The first two checks more or less coincide with the original measurements, which suggests that no alteration has occurred between the original step and the pTRM check. The PI is calculated by multiplying the slope of the linear fit by the lab field, in this case 30 μT.

5.1.2 Microwave method

Theory

The microwave method, like Thellier-Thellier, is a step-wise method, but — as its name suggests — it uses high-frequency microwaves to directly excite the magnetic spin system within the magnetic grains in order to re- or demagnetise a specimen. Because only the

magnetic phases are heated, the bulk sample experiences far less heating, thus reducing the degree of alteration (Tauxe, *Essentials*; Hill and Shaw, 2007).

However, it is much less straightforward to reproduce a microwave intensity than it is a temperature in a conventional oven. One way of working around this is by using the Kono perpendicular method (e.g. Hill and Shaw, 2007) which only uses one measurement per (temperature) step. However, having the signal generator under remote control so that the system is automatically kept in resonance has improved the reproducibility of the absorbed power. The difference between the applied and reflected power (the 'power integral') gives an is expected to be similar (generally within 5%) for the same applied power and power absorption by the sample. These developments made it possible to carry out double-heating experiments and to perform checks (Hill and Shaw, 2007).

The microwave system in Liverpool I used operates at 14 GHz; its maximum power is 40 W. The very small specimens (2 mm diameter) are inserted into the microwave system and SQUID magnetometer vertically and kept in place using a vacuum. The system has two Helmholtz field coils, which can produce a field in the Z and Y directions. A field can be applied in any direction within the Y-Z plane with any magnitude up to 100 μT, which means the specimen itself does not have to be aligned (Hill and Shaw, 2007).

Fig. 5.5 The automated microwave system at the University of Liverpool, combined with a Tristan Technologies liquid helium cooled SQUID magnetometer with a cryocooler. (Source: http://www.liv.ac.uk/earth/geomagnetism/facilities.htm.)

Experiment

Specimens of diameter 2 mm and length 1-6 mm were drilled out of the original 1-inch-diameter specimens. The best frequency to carry out the experiment was determined by sweeping frequencies and selecting the frequency at which absorption was highest. One

specimen with a high T_c and one with a low T_c were demagnetised to get used to operating the microwave system and to assess the step size needed for the actual PI experiment. After this preliminary step, three different protocols were tested on sites 4 (high T_c) and 15 (low T_c): the IZZI antiparallel protocol, the Aitken parallel protocol and the perpendicular protocol.[2] The Aitken parallel protocol generally yielded the best results, especially at fields below the expected palaeofield. Consequently, measurements on the other sites were carried out using the Aitken protocol at H_{lab} = 25 μT.

Step size varied widely between sites, depending not only on its Curie temperature, but also on the amount of absorbed microwave radiation. Site 6, for example, absorbed so little radiation that it was impossible to perform the PI experiment. Site 11, on the other hand, lost magnetisation very fast, requiring power steps of just 1 W. During the experiment, power was increased until it reached about 35 W. If more microwave energy was needed, the application time was increased from the standard 5 s to 10 s or more.

Like the results from the Thellier-Thellier PI experiments, results were plotted in Arai plots (e.g. **fig. 5.4**), with the NRM remaining on the vertical axis and the pTRM gained on the horizontal axis. In the experiments using the Aitken protocol, these were calculated in the same way as for Thellier-Thellier. (See **eqs 5.4-6**.) In the IZZI protocol, the field is aligned anti-parallel to the sample and every other step is the other way around from Aitken (i.e. zero-field/in-field instead of in-field/zero-field), slightly complicating the calculations. For results obtained using the perpendicular protocol, an Excel template by Mimi Hill (University of Liverpool) was used to calculate the NRM remaining and pTRM gained and to calculate the angle between these two, which should be (close to) 90°.

5.1.3 Multispecimen method

5.1.3.1 MSP-DB

Theory

The multispecimen parallel differential pTRM method (MSP-DB) is based on the linearity of pTRM with inducing field. This property should be independent of domain state, which means the method can be applied to all magnetic grains, as long as no alteration occurs. Each sample undergoes just one treatment, to ensure all samples have the same magnetic history. An ancient TRM is overprinted by an artificial pTRM pointing in the same direction at a single low measurement temperature, which must be higher than the highest demagnetising temperature of the viscous component. The basic principle is illustrated in **fig. 5.6**: if the intensity of the lab field is equal to the intensity of the ancient field, the resulting remanence will be equal to the specimen's NRM.

[2] A mathematical model by Yu, Tauxe and Genevey (2004) indicates that the Aitken protocol yields the best results when H_{lab} // H_{anc}, whereas the Coe (and IZZI) protocol yields the best results when H_{lab} is applied antiparallel to H_{anc}.

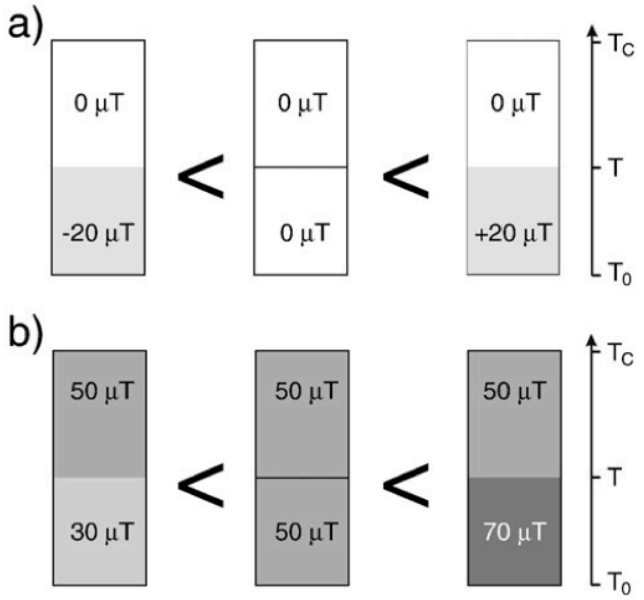

Fig. 5.6 The basic principle underlying the multispecimen method, where T_c is the Curie temperature, T_0 room temperature and T the temperature used when overprinting part of the original NRM. The part between T_0 and T thus represents the part of magnetisation of the specimen that has been unblocked at T and the part between T and T_c the part that is still blocked. **a)** A negative overprint over a zero-field TRM will lead to a negative remanence, a zero-field overprint to zero remanence and a positive overprint to a positive remanence. Shifting this by 50 μT using Biggin and Poidras' symmetry relation (2006) leads to **b)**. Figure from Fabian and Leonhardt (2010).

This is visualised by plotting the DB ratio Q_{DB} against the lab field H_{lab} (e.g. **fig. 5.7**).

$$Q_{DB} = \frac{m_1 - m_0}{m_0} \tag{5.7}$$

where m_0 represents the specimen's NRM and m_1 represents its remanence after partially overprinting it in a parallel field. According to the premise of the MSP-DB method, this ratio should be zero if the laboratory field is equal to the ancient field. Because for low fields such as the Earth's, a rocks magnetisation is approximately linearly related to the ambient field, Q_{DB} plotted against H_{lab} should in principle yield a straight line.

The multispecimen method has several important advantages compared to Thellier-Thellier-type experiments. Firstly, it is not limited to SD particles, but allows all magnetic domain states to be processed. Using multiple specimens ensures that all specimens experienced the same magnetic history. Alteration effects are reduced by limiting the number of temperature steps (only one per specimen) and selecting the pTRM acquisition temperature below the alteration temperature. High-temperature tails that effect MD minerals are minimised by aligning the laboratory pTRM parallel to the specimens' NRM. Finally, because the multispecimen protocol requires less steps than any other PI method, it drastically decreases the total time needed to process a rock unit (Dekkers and Böhnel, 2006).

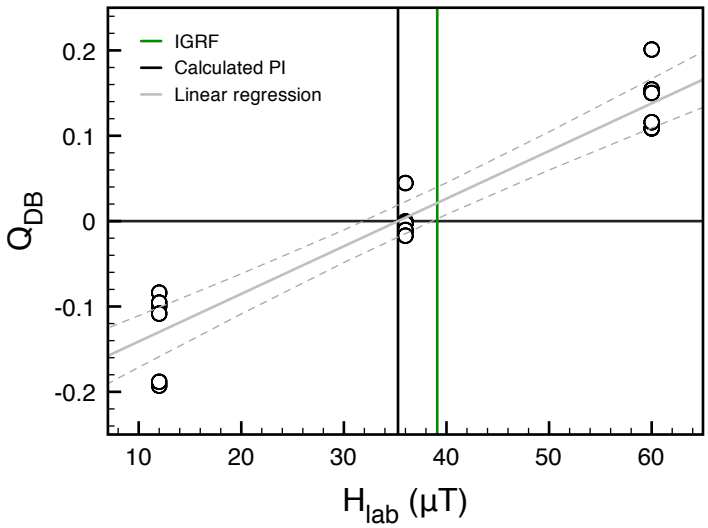

Fig. 5.7 Example of an MSP-DB plot. The linear regression through the data points is shown in grey and its intersection with the *x*-axis (i.e. the calculated PI) is shown as a black line. If applicable, the IGRF value for the intensity is plotted in green.

Experiment

Each specimen was measured twice using a SQUID magnetometer. Once before heating (m_0, the specimen's NRM) and once after it has been overprinted in a parallel field (m_1). The temperatures used in the experiment were based on Curie diagrams of each site. Sites 3, 5, 7, 8, 11 and 15 were overprinted at a temperature of 100°C; sites 1, 2, 4, 6, 9, 10, 12, 13 and 14 were overprinted at a temperature of 200°C. Samples were aligned parallel to the field in the oven using the method illustrated in **fig. 5.3**.

I tested the protocol on site 15, using three field steps: 0 μT, 30 μT and 60 μT and two specimens per field step. The zero-field step yielded odd results, so in later experiments I used steps of 12 μT, 36 μT and 60 μT. For most sites, nine specimens were measured; three for every field step. For site 4, six specimens per drilling row were measured (2 per row per field step). For site 11, five additional specimens were measured because the MSP-DB plot did not show a straight line.

Results were plotted with the DB ratio Q_{DB} on the vertical axis and the lab field on the horizontal axis. I wrote a Scilab code to calculate Q_{DB}, a linear regression through the data points and the PI. (See **Appendix VI**.) The confidence interval of the linear regression was calculated using the following equation in Excel:

$$t \cdot SYX \cdot \sqrt{\frac{1}{n} + \frac{\left(H_{lab} \cdot XAVG\right)^2}{SSX}} \tag{5.8}$$

where t is the inverse of the Student T distribution, SYX the standard error in the estimate (STEYX(y,x) in Excel), n the number of specimens, XAVG the average x value (i.e. the average value of H_{lab}) and SSX the sum of the squared deviations of the data points with respect to the average of the statistical sample (DEVSQ(x) in Excel). These values are added to (subtracted from) the linear regression to produce the upper (lower) margin of the error envelope.

5.1.3.2 MSP-DSC

Theory

Because MSP-DB seemed to systematically overestimate palaeointensities, especially for intermediate-sized grains, Fabian and Leonhardt (2010) proposed the MSP-DSC protocol, where DSC is short for 'domain-state corrected'. The protocol consists of three additional steps per specimen compared to MSP-DB, which are used to correct the slope of the resulting plot, estimate the domain state and detect chemical alteration. It is supposed to lower overestimates and reduce scatter.

These steps are based on an extended version of the TRM model shown in **fig. 5.6**, which includes a pTRM tail and an in-field heating effect (**fig. 5.8a-c**). In this figure, the magnetic remanences in the specimen are basically grouped by their blocking (on the horizontal axis) and unblocking (on the vertical axis) temperatures. Blocking and unblocking temperatures need not be the same for PSD and MD grains, which means only part of the unblocked grains are remagnetised by the lab field (represented by the dark grey and white parts, respectively). The model also accounts for the observed MD tail of pTRM (**fig. 5.8a**) and an in-field heating effect (**fig. 5.8b**). This effect prevents unblocked remanences from demagnetising completely. But because they also do not acquire a full TRM, they are considered to be less effective than the initial TRM.

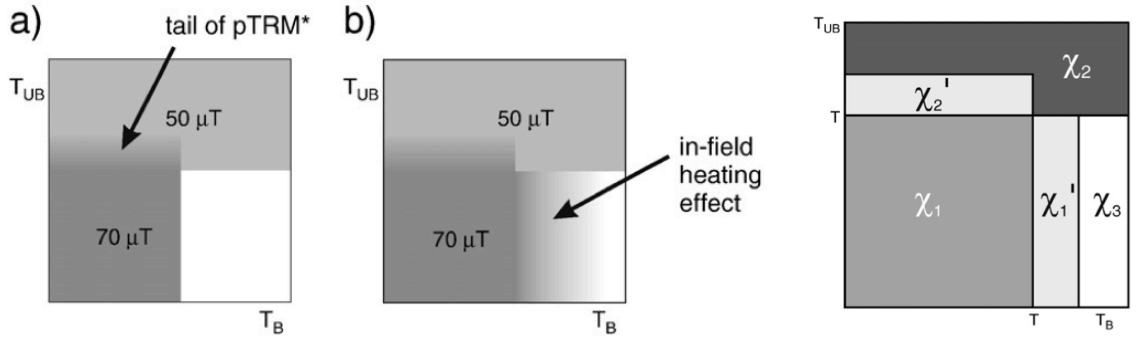

Fig. 5.8 The phenomenological TRM model used in the MSP-DSC method, which accounts for inequality of blocking and unblocking temperatures, the experimentally observed pTRM tail (**a**) and an in-field heating effect (**b**). A simplified representation of the relevant areas to describe the remanent magnetisations for the MSP-DSC protocol is shown on the right. Figures from Fabian and Leonhardt (2010)

Using this phenomenological model, the different steps of the protocol can be visualised as follows (figures from Fabian and Leonhardt, 2010):

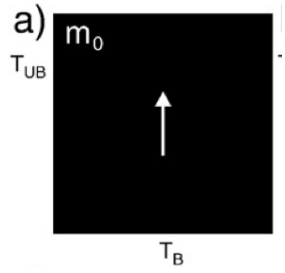

Step 0: NRM. In terms of the phenomenological model:

$$m_0 = \chi_2 H + \chi_1 H + \chi_2' H + \chi_1' H + \chi_3 H$$

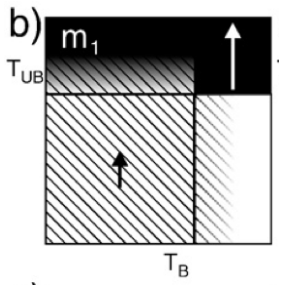

Step 1: Heat and cool in parallel field. (Same as MSP-DB.)

$m_1 = \chi_2 H + \chi_1 H_{lab} + \chi_2' H_{lab} + \chi_1' H_{lab}$

Subtracting m_0 from m_1 and dividing by two yields the figure on the right, as suggested by MSP-DB.

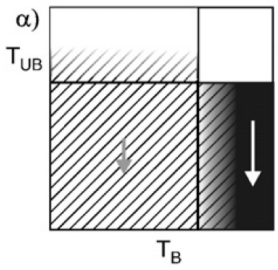

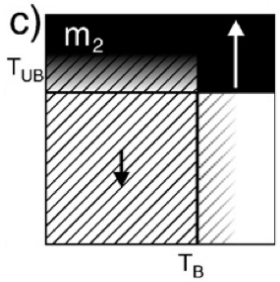

Step 2: Heat and cool in antiparallel field.

$m_2 = \chi_2 H - \chi_1 H_{lab} - \chi_2' H_{lab} - \chi_1' H_{lab}$

This step is used to determine a slope correction, as illustrated by β), which shows $(m_1 + m_2)/2$.

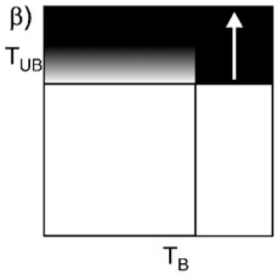

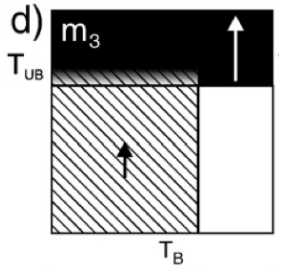

Step 3: Heat in zero field, cool in parallel field.

$m_3 = \chi_2 H + \chi_1 H_{lab} + \frac{1}{2}\chi_2' H_{lab}$

This step is used to estimate the domain state effect, by subtracting m_3 from m_1 and dividing by two.

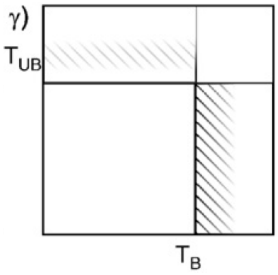

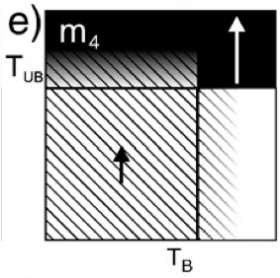

Step 4: Repeat step 1. m_4 - m_1 can deviate from zero because of measurement uncertainty or chemical alteration between steps 1 and 4.

The areas shown in the simplified version of the phenomenological model (**fig. 5.7c**) can be used to calculate a variety of parameters, for example the two single-specimen estimates H_{max} and H_{est}. H_{max} is an upper estimate of the palaeofield:

$$H_{\max} = \left(1 + \frac{\chi_3}{\chi_1 + \chi_1' + \chi_2'}\right) = \frac{2m_0 - m_1 - m_2}{m_1 - m_2} H_{lab} \qquad (5.9)$$

Because $\chi_3 > 0$ except for SD particles, the phenomenological model predicts that H_{max} will always overestimate the field. A better estimate can only be obtained if χ_3 is better known, which appears to be intrinsically impossible to exactly measure. Fabian and Leonhardt approximate χ_3 by introducing the parameter $\alpha > 0$:

$$\chi_3 = \alpha \frac{m_1 - m_3}{H_{lab}} \qquad (5.10)$$

Experiments indicate that the value of α typically lies between 0.2 and 0.8. I always used the 'standard' value of 0.5 in my calculations.

Using this estimate of χ_3, Fabian and Leonhardt obtain a domain-state corrected single-specimen estimate:

$$H_{est} = \frac{2m_0 - m_1 - m_2}{(1+2\alpha)m_1 - 2\alpha m_3 - m_2} H_{lab} \tag{5.11}$$

Using the phenomenological model, the DB ratio from the original multispecimen protocol can be extended. m_2 can be used to improve the normalisation of the DB ratio by calculating the *f*-corrected MSP-FC ratio:

$$Q_{FC} = 2\frac{m_1 - m_0}{2m_0 - m_1 - m_2} \tag{5.12}$$

Finally, the domain-state-corrected MSP-DSC ratio is given by:

$$Q_{DSC} = 2\frac{(1+\alpha)m_1 - m_0 - \alpha m_3}{2m_0 - m_1 - m_2} \tag{5.13}$$

As in MSP-DB, it is assumed that $Q_{DSC} = 0$ if $H_{lab} = H_{anc}$. The PI is thus found by drawing a linear regression through the data points and determining where it intersects the *x*-axis. The intensity error ΔH can be calculated using:

$$\left(\frac{\Delta H}{H}\right)^2 = \left[\sum_{i=1}^{N}\left(\frac{H_i/H}{\Delta Q_i}\right)^2\right]^{-1} \tag{5.14}$$

where H is the calculated palaeofield, N the number of specimens, H_i the laboratory field used for the i^{th} specimen and ΔQ_i the total error of the i^{th} specimen. Results are plotted in the same way as for MSP-DB, only with Q_{DSC} instead of Q_{DB} on the vertical axis and with the addition of the intensity error ΔH (dashed black lines). An example is shown in **fig. 5.9**.

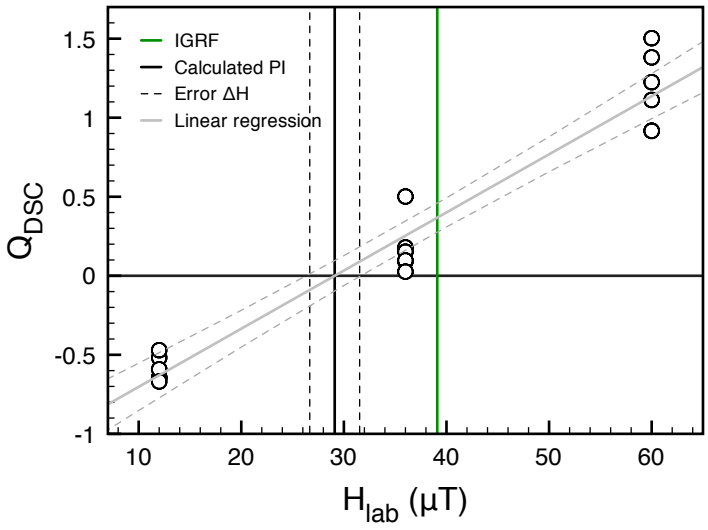

Fig. 5.9 Example of an MSP-DSC plot showing the measured data points, the linear regression through the data points (grey line), the calculated PI (the intersection with the *x*-axis; black line), the intensity error ΔH and (if applicable) the IGRF value of the intensity.

Experiment

The first two steps of the MSP-DSC protocol are the same as in MSP-DB. Therefore, I could use the same specimens and oven temperatures as in the DB method. All samples were measured an additional three times (m_2 to m_4) using a SQUID magnetometer. In steps 1, 3 and 4 the specimens were aligned parallel to the field; in step 2 the specimens were aligned anti-parallel to the field. In steps 1, 2 and 4 the specimen was heated and cooled in-field, whereas in step 3 the specimen was heated in zero field and cooled in-field. (See **table 5.2**.)

I wrote a Scilab code to convert the magnetisation vectors to scalar intensities and calculate a range of parameters described in Fabian and Leonhardt (2010). The Scilab program is described in more detail in **Appendix VI**.

Table 5.2 Summary of the measurements used in the MSP-DSC protocol. Step 1 is identical to MSP-DB.

Step	Heating	Cooling	Field direction
1	In-field	In-field	Parallel
2	In-field	In-field	**Anti-parallel**
3	**Zero field**	In-field	Parallel
4	In-field	In-field	Parallel

5.1.3.3 Full TRM

Site 11 provided a very interesting test case, because its Curie temperature (80°C) is much lower than its alteration temperature (300-350°C), which means it has lost most of its magnetisation at a temperature well below the alteration temperature. This was corroborated by its thermal NRM decay curve. (See **Section 4.2.1** and **Appendix I**.) This means it can be given a full TRM (i.e. the entire NRM is replaced by a laboratory TRM in a magnetic field of known intensity) without altering the specimen, at least in theory. PI experiments should then yield the intensity of the field used to overprint the specimens.

Nine specimens (18 mm diameter) were first AF demagnetised using a field of 300 mT to ensure most (about 99%) of its NRM was gone. This was tested by measuring the specimens' magnetisation in the SQUID magnetometer before and after AF demagnetising them. The specimens were overprinted using a field of 40 μT at 250°C, after which the MSP-DB protocol was applied at a temperature of 100°C.

5.2 Results

5.2.1 Thellier-Thellier method

All Thellier-Thellier results were obtained using the Aitken protocol and a laboratory field of 30 μT. Two plots are shown in **fig. 5.10a-b**: one technically acceptable plot and one plot that shows sagging. All Arai plots can be found in **Appendix III**; results are summarised in **table 5.3**. It can be seen from the Arai plots that many sites lose less than 30% — and often even less than 10 to 20% — of their NRM during the experiments, which were all carried out at temperatures below the sites' alteration temperatures.

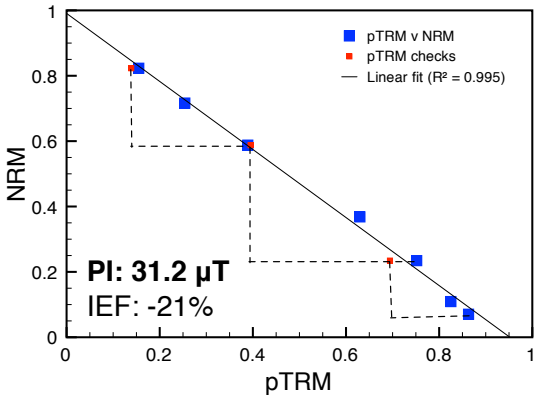

Fig. 5.10a This Arai plot for site 11 (1949, crater) is technically very good: the specimen loses a lot of its NRM, the plot shows a straight line and the pTRM checks are good. The calculated PI, however, is 21% below the IGRF value for 1949.

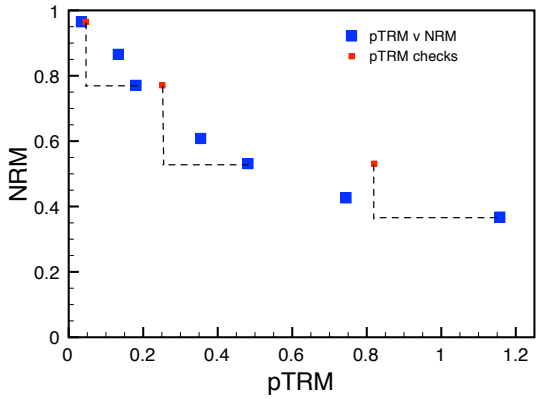

Fig. 5.10b This Arai plot for site 13 (1949, east) shows strong sagging and failed pTRM checks.

Ten out of fifteen measured sites yielded acceptable results based on the performed pTRM checks and the linearity of their plots. Site 1 (1949) and in particular site 13 (1949, east) showed sagging in their Arai plots, rendering it impossible to extract PIs. Eleven measurements were considered unreliable because of failed pTRM checks. (Marked in grey in **table 5.3**.) Despite drilling smaller (16-18 mm) samples out of the original 1-inch specimens, four measurements failed because the DC SQUID magnetometer went out of range.

Of the sites that could be compared to the IGRF, sites 4 (1971, west), 9 (1971, crater) and 15 (1949) showed straight lines and reasonably good pTRM checks and yielded PIs within 10% of their IGRF values, but all three lost less than 30% of their NRMs. Site 7 (1949, sea) also produced reasonably good Arai plots, but yielded underestimates of 7 to 22%. Site 1 (1949) and in particular site 13 (1949, east) showed sagging; no PIs could be extracted. Of the site 8 (1971, east) measurements, two failed due to bad pTRM checks and the third yielded an underestimate of 18%. Finally, site 11 (1949, crater) is perhaps the most interesting of the 20th-century sites because its Arai plots are technically very nearly perfect: it loses more than 90% of its magnetisation, its data points are on very straight lines ($R^2 > 0.995$) and its pTRM checks are generally very good. However, all three measured specimens yielded underestimates of 21-32% compared to the IGRF, indicating that technically good Arai plots are no guarantee for success.

Table 5.3 Thellier-Thellier results. Grey results indicate failed pTRM checks and thus unreliable results.

Site	IGRF	Sample 1	Sample 2	Sample 3	Average (success rate)	IEF (%)
1	**39.4**	sagging	sagging	sagging	-	-
2		40.4	51.3	47.0	-	-
3		out of range	28.6	34.8	31.7 (2/2)	-
4 - T	**39.1**	36.1	35.7	-	35.9 (2/2)	-8.2
4 - M	**39.1**	36.7	36.7	-	36.7 (1/2)	-6.1
4 - B	**39.1**	40.8	40.0	-	40.8 (1/2)	+4.3
4 - all	**39.1**	-	-	-	37.3 (4/6)	-4.6
5		42.3	45.2	46.6	-	-
6		failed	out of range	55.8	55.8 (1/3)	-
7	**39.4**	32.2	31.2	30.8	31.0 (2/3)	-21.3
8	**39.1**	35.2	32.0	31.2	32.0 (1/3)	-18.2
9	**39.1**	37.0	42.1	46.3	41.8 (3/3)	+6.9
10		37.7	37.0		37.4 (2/2)	-
11	**39.4**	29.0	26.9	31.2	29.0 (3/3)	-26.4
12		36.1	out of range	out of range	36.1 (1/3)	-
13	**39.4**	sagging	sagging	sagging	-	-
14		failed	failed	failed	-	-
15	**39.4**	40.0	40.2	36.6	38.9 (3/3)	-1.3

5.2.2 Microwave method

Three microwave protocols (Aitken parallel, IZZI antiparallel and perpendicular) were tested on one site with a high Curie temperature (site 4, 1971) and one site with a low Curie temperature (site 15, 1949). The perpendicular protocol failed for site 15 and yielded a large underestimate for site 4. Because no pTRM checks can be incorporated into the perpendicular protocol, there is no way of testing the reliability of a measurement. The IZZI protocol failed for both sites, because of sagging (site 4) or failed pTRM checks (both sites). The Aitken parallel protocol yielded the best results for both sites. If steps with failed pTRM checks were not taken into account, the Aitken protocol using H_{lab} = 40 μT applied to site 4 yielded a PI of 42.6 μT, which is within 10% of the IGRF value of 39.1 μT. Using H_{lab} = 30 μT, site 4 yielded a PI of 34.4 μT, 12% below the IGRF value. Applying the Aitken protocol to site 15 using H_{lab} = 25 μT produced a very straight line and good pTRM checks for the first 6 data points and a PI of 42.9 μT, which is within 10% of the IGRF value of 39.4 μT.

My measuring time at the Geomagnetic Laboratory of the University of Liverpool was limited, so for most sites only one specimen was measured. Because of the results for sites 4 and 15, I chose to use the Aitken parallel protocol and a laboratory field of 25 µT. The results were plotted in Arai plots, which can be found in **Appendix IV**. The obtained PIs can be found in **table 5.4**; a few Arai plots are shown in **fig. 5.11a-d**. Site 6 (1646) could not be measured because it did not absorb enough radiation; site 10 (1.09 ± 0.05 ka) could not be measured because the specimens were very vesicular and easily fell apart, making it impossible to drill 2-mm samples out of the original 1-inch-diameter specimens. Site 7 (1949, sea) showed alteration during microwave demagnetisation and was measured using the perpendicular protocol to reduce the number of heating steap and hopefully minimise alteration.

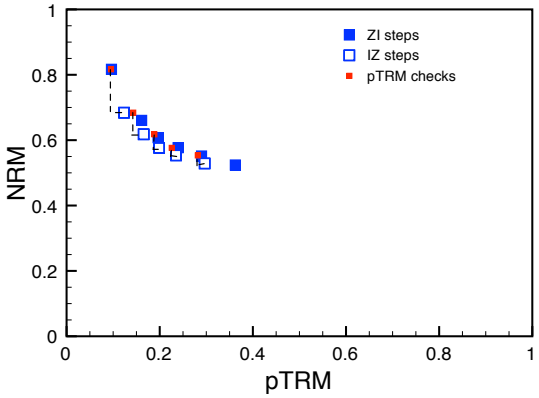

Fig. 5.11a This microwave Arai plot for site 1 (1949) using the IZZI antiparallel protocol and H_{lab} = 30 µT shows strong sagging.

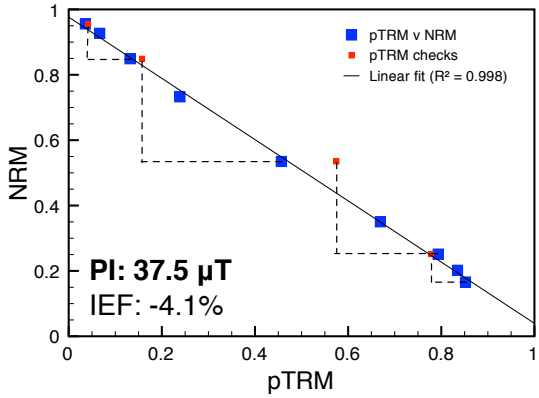

Fig. 5.11b Technically acceptable microwave Arai plot for site 9 (1971, crater) obtained using the Aitken parallel protocol and H_{lab} = 40 µT.

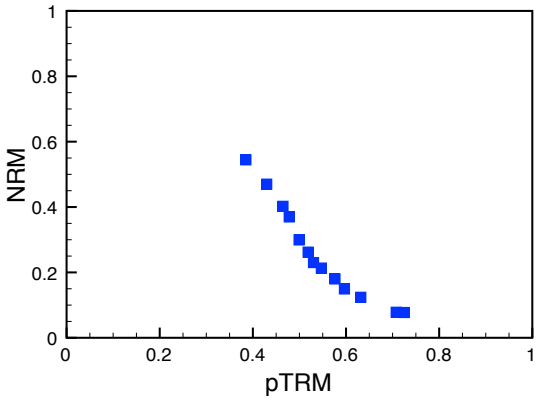

Fig. 5.11c Microwave Arai plot for site 7 (1949, sea) obtained using the perpendicular protocol and H_{lab} = 25 µT. The plot shows sagging.

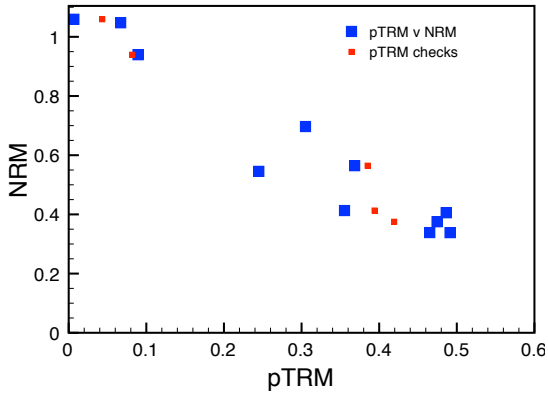

Fig. 5.11d This microwave Arai plot for site 14 (3.2 ± 0.01 ka) obtained using the Aitken parallel protocol and H_{lab} = 25 µT shows failed pTRM checks and very odd data points.

Sites 5 (1677) and 7 (1949, sea) showed sagging and sites 8 (1971, east) and 14 (3.2 ± 0.01 ka) failed their pTRM checks. The other sites, however, yielded reasonably straight lines and good pTRM checks. PIs were close to the IGRF for the 20th-century sites (generally within 10%) or yielded plausible results. Site 9 (1971, crater) in particular yielded very

good results, so when I had time left, I also performed the IZZI anti-parallel protocol at H_{lab} = 25 μT and the Aitken parallel protocol at H_{lab} = 40 μT. Both measurements yielded results close to the IGRF value for 1971 (39.1 μT). Site 9 is very close to SD, which may (partly) explain the good results.

In general, it can be said that if the Arai plots show straight lines and good pTRM checks, the resulting PI is close to the IGRF value. This in contrast to the Thellier-Thellier experiments, in which technically good plots some times yielded large over- or underestimates.

Table 5.4 Microwave results in μT.

Site	**IGRF**	**Aitken**	**IZZI**	**Perpendi-cular**	**Average (success rate)**	**IEF** (%)
1	**39.4**	-	sagging	-	-	-
2		43.5	-	-	43.5 (1/1)	-
3		43.0	-	-	43.0 (1/1)	-
4 - T	**39.1**	34.4	-	-	34.4 (1/1)	-12.0
4 - M	**39.1**	-	-	-	-	-
4 - B	**39.1**	42.6	failed	19.1 (no checks)	30.9 (2/2) 42.6 (1/2)	-21.0 +9.0
4 - all	**39.1**	-	-	-	32.0 (3/3) 38.5 (2/3)	-18.2 -1.5
5		sagging	-	-	-	-
6		-	-	-	-	-
7	**39.4**	-	-	sagging	-	-
8	**39.1**	failed	-	-	-	-
9	**39.1**	37.5 42.5	42.5	-	40.8 (3/3)	+4.3
10		-	-	-	-	-
11	**39.4**	44.1	-	-	44.1	+11.9
12		44.1	-	-	44.1	-
13	**39.4**	43.8	-	-	43.8	+11.2
14		failed	-	-	-	-
15	**39.4**	42.9	failed	sagging	42.9	+8.9

5.2.3 Multispecimen method

5.2.3.1 MSP-DB

Results for the MSP-DB protocol are summarised in **table 5.5**; a few plots are shown in **fig. 5.12a-d**. All plots can be found in **Appendix V**. Outliers, which were not taken into account in the linear regression, are marked in red. Because the Scilab code I wrote calculated MSP-DB and MSP-DSC parameters simultaneously, some times data points that were all right in MSP-DB were discarded because they were outliers in MSP-DSC (e.g. sites 8 and 9).

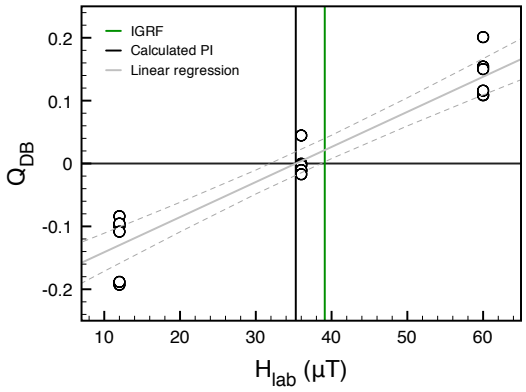

Fig. 5.12a MSP-DB plot for site 4 (1971), which yields a small underestimate.

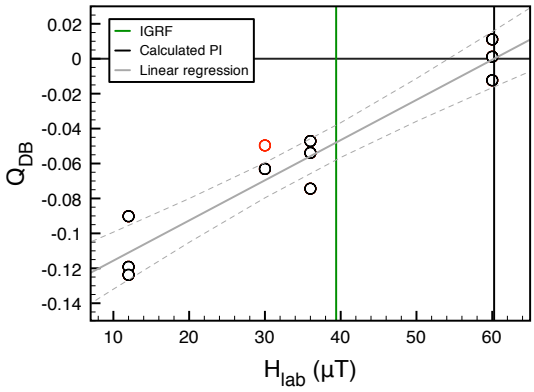

Fig. 5.12b MSP-DB plot for site 15 (1949), which yields a large overestimate. The red data point was discarded because it was an outlier in the DSC plot.

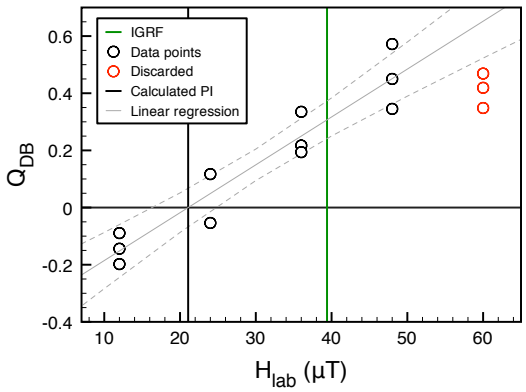

Fig. 5.12c MSP-DB plot for site 11 (1949, crater), which yields a large underestimate. The red symbols indicated discarded data points.

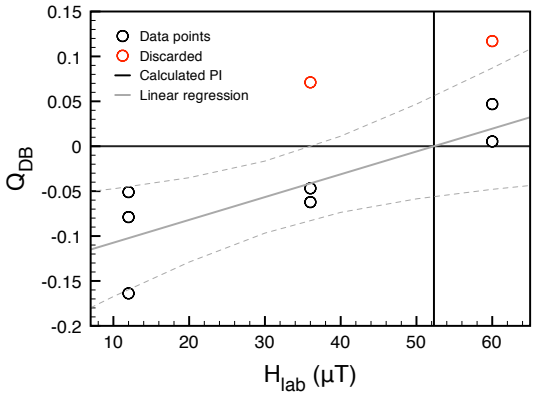

Fig. 5.12d MSP-DB plot for site 2 (1585), which shows a lot of scatter.

In general, most sites yielded acceptable results: the data points were on a more or less straight line and showed relatively little scatter. Data points at 60 μT tended to show the largest scatter (e.g. sites 4 and 13). Sites 2 (1585) and 9 (1971, crater) showed the largest scatter and the lowest values of R^2 (0.683 and 0.752, respectively). Site 7 (1949, sea) and the bottom row of site 4 (1971) showed the least scatter.

Of the sites within the IGRF range, sites 1 (1949) and 4 (1971, west) yielded small (<10%) underestimates: 35.3 μT [30.2 - 40.7] for site 1 and 35.5 μT [31.9 - 38.6] for site 4.

Site 4 was drilled in three separate rows to assess the influence of cooling rate. The top row (37.2 μT [29.6 - 45.2]) and bottom row (36.3 μT [33.1 - 39.4]) yielded the best results, the IGRF value of the PI falling within the error bounds of one standard deviation. Site 9 (1971, crater) also yielded a PI within 10% of its IGRF value, but showed large scatter and thus a very large standard deviation: 35.3 μT [20.5 - 49.5].

Site 7 (1949, sea) showed the best linear fit and the least scatter of all sites (R^2 = 0.977), but yielded a large (+21.8%) overestimate of the IGRF intensity. Site 15 also showed a nice plot (R^2 = 0.929) combined with a large (+52.8%) overestimate. Sites 8 (1971, east), 11 (1949, crater) and 13 (1949, east) yielded technically acceptable results, but produced large underestimates of -32.2, -46.4 and -38.8%, respectively.

For the other sites, the accuracy of the obtained PI cannot definitively be assessed. However, based on their close proximity in time, sites 3 (1712), 5 (1677) and 6 (1646) would be expected to yield similar results and in fact they did: 37.2 μT [25.2 - 47.7] for site 3, 35.1 μT [25.8 - 45.7] for site 5 and 43.5 μT [35.6 - 53.9] for site 6. The scatter observed for site 2 (1585) makes it impossible to extract a PI with any degree of confidence.

Site 12 (1470-92) yielded a PI of 29.0 μT [25.2 - 32.6], which seems plausible if somewhat low. The two oldest sites — site 10 (1.09 ± 0.05 ka) and site 14 (3.2 ± 0.01 ka) — yielded technically good results (R^2 > 0.9) and plausible PIs of 38.6 μT [33.4 - 44.1] and 44.1 μT [40.3 - 48.4], respectively.

Looking at **table 5.5**, it would seem that — at least for the IGRF sites — sites with high Curie temperatures generally yield results within 10% of the IGRF value, whereas sites with low Curie temperatures tend to yield large (up to 50%) under- or overestimates.

Table 5.5 Parameters and results for the MSP-DB protocol. T_{MSP} is the temperature at which the MSP experiments were carried out, IEF the intensity error fraction, *n* the number of specimens used in the linear regression and R^2 the coefficient of determination (the goodness of the linear regression).

Site	IGRF (μT)	T_c (°C)	T_{MSP} (°C)	PI (μT)	IEF (%)	n	R^2
1	**39.4**	540	200	35.5 [30.2 - 40.7]	-9.9	9	0.921
2	**-**	540	200	52.3 [36.4 - 131.0]	-	7 (2)	0.683
3	**-**	210	100	37.2 [25.2 - 47.7]	-	7 (2)	0.848
4 - T	**39.1**	540	200	37.2 [29.6 - 45.2]	-4.6	6	0.934
4 - M	**39.1**	540	200	32.9 [23.8 - 40.9]	-15.9	6	0.925
4 - B	**39.1**	540	200	36.3 [33.1 - 39.4]	-7.2	6	0.987
4 - all	**39.1**	540	200	35.3 [31.9 - 38.6]	-9.7	18	0.910
5	**-**	120	100	35.1 [25.8 - 45.7]	-	8 (1)	0.821
6	**-**	540	200	43.5 [35.6 - 53.9]	-	8 (1)	0.874
7	**39.4**	90	100	53.2 [51.1 - 55.6]	+35.0	9	0.992
8	**39.1**	135	100	26.5 [21.4 - 30.7]	-32.2	7 (2)	0.965
9	**39.1**	540	200	35.3 [20.5 - 49.5]	-9.7	8 (1)	0.752

Site	IGRF (μT)	T_c (°C)	T_{MSP} (°C)	PI (μT)	IEF (%)	n	R^2
10	**-**	475	200	38.6 [33.4 - 44.1]	-	8	0.943
11	**39.4**	80	100	21.1 [16.4 - 24.6]	-46.4	11 (3)	0.910
12	**-**	280	200	29.0 [25.2 - 32.6]	-	8 (1)	0.965
13	**39.4**	100	200	24.1 [13.1 - 31.4]	-38.8	9	0.857
14	**-**	370	200	44.1 [40.3 - 48.4]	-	9	0.958
15	**39.4**	90	100	60.2 [54.3 - 68.9]	+52.8	10 (1)	0.929

5.2.3.2 MSP-DSC

A summary of the MSP-DSC results can be found in **table 5.6**; some plots are shown in **fig. 5.13**. All plots and calculated parameters can be found in **Appendix V**. Outliers, which were not taken into account in the linear regression, are marked in red. For some specimens, the magnetisation obtained after step 2 (antiparallel field) was antiparallel to the initial NRM (e.g. **fig. 5.13**, left). This was detected and corrected for by multiplying m_2 by the normalised dot product of m_0 and m_2 in the Scilab code calculating the DSC-ratio and other parameters.

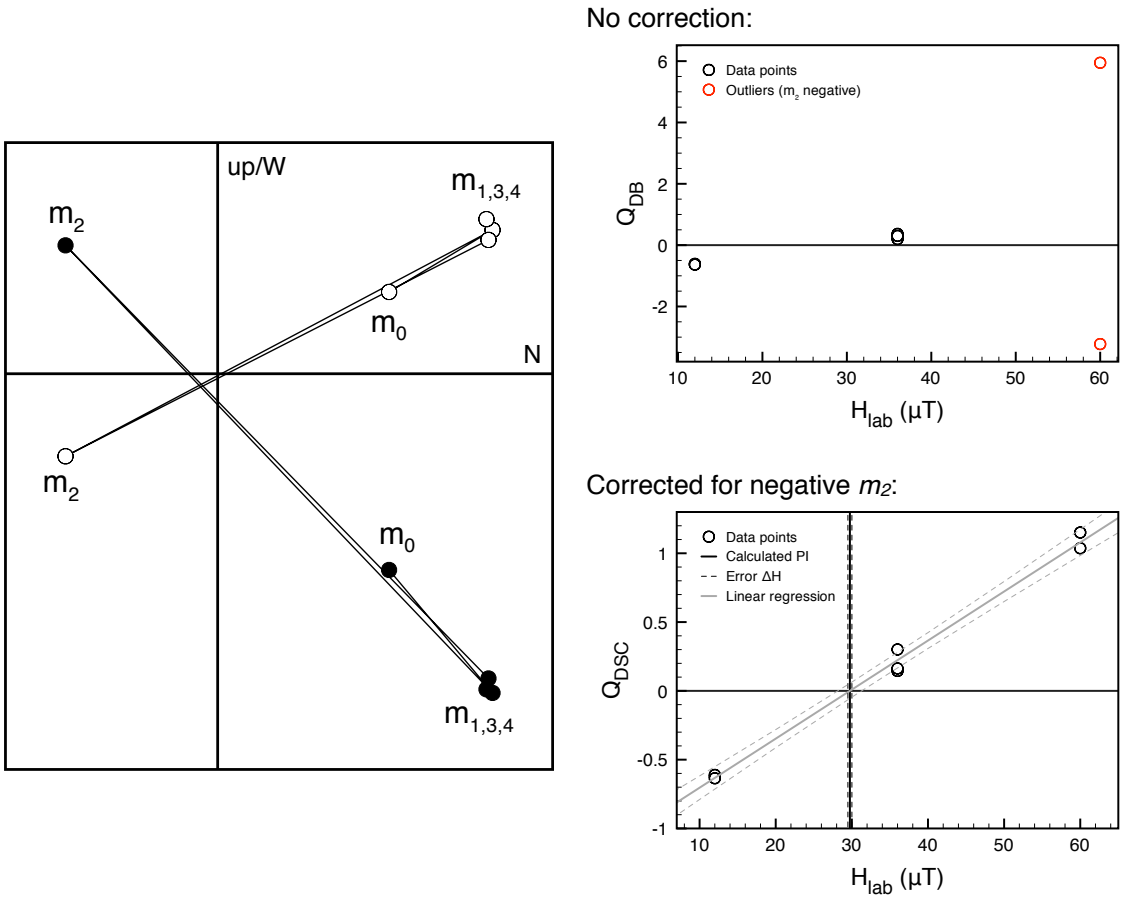

Fig. 5.13 Example of a specimen (site 12) for which m_2 is negative. *Left:* Zijderveld diagram, showing that the measured magnetisation flips direction after the step in negative field m_2. *Right:* Q_{DSC} plotted against H_{lab} without correction (m_2 always positive) and with correction (m_2 allowed negative).

Fabian and Leonhardt (2010) make two claims concerning the MSP-DSC protocol: compared to MSP-DB it should lower the overestimates and it should reduce scatter. Unfortunately, of the eight 20th-century flows, only two yielded overestimates, whereas the other six produced underestimates. In principle, the DSC protocol is not suitable for underestimates, but I applied it anyway to see what would happen. Looking at the last column of **table 5.6**, it can be seen that most PIs obtained using MSP-DSC are indeed lower than those found using MSP-DB by 3 to 35%. The PIs obtained for the two overestimates (sites 7 and 15) using the DB protocol were reduced by 9.8 and 15%, respectively, still yielding overestimates of 21.8 and 31.5% compared to their IGRF values (e.g. **fig. 5.14a**).

In four cases (sites 9, 11, 12 and 13) the PIs found using MSP-DSC are a few percent (1 to 3 µT) higher than those obtained using the DB protocol. These cases are usually related to a reduction in scatter. This is best seen for site 9 (1971, crater), for which the scatter in data points at 12 and 60 µT was considerably reduced by the DSC protocol, although the scatter at 36 µT was increased (see **fig. 5.14b**). The PI obtained for site 9 is within 4% of its IGRF value.

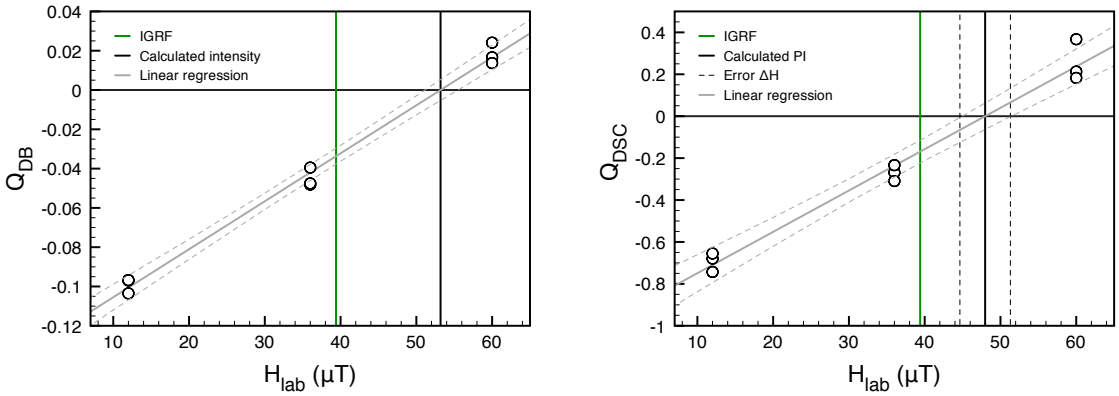

Fig. 5.14a *Left:* MSP-DB plot for site 7 (1949, sea), which shows a substantial overestimate. *Right:* MSP-DSC plot for the same site. The overestimate is reduced, but the resulting PI is still high.

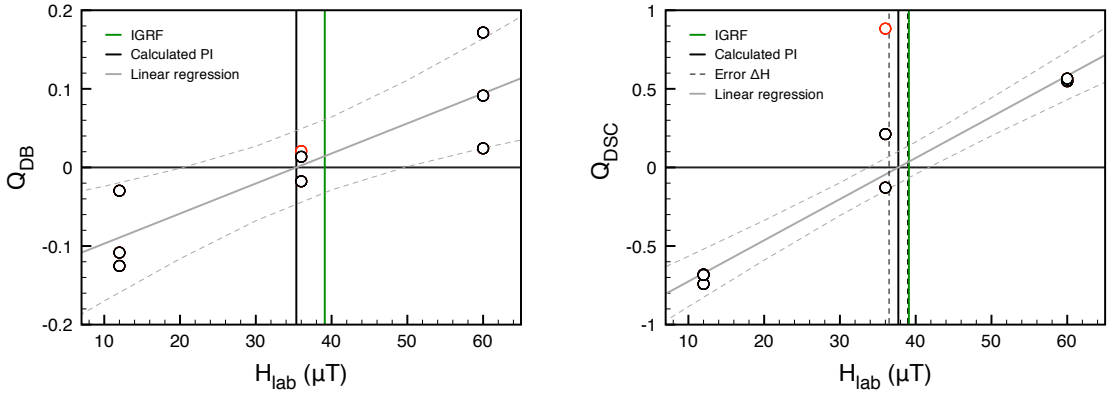

Fig. 5.14b *Left:* MSP-DB plot for site 9 (1971, crater). *Right:* MSP-DSC plot for the same site. The scatter in the data points at 12 and 60 µT is reduced considerably, although the scatter at 36 µT is increased. The resulting PI is within 5% of the IGRF.

Table 5.6 Results and parameters for the MSP-DSC protocol. ΔH is the intensity error that can be calculated using from **eq. 5.14**. ΔPI is the normalised difference between the PIs obtained using the DSC and DB protocol: $(PI_{DSC} - PI_{DB}) / PI_{DB}$.

Site	**IGRF** (μT)	**T_c** (°C)	**T_{MSP}** (°C)	**PI** (μT)	**ΔH** (μT)	**IEF** (%)	**n**	**R^2**	**ΔPI** (%)
1	**39.4**	540	200	34.1 [28.6 - 39.2]	1.09	-13.5	9	0.924	-3.9
2	**-**	540	200	44.4 [32.4 - 69.9]	5.52	-	7 (2)	0.785	-15.1
3	**-**	210	100	24.3 [17.5 - 29.4]	2.80	-	7 (2)	0.962	-34.7
4 - T				29.5 [22.0 - 35.6]	3.53	-24.6	6	0.953	-20.7
4 - M	**39.1**	540	200	27.8 [20.0 - 33.8]	4.48	-28.9	6	0.953	-15.5
4 - B				29.9 [22.6 - 35.9]	5.05	-23.5	6	0.953	-17.6
4 - all				29.1 [26.4 - 31.6]	2.43	-25.6	18	0.947	-17.6
5	**-**	120	100	31.0 [22.7 - 38.6]	3.00	-	8 (1)	0.868	-11.7
6	**-**	540	200	37.4 [35.2 - 39.7]	2.32	-	8 (1)	0.989	-14.0
7	**39.4**	90	100	48.0 [45.0 - 51.4]	3.33	+21.8	9	0.977	-9.8
8	**39.1**	135	100	25.6 [17.3 - 31.5]	1.07	-34.5	7 (2)	0.929	-3.4
9	**39.1**	540	200	37.7 [33.9 - 41.7]	1.22	-3.6	8 (1)	0.967	+6.8
10	**-**	475	200	26.7 [20.6 - 32.0]	5.37	-	8	0.950	-30.8
11	**39.4**	80	100	22.1 [14.6 - 27.6]	0.36	-43.9	11 (3)	0.925	+4.7
12	**-**	280	200	29.7 [28.2 - 31.3]	0.26	-	8 (1)	0.993	+2.4
13	**39.4**	100	200	26.0 [18.1 - 31.9]	2.25	-34.0	9	0.901	+7.9
14	**-**	370	200	32.4 [28.3 - 36.2]	6.03	-	9	0.955	-26.5
15	**39.4**	90	100	51.8 [47.4 - 57.5]	3.95	+31.5	10 (1)	0.944	-14.0

The phenomenological model of the DSC protocol allows to calculate several other parameters, such as μ_{DS}, which gives an estimate of the domain state and ε_{alt}, which estimates the alteration between steps 1 and 4. The phenomenological model can also be used to estimate the domain-state error and the alteration error for each specimen. (See **Appendix VI** for the equations.) The average value of μ_{DS} and its standard deviation for each site is plotted in **fig. 5.15**; ε_{alt} is shown in **fig. 5.16**. The average value of μ_{DS} is lower than 0.2 for all sites, but because of the large within-site variation the standard deviation can be very large. The absolute difference between measurements 1 and 4, ε_{alt}, is less than 8% for all sites and for most sites less than 5%, as would be expected, considering that the temperature used in the MSP experiments was chosen below the specimens' alteration temperatures.

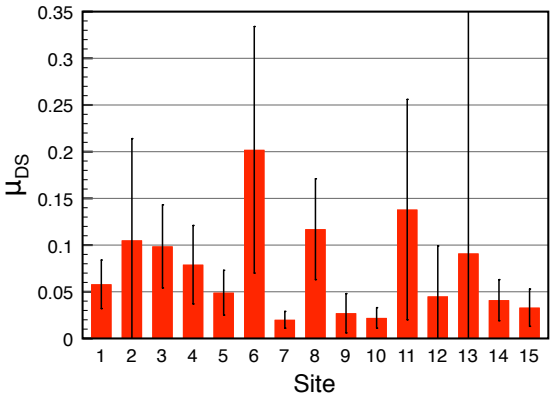

Fig. 5.15 Average values of μ_{DS}, a parameter that estimates the domain state, and its standard deviation. The μ_{DS} ratio estimates the relative pTRM tail.

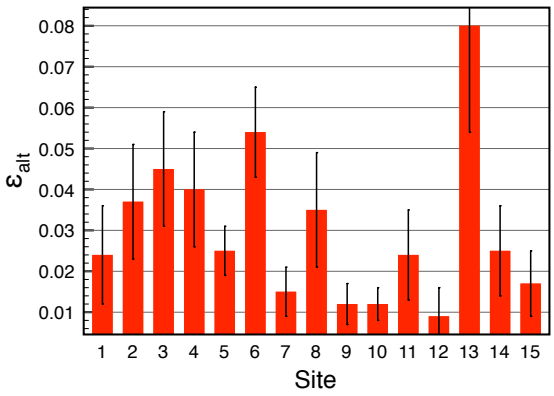

Fig. 5.16 The average relative alteration error ε_{alt} between steps 1 and 4 and its standard deviation.

The average values and standard deviations of the alteration error $\Delta Q_{DSC,alt}$ and the domain-state error $\Delta Q_{DSC,ds}$ are plotted in **fig. 5.17a-b**. Values for separate specimens can be found in **Appendix V**. Because there was a lot of variation between specimens of the same site, standard deviations are quite large. **Fig. 5.17** shows that the alteration error is in general about four times larger than the domain-state error. Generally speaking, sites that show a small (large) alteration error, also show a small (large) domain-state error.

The total error $\Delta Q_i = \sqrt{\Delta Q_{DSC,alt}^2 + \Delta Q_{DSC,ds}^2}$ is most useful for separate specimens. Looking at the MSP results in **Appendix V**, it is apparent that in many (though not all) cases outliers have relatively high ΔQ_is. Examples are sites 2 (1585), 5 (1677), 9 (1971, crater) and 11 (1949, crater). On the other hand, high values of ΔQ_i do not always translate to outliers, see e.g. sites 3 (1712), 10 (1.09 ± 0.05 ka), 13 (1949, east) and 14 (3.2 ± 0.01 ka).

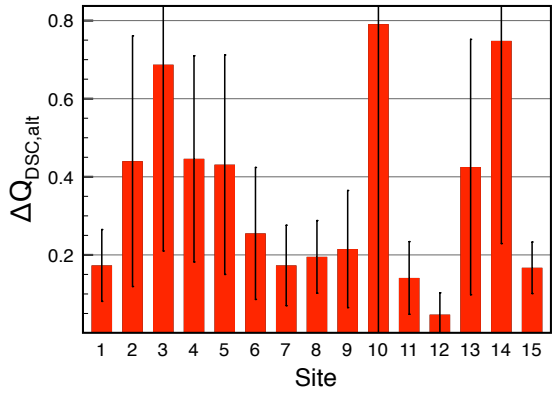

Fig. 5.17a The average alteration error $\Delta Q_{DSC,alt}$ and its standard deviation for each site.

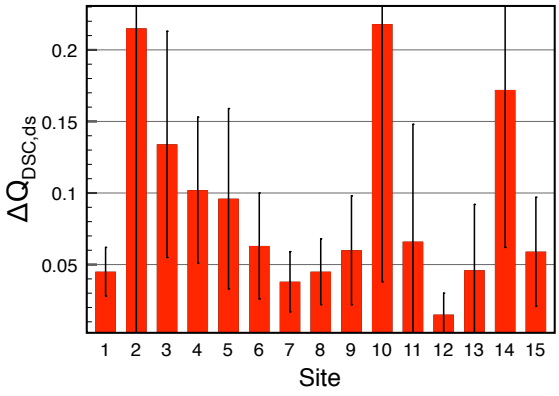

Fig. 5.17b The average domain state error $\Delta Q_{DSC,ds}$ and its standard deviation for each site.

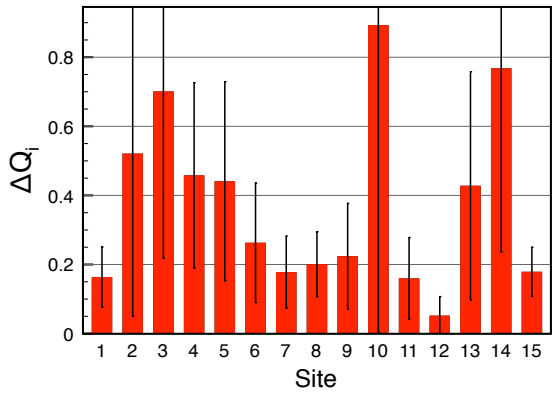

Fig. 5.17c Average total error ΔQ_i per site and its standard deviation.

5.2.3.3 Full TRM

I also applied the MSP-DB protocol to nine specimens of site 11, which had been overprinted with a known field of 40 µT at a temperature below its alteration temperature. The resulting plot is shown in **fig. 5.18**. Whereas site 11 in the 'real' MSP-DB experiment yielded a large (-46.4%) underestimate, the full-TRM experiment yielded an intensity of 40.2 µT, an intensity error fraction of only 0.5%. This may indicate that the NRM is not an uncontaminated TRM or that some alteration occurs during the first heating step. Because the first heating step in this case is the overprinting step, such alteration should not influence the MSP-DB protocol, whereas in the 'real' MSP-DB experiment the alteration takes place during the actual PI determination and might influence the results.

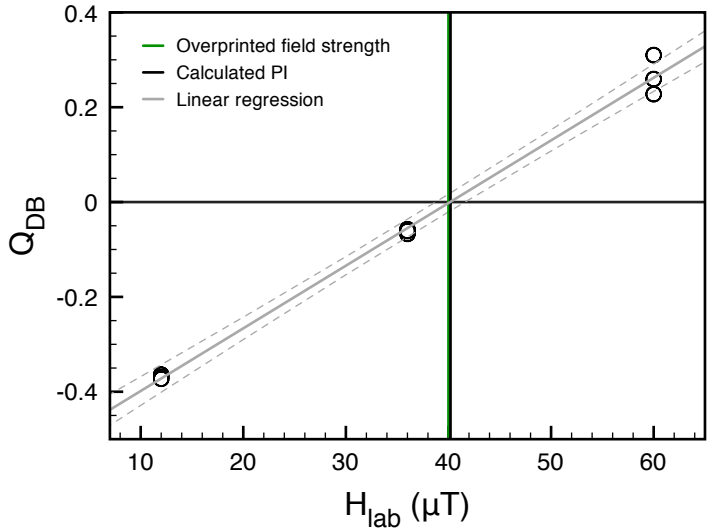

Fig. 5.18 MSP-DB plot of site 11 (1949 flow, crater), which had been given a full pTRM of 40 µT (green line). The calculated intensity (black line) very nearly overlaps.

5.2.4 Summary

PI results obtained through the three different methods are summarised in **table 5.7**. For the sites within the IGRF range, PIs within 10% of their IGRF values are marked in bold and the result closest to the IGRF is underlined. Looking at the 20th-century sites, it is apparent that results from the multispecimen and Thellier-Thellier methods vary widely. In the MSP protocol, some sites (1, 4 and 9) yield PIs very close to their IGRF values, whereas others produce large over- (sites 7 and 15) or underestimates (sites 8, 11 and 13). The Thellier-Thellier method yielded a few PIs very close to the IGRF values (sites 4, 9 and 15), while other -- technically acceptable -- plots yielded large underestimates (sites 7, 8 and 11). The microwave method, on the other hand, always yields PIs within 15% of their IGRF values if the plots are technically acceptable.

Table 5.7 Summary of the PI results for all three methods.

Site	IGRF	Thellier (success rate)	Microwave (success rate)	Multispecimen DB / DSC
1 (1949)	**39.4**	failed	failed	**35.6** / 34.1
2 (1585)	**-**	-	43.5 (1/1)	52.3 / 44.4
3 (1712)	**-**	31.7 (2/2)	43.0 (1/1)	37.2 / 24.3
4 (1971)	**39.1**	**37.2** (5/6)	**38.5** (2/3)	**35.3** / 29.1
5 (1677)	**-**	-	-	35.1 / 31.0
6 (1646)	**-**	55.8 (1/3)	-	43.5 / 37.4
7 (1949)	**39.4**	30.8 (1/3)	failed	53.2 / 48.0
8 (1971)	**39.1**	32.0 (1/3)	failed	26.2 / 25.6
9 (1971)	**39.1**	**41.8** (3/3)	**40.0** (2/2)	failed / **37.7**
10 (1.09 ka)	**-**	37.4 (2/3)	-	38.6 / 26.7
11 (1949)	**39.4**	29.0 (3/3)	44.1 (1/1)	21.1 / 22.1
12 (1470-92)	**-**	36.1 (1/3)	44.1 (1/1)	29.0 / 29.7
13 (1949)	**39.4**	failed	43.8 (1/1)	24.9 / 26.0
14 (3.2 ka)	**-**	-	-	44.1 / 32.4
15 (1949)	**39.4**	**38.9** (3/3)	**42.9** (1/1)	60.4 / 51.7

6 DISCUSSION

In this chapter I will discuss the results from the previous chapters. In the first section I will discuss possible influences on the reliability of PI measurements, such as (chemical) alteration, domain state and cooling rate effects. In the second section I will focus on the PI methods themselves.

6.1 Sources of error

6.1.1 Chemical alteration

Chemical alteration is an important cause of error in PI experiments. In Thellier-Thellier and microwave experiments a specimen's ability to gain a pTRM may change due to alteration, which may be visible as sagging in its Arai plot. In contrast to Thellier-type experiments, MSP protocols do not incorporate pTRM checks to assess alteration. By
Using Fabian and Leonhardt (2010)'s phenomenological model, two parameters related to chemical alteration can be calculated. The first is the alteration between steps 1 and 4 ε_{alt} and the second the alteration error $\Delta Q_{DSC,alt}$. Because the MSP experiments were carried out at temperatures well below a site's alteration temperature, minimal chemical alteration would be expected. And indeed the magnetisation measured after step 4 differs from that measured after step 1 by less than 8% for all sites and less than 5% for most. No correlation between high (low) alteration temperatures evident in Curie or susceptibility-versus-temperature diagrams and high (low) values of ε_{alt} and $\Delta Q_{DSC,alt}$ can be observed, again in line with expectations. For example site 7 (1949, sea) shows strong alteration at temperatures > 250°C, but yields low values of ε_{alt} and $\Delta Q_{DSC,alt}$.

Generally, low (high) values of ε_{alt} seem to be correlated with low (high) values of $\Delta Q_{DSC,alt}$, with the exception of sites 10 (1.09 ± 0.05 ka) and 14 (3.2 ± 0.01 ka), which show a markedly higher $\Delta Q_{DSC,alt}$ than ε_{alt} and sites 6 (1646) and 13 (1949, east), which show a markedly higher value of ε_{alt} than of $\Delta Q_{DSC,alt}$. But as the standard deviations in $\Delta Q_{DSC,alt}$ are much larger than for ε_{alt}, it is difficult to draw any definitive conclusions. Additionally, the value of ε_{alt} is not only influenced by alteration between steps 1 and 4, but also by measurement uncertainties (e.g. alignment in the oven or the DC SQUID magnetometer, oven temperature, oven field, etc.).

Both ε_{alt} and $\Delta Q_{DSC,alt}$ assess alteration that occurred after step 1, but it may be that most alteration (chemical or otherwise) does in fact take place during the first heating. This alteration cannot be assessed by adding in additional heating steps. In this respect, the full-TRM experiment is very interesting. Site 11 (1949, crater) yielded a large (-46.4%) underestimate in the MSP-DB experiment, but produced a 'PI' within 1% of the overprinted intensity in the full-TRM experiment. Because the specimens were overprinted at a temperature below their alteration temperature, the specimens should not have altered chemically. Nevertheless, that a site that produces such a large undererestimate in MSP-DB yields very nearly exactly the right intensity in a full-TRM experiment suggests either that the NRM was not an uncontaminated TRM or that some alteration has occurred. This alteration must have occurred during the first heating step, i.e. when the specimens were overprinted. In an Arai plot, such alteration may be visible as an offset: the linear regression does not cross the vertical axis at (0, 1). However, site 11 (1949) yielded a large

underestimate, but the linear regression through the data points shows no appreciable offset.

Table 6.1 Average values and standard deviations of ε_{alt} and $\Delta Q_{DSC,alt}$.

	ε_{alt}		$\Delta Q_{DSC,alt}$	
Site	**Average**	**σ**	**Average**	**σ**
1 (1949)	0.024	0.012	0.173	0.092
2 (1585)	0.037	0.014	0.440	0.321
3 (1712)	0.045	0.014	0.687	0.477
4 (1971)	0.040	0.014	0.446	0.264
5 (1677)	0.025	0.006	0.431	0.281
6 (1646)	0.054	0.011	0.255	0.169
7 (1949)	0.015	0.006	0.173	0.103
8 (1971)	0.035	0.014	0.195	0.093
9 (1971)	0.012	0.005	0.215	0.150
10 (1.09 ka)	0.012	0.004	0.791	0.833
11 (1949)	0.024	0.011	0.141	0.093
12 (1470-92)	0.009	0.007	0.047	0.056
13 (1949)	0.080	0.026	0.425	0.327
14 (3.2 ka)	0.025	0.011	0.748	0.519
15 (1949)	0.017	0.008	0.167	0.066

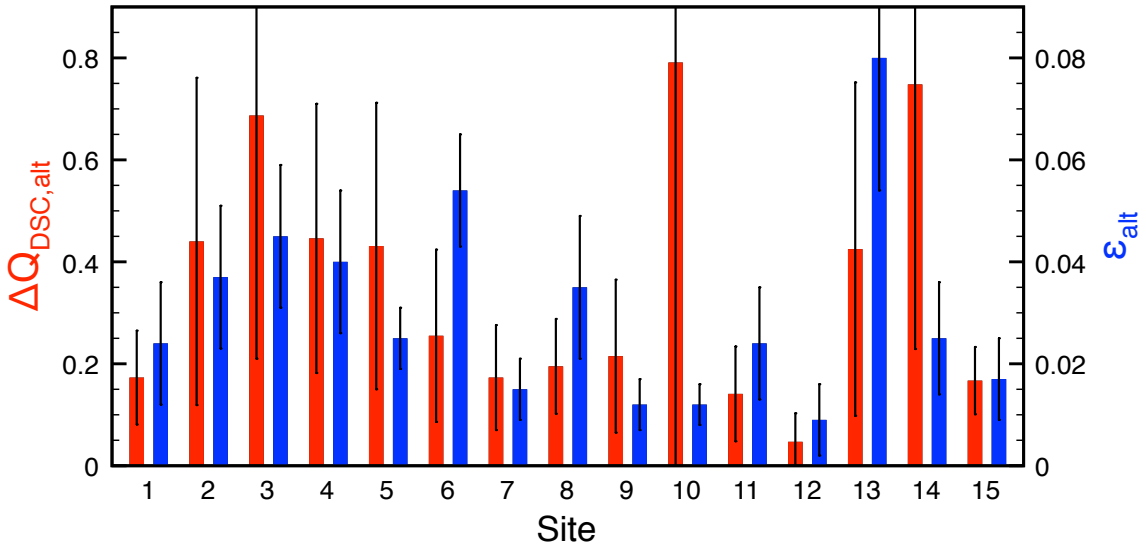

Fig. 6.1 Average values of ε_{alt} (blue), a measure of the alteration between steps 1 and 4, and $\Delta Q_{DSC,alt}$ (red), the alteration error.

6.1.2 Domain state effects

The phenomenological model proposed in Fabian and Leonhardt (2010) allows to calculate several parameters related to domain state effects: μ_{DS}, which estimates the domain state, and $\Delta Q_{DSC,ds}$, which is the domain state error for a single specimen. Values of these parameters for single specimens can be found in **Appendix V**; their averages and standard deviations are summarised in **table 6.2**. In Fabian and Leonhardt (2010), μ_{DS} was lowest for (artificial) specimens closest to SD, increases for PSD grains and decreases again for MD specimens. In order to compare my results to table 1 in Fabian and Leonhardt (2010), I ordered the sites based on their domain state as estimated from the Day plot shown in **fig. 4.11**. The results are plotted in **fig. 6.2a-b**. Fabian and Leonhardt used the amount of sagging in Thellier-Thellier data as indicator of domain state.

In general, a similar trend as in Fabian and Leonhardt (2010) can be observed: the three sites closest to SD (sites 9, 7 and 15) yielded low values of μ_{DS} whereas the sites more near the middle of the PSD range of the Day plot tended to yield the highest values, with the notable exception of sites 10 and 12. μ_{DS} decreases again for the sites closest to MD: sites 5 and 14. The domain state error $\Delta Q_{DSC,ds}$ does not seem to show any trend, although the four sites closest to SD all exhibit relatively low values of $\Delta Q_{DSC,ds}$. For both parameters standard deviations are large, making it difficult to interpret the data.

Table 6.2 Values of μ_{DS} and $\Delta Q_{DSC,ds}$ sorted by domain state as obtained from the Day plot in **fig. 4.13**.

	μ_{DS}		$\Delta Q_{DSC,ds}$		
Site	**Average**	**σ**	**Average**	**σ**	
9 (1971)	0.027	0.021	0.060	0.038	close to SD
7 (1949)	0.020	0.009	0.038	0.021	
15 (1949)	0.033	0.020	0.059	0.038	
1 (1949)	0.058	0.026	0.045	0.017	
2 (1585)	0.105	0.109	0.215	0.392	
3 (1712)	0.099	0.045	0.134	0.079	
6 (1646)	0.202	0.132	0.063	0.037	
4 (1971)	0.079	0.042	0.102	0.051	↓
13 (1949)	0.091	0.581	0.046	0.046	
10 (1.09 ka)	0.022	0.011	0.218	0.180	
11 (1949)	0.138	0.118	0.066	0.082	
12 (1470-92)	0.045	0.054	0.015	0.015	
8 (1971)	0.117	0.054	0.045	0.023	
5 (1677)	0.049	0.024	0.096	0.063	
14 (3.2 ka)	0.041	0.022	0.172	0.110	close to MD

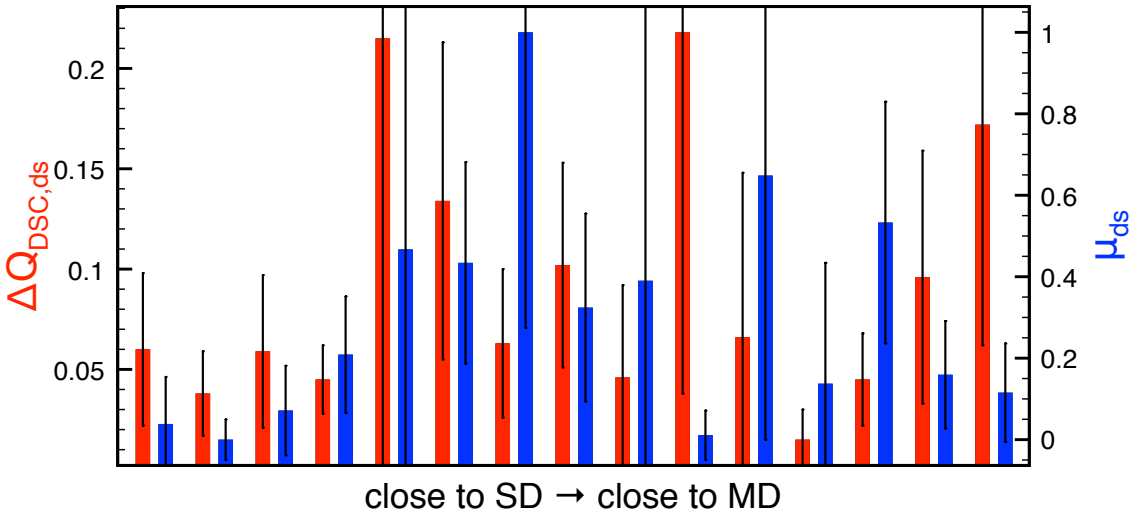

Fig. 6.2 Average values of μ_{alt} (blue), which estimates domain state, and $\Delta Q_{DSC,ds}$ (red), the domain-state error.

Another way to assess domain-state effects is by looking at a site's location on a Day plot. **Fig. 6.3** shows the same plot as in **fig. 4.11**, but now indicating over- and underestimates. The site closest to SD — site 9 (1971, crater) — is also the site that yielded the PI closest to the IGRF. However, sites 1 (1949) and 4 (1971, west), which also yielded small (< 10%) underestimates, are located more towards the MD part of the plot, whereas the two large overestimates are both very close to SD. The three large underestimates are all located more towards the MD part of the plot. From this plot, there would not seem to be a clear relation between a site's location on a Day plot and its MSP results.

Comparing a site's location on a Day plot before and after heating (**fig. 4.12**) yields information on a site's change in domain state due to heating. Except for site 1 (1949), there seems to be a trend toward more SD behaviour. In particular sites 7 (1949, sea) and 9 (1971, crater) show a significant shift. However, there does not seem to be a link between over- or underestimates in the MSP method and changes in domain state as evident from the Day plot. Sites 7, 9 and 15 (1949) show a similar shift in their M_r / M_s ratios, but sites 7 and 15 yielded a large overestimate in the MSP experiments (both DB and DSC), whereas site 9 yielded a PI within 5% of the IGRF value using the DSC protocol. Site 1 and site 4 (1971, west) both produced PIs within 10% of the IGRF values using MSP-DB, but site 4 shows no significant change in domain state and site 1 would seem to shift a bit towards more MD behaviour, although scatter makes it difficult to draw any definitive conclusions.

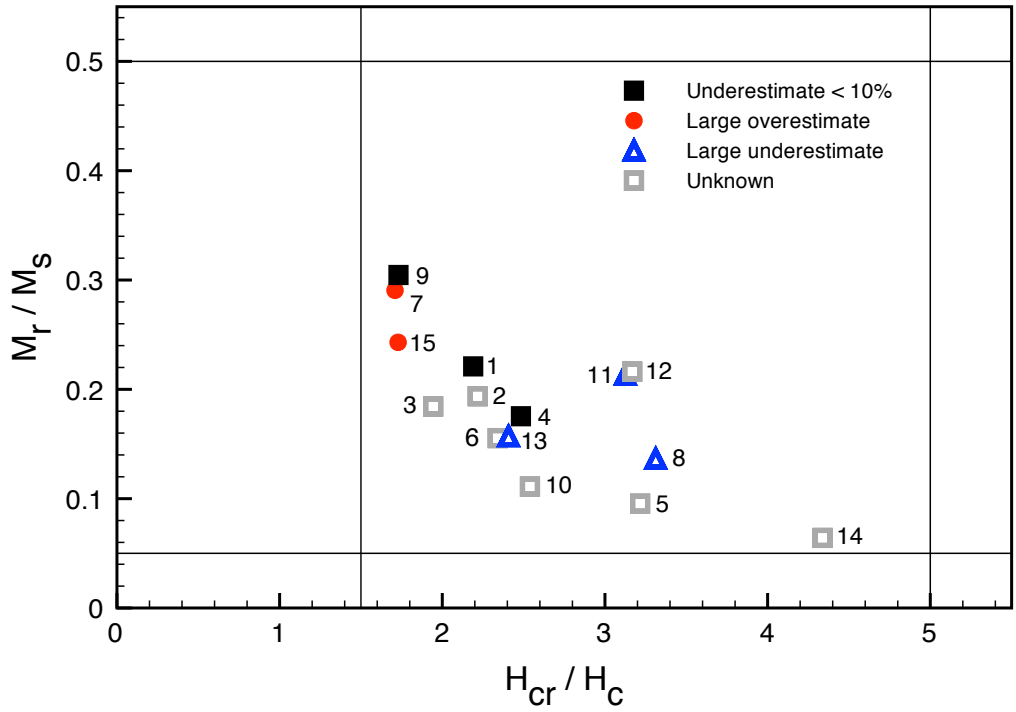

Fig. 6.3 Day plot indicating over- and underestimates. Sites shown in grey are outside the range of the IGRF.

6.1.3 Cooling rate effects

To assess the effect of cooling rate, site 4 (1971, west) was drilled in three rows at increasing distances from the top of the flow. (See **fig. 3.2**.) Results for the different methods are summarised in **table 6.3**. The best results would be expected for cooling rates close to the one in the lab. As the top of the flow cooled fastest, specimens drilled near the top of the flow should yield better results than specimens drilled further away from the top.

For both the Thellier-Thellier and the microwave method, the bottom row (slowest cooling) yielded the best results, but as only one or two specimens were measured for each row in the Thellier-Thellier and microwave experiment, this may be incidental. The MSP protocols (**fig. 6.4a-b**) shows that there seems to be no significant correlation between the distance from the top of the flow and the intensity error fraction. Both the top and bottom rows yielded PIs within 10% of the IGRF, whereas the PI obtained for the middle row underestimates the field by nearly 16%. However, the middle row also showed the largest amount of scatter, which may have influenced results.

Table 6.3 PI results per drilling row for site 4 (1971, west).

Site	IGRF	Thellier-Thellier		Microwave		MSP-DB		MSP-DSC	
		PI (μT)	IEF (%)	PI (μT)	IEF (%)	PI (μT)	IEF (%)	PI (μT)	IEF (%)
4 - T		35.9	-8.2	34.4	-12.0	37.2	-4.6	29.5	-20.7
4 - M	**39.1**	36.7	-6.1	-	-	32.9	-15.9	27.8	-15.5
4 - B		40.8	+4.3	42.6	+9.0	36.3	-7.2	29.9	-17.6

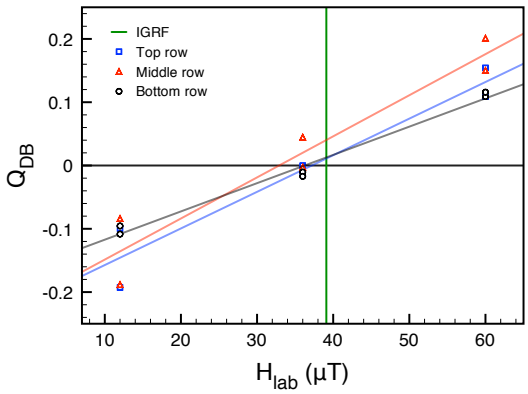

Fig. 6.4a MSP-DB plot for site 4 (1971, west), separated by drilling row.

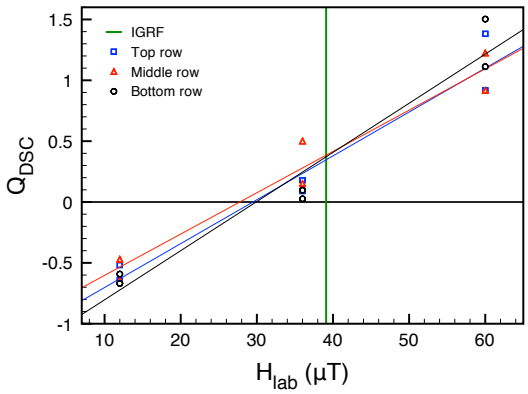

Fig. 6.4b MSP-DSC plot for site 4 (1971, west), separated by drilling row.

6.2 Palaeointensity methods

6.2.1 Thellier-Thellier

Many sites lose less than 30% — and often even less than 10 to 20% — of their NRM during the experiments, which were all carried out at temperatures below the sites' alteration temperatures. A low *f*-value (i.e. fraction NRM lost in the interval used to calculate the linear regression) makes the results somewhat less reliable, because it is impossible to tell whether the plot actually *is* a straight line or if it would have shown sagging at higher temperatures. For example site 13 (1949, east) shows strong sagging, but if only the first four data points had been measured, it would have seemed like a straight line. According to criteria formulated by Coe *et al*. (1978) an *f*-value of 0.15 or higher is acceptable, but Biggin and Thomas (2003) suggest that the minimum required *f*-value should be at least 0.5 to overcome the problem of overestimation caused by insufficient representation of a concave-up curve.

However, from my results it would seem that even high *f*-values, straight lines and good pTRM checks do not always produce good PIs. The best example of this is site 11 (1949,

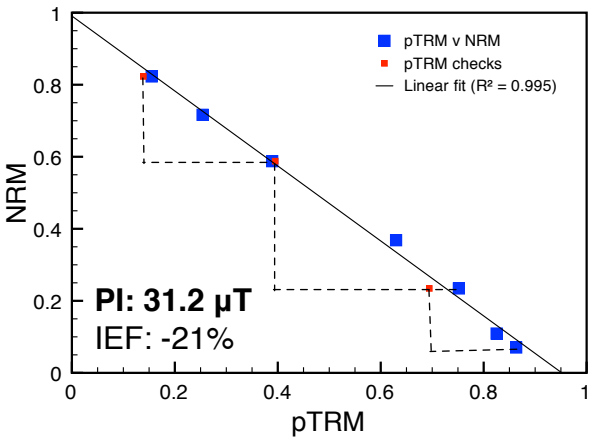

Fig. 6.5 Thellier-Thellier Arai plot for site 11 (1949, crater), normalised by the specimen's NRM. This plot was obtained using the Aitken parallel protocol and a laboratory field of 30 μT.

crater; see **fig. 6.5**). Its Arai plot is technically very good: > 90% NRM lost, the plot does not show sagging and the first two pTRM checks are very good. Nevertheless, all three site 11 specimens produced large (> 20%) underestimates compared to the IGRF value of the PI. The full-TRM experiment performed on site 11 indicates that either some alteration takes place during the first heating or that its NRM is not an uncontaminated TRM. However, all three specimens used in the Thellier-Thellier experiment show a linear regression that crosses the vertical axis at or very near (0, 1), suggesting that no significant alteration occurred during the first heating step. As the first two pTRM checks are very good, it is unlikely that some gradual alteration process influenced the results. Therefore, it seems most likely that — at least in the case of site 11 — the discrepancy between the obtained PI and the IGRF value is caused by the NRM not being a pure TRM.

6.2.2 Microwave method

Proponents of the microwave method of determining PIs claim that by directly exciting the spins, the bulk sample experiences less heating, thus reducing the risk of chemical alteration due to heating (e.g. Walton et al., 1993; Hill, Shaw and Herrero-Bervera, 2005). As a specimen's temperature cannot be measured while the microwave system is switched on, it is impossible to know the maximum temperature the specimen is subjected to. (e.g. Walton et al., 1993). However, local melting can occur if microwave energy is focussed on an irregularity of the surface (e.g. Biggin, 2010).

An interesting test case is site 7 (1949, sea), which shows strong alteration at temperatures > 250°C, becoming appreciably more magnetic as a result. Its microwave and thermal NRM decay curves are plotted in **fig. 6.6**. It can be observed that at higher values of the power integral (the difference between the applied and reflected power) the NRM increases again. Comparing this curve to site 7's thermal NRM decay curve suggests that the specimen was heated to at least 250°C during the microwave demagnetisation.

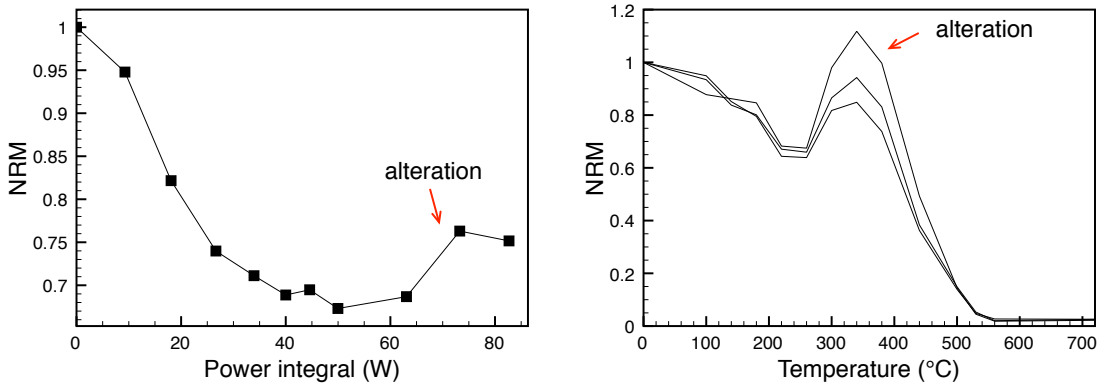

Fig. 6.6 *Left:* Microwave NRM decay curve showing alteration at a power integral higher than 60 W. *Right:* Thermal NRM decay curve, showing strong alteration at temperatures above 200°C.

6.2.3 Multispecimen method

The phenomenological model described in Fabian and Leonhardt (2010) predicts that PSD grains will always yield overestimates in MSP experiments. However, of my eight 20th-century sites, only two sites produced (large) overestimates, whereas the other six yielded underestimates. This may have something to do with chemical alteration, which is not taken into account by the model. Chemical alteration should be minimal, because the MSP experiment is carried out at a temperature below a site's alteration temperature, but magnetic alteration does occur and may have influenced the experiment, although there does not seem to be a link between over- or underestimates and a shift in hysteresis ratios.

Comparing a site's MSP-DB results to its Curie temperature, shows that high (540°C) Curie temperatures seem to be linked to PIs close to the IGRF (within 10%), whereas sites with low Curie temperatures produce large (up to 50%) over- or underestimates. As dark lavas may reach temperatures up to 60°C, sites with low Curie temperatures are likely to have been partially overprinted with the present-day field, but this should only affect the top few millimetres of a drilled core. Site 11 (1949, crater) has a T_c of 80°C and indeed shows an overprint, which is removed at 140°C. Overprints may be of some influence on PI measurements, but they are unlikely to be solely responsible for over- or underestimates of nearly 50%, considering the intensity of Earth's magnetic field has changed by less than 1 μT since 1949.

Applying the DSC protocol to the 20th-century sites shows that there does not seem to be a link between the amount by which the field is over- or underestimated and the amount of DSC correction. Sites 1 (1949) and 4 (1971, west) yielded PIs within 10% of the IGRF using the DB protocol, but while site 1 was corrected by only -3.9%, site 4 was corrected downward by -17.6%. The two large overestimates, sites 7 (1949, sea) and 15 (1949), were reduced by -9.8% and -14.0% respectively. In some cases the DSC protocol yielded a higher PI than the DB protocol, generally related to a reduction in scatter, e.g. site 9 (1971, crater).

6.2.4 Consistency between palaeointensity methods

PI results for the three different methods are summarised in **table 5.7**. Because the Thellier-Thellier and MSP methods are based on the same principle — a specimen's NRM is partially overprinted with a laboratory pTRM — comparable results would be expected. For sites 4 (1971, west), 9 (1971, crater) and 10 (1.09 ± 0.05 ka) PIs obtained using MSP and Thellier-Thellier are within a few percent of each other. Sites 8 (1971, east) and 11 (1949, crater) yielded underestimates using both methods, whereas site 7 (1949, sea) yielded a large overestimate using the MSP method and a large underestimate using the Thellier-Thellier method. Site 15 (1949) produced a large overestimate using the MSP protocol, but approximately the IGRF value using Thellier-Thellier.

Biggin (2010) states there is clear, statistically significant evidence that microwave PI experiments performed on igneous rocks tend to produce *lower* PI estimates than thermal Thellier-Thellier experiments. However, comparing the microwave method with the Thellier-Thellier method shows that the microwave method generally yields higher PIs, but as for most sites only one specimen was measured using the microwave method, this may not be significant. The slightly higher field used in the Thellier-Thellier experiment (30 μT) compared to that used in the microwave method (usually 25 μT) may have biased the

results to some extent. Microwave measurements performed using lower (higher) fields tended to produce higher (lower) PIs. For example site 9 yielded a PI of 42.5 μT when a field of 25 μT was used and a PI of 37.5 when a field of 40 μT was used.

The microwave method and MSP method agree to within a few percent for sites 4 (MSP-DB) and 9 (MSP-DSC), the microwave method yielding slightly higher results. For the other sites, results differed considerably. This is in contrast to results found by Böhnel et al. (2009) for Mexican lavas, in which both methods yielded well comparable results with the microwave method tending to yield slightly lower PIs than the MSP method. However, my microwave PIs are usually based on only one specimen per site, making it difficult to draw definitive conclusions.

Finally, comparing all three methods, it appears that if all three methods agree to within a few percent (sites 4 and 9), the obtained PIs are close to the IGRF value. The same might be said if two of the methods closely agree, such as for site 15. If the three methods do not agree, the microwave method tends to produce the best result (sites 11 and 13).

Based on this conclusion, the obtained PIs are plotted against time in **fig. 6.7**. Sites or flows that were averaged over three methods (and multiple sites) are indicated in green; PIs based on two measurements are shown in blue. The PIs in grey are based on only one measurement, if possible that obtained in using the microwave method, as that method yielded the most reliable results for the 20th-century sites. PIs obtained for the 1470-92, 1585 and 1712 flows are consistently higher than those obtained for the 1949 and 1971 flows, but as the PIs for the older flows are based on just one or two measurements, this is a very tentative result.

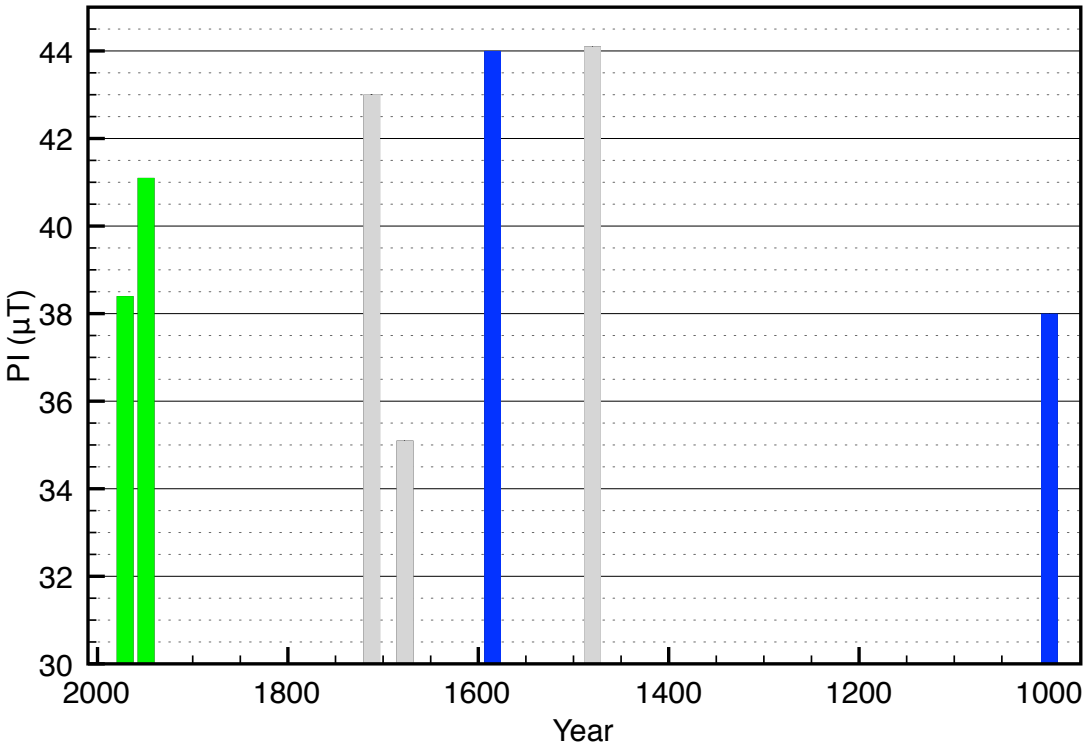

Fig. 6.7 Calculated PIs against time. Green bars indicated PIs based on three or more successful measurements, blue bars indicate PIs averaged over two succesful measurements and grey bars indicate PIs based on just one successful measurement. If two or more methods agreed to within a few μT, the resulting PIs were averaged. If the three methods disagreed, only the value for the microwave method was plotted, as these yielded the best results for the 20th-century sites. Site 5 (1677)'s PI is the value obtained using MSP-DB.

7 CONCLUSIONS

The Thellier-Thellier method yielded very variable results. Technically acceptable Arai plots some times produced PIs within 5% of the IGRF, but also produced large (> 20%) underestimates. The microwave method, on the other hand, always yielded results within 12% of the IGRF if the Arai plot was technically acceptable. The MSP protocol yielded underestimates for six out of eight sites within the IGRF, whereas the phenomenological model by Fabian and Leonhardt (2010) predicts overestimates for PSD grains. The three sites with high (540°C) Curie temperatures all yielded small (< 10%) underestimates, whereas the five sites with low (80-130°C) Curie temperatures yielded large (up to 50%) under- or overestimates. The domain-state-corrected protocol proposed by Fabian and Leonhardt (2010) promises to reduce overestimates and decrease scatter. However, the two overestimates were reduced to some extent, but still overestimated the palaeofield by more than 20%. Scatter was in some cases strongly reduced, although in some cases data points that were acceptable in MSP-DB became outliers in MSP-DSC. The full-TRM experiment indicates that (chemical or magnetic) alteration during the first heating may be an important factor.

Comparing results from the three different methods for the eight IGRF sites, it seems that if all three methods agree to within percent, the resulting PI is also within a few percent of the IGRF. This may also be the case if two out of three methods are in close agreement. If the three methods yield inconsistent results, the microwave method tends to produce the best results.

ACKNOWLEDGEMENTS

During my master's research project, there have been a number of people who helped me. I am very grateful for their help and support.

First of all, I would like to thank the people at Paleomagnetic Laboratory 'Fort Hoofddijk' who helped and encouraged me during my time within their department. In particular Lennart de Groot, who supervised my master's research project. I would like to thank him and Prof.dr. Cor Langereis for giving me the opportunity to do exciting things like going to the University of Liverpool for measurements and giving a presentation about my research project at the EGU General Assembly in Vienna.

I would also like to thank Dr. Mark Dekkers for answering any palaeomagnetism-related questions I had and for commenting on the first draft of this thesis, and Tom Mullender for helping me when I had questions about the lab equipment.

I am grateful to Dr. Andy Biggin and Dr. Mimi Hill from the University of Liverpool for letting me make use of the microwave system and their help in operating it and interpreting the resulting data.

And last but not least I would like to thank my family and friends for their support during my master's project.

REFERENCES

Books

Tauxe, Lisa, *Essentials of paleomagnetism* (Berkeley/Los Angeles/London 2010)

Papers

Aitken, M. *et al*. (1988) Determination of the intensity of the Earth's magnetic field during archeological times: reliability of the Thellier technique, *Rev. Geophys.* **26**, 3-12.

Biggin, Andrew John (2010) Are systematic differences between thermal and microwave Thellier-type palaeointensity estimates a consequence of multidomain bias in the thermal results?, *Physics of the Earth and Planetary Interiors* **180**, 16–40.

Biggin, Andrew J. and D. Neil Thomas (2003) The application of acceptance criteria to results of Thellier palaeointensity experiments performed on samples with pseudo-single-domain-like characteristics, *Physics of the Earth and Planetary Interiors* **138**, 279–287.

Böhnel, Harald N. *et al*. (2009) Comparison between the microwave and multispecimen parallel difference pTRM paleointensity methods, *Geophys. J. Int.* **177**, 383–394.

Carracedo *et al*. (2001) Geology and volcanology of La Palma and El Hierro, Western Canaries, *Estudios Geol.* **57**, 175-273.

Coe, R.S. (1967) The determination of paleo-intensities of the Earth's magnetic field with emphasis on mechanisms which could cause non-ideal behavior in Thellier's method, *J. Geomag. Geoelectr.* **19**, 157-178.

Coe, Robert S., Sherman Grommé and Edward A. Mankinen (1978) Geomagnetic paleointensities form radiocarbon-dated lava flows on Hawaii and the question of the Pacific Nondipole Low, *Journal of Geophysical Research* vol 83, no B4, 1740-1756.

Day, R., M. Fuller and V.A. Schmidt (1977) Hysteresis properties of titanomagnetites: grain-site and compositional dependence, *Physics of the Earth and Planetary Interiors,* **13**, 260-267.

Dekkers, Mark J. and Harald N. Böhnel (2006) Reliable absolute palaeointensities independent of magnetic domain state, *Earth and Planetary Science Letters* **248**, 508–517.

Dunlop, David J. (1979) On the use of Zijderveld vector diagrams in multicomponent paleomagnetic studies, *Physics of the Earth and Planetary Interiors* **20**, 12-24.

Fabian, Karl and Roman Leonhardt (2010) Multiple-specimen absolute paleointensity determination: An optimal protocol including pTRM normalization, domain-state correction, and alteration test, *Earth and Planetary Science Letters* **297**, 84**–**94.

Grommé, C., T.L. Wright and D.L. Peck (1969) Magnetic properties and oxidation of iron-titanium oxide minerals in Alae and Makaopuhi lava lakes, Hawaii, *Journal of Geophysical Research*, vol. 74, no. 22, 5277-5293.

Hill, Mimi J. and John Shaw (2007) The use of the 'Kono perpendicular applied field method' in microwave palaeointensity experiments, *Earth Planets Space* **59**, 711–716.

Hill, Mimi J., John Shaw and Emilio Herrero-Bervera (2005) Palaeointensity record through the Lower Mammoth reversal from the Waianae volcano, Hawaii, *Earth and Planetary Science Letters* **230**, 255–272.

Hunt, Chris (1994) Kudos for the Kappabridge, *The IRM Quarterly*, vol. 4, no. 2, 1.

Keulemans (2006) De dag dat de wereld verging: Megatsunami La Palma loopt vertraging op, *[in]ONDERZOEK* **2006-3**, 16-21.

Klügel, A. *et al*. (1999) Chronology and volcanology of the 1949 multi-vent rift-zone eruption on La Palma (Canary Islands), *Journal of Volcanology and Geothermal Research* **94**, 267–282.

Mader, Charles L. (2001) Modeling the La Palma landslide tsunami, *Science of Tsunami Hazards* **19**, 150-170.

Michalk, Daniel M. *et al*. (2008) Evaluation of the multispecimen parallel differential pTRM method: a test on historical lavas from Iceland and Mexico, *Geophys. J. Int.* **173**, 409–420.

Michalk, Daniel M. *et al*. (2010) Application of the multispecimen palaeointensity method to Pleistocene lava flows from the Trans-Mexican Volcanic Belt, *Physics of the Earth and Planetary Interiors* **179**, 139–156.

Tauxe, L. and H. Staudigel (2004) Strength of the geomagnetic field in the Cretaceous Normal Superchron: new data from submarine basaltic glass of the Troodos Ophiolite, *Geochem. Geophys. Geosyst.*, vol. 5, no. 2, Q02H06, doi:10.1029/2003GC000635.

Thellier, E. and O. Thellier (1959) Sur l'intensité du champ magnétique terrestre dans le passé historique et géologique, *Ann. Geophys.* **15**, 285-378.

Valet, Jean-Pierre and Vicente Soler (1999) Magnetic anomalies of lava fields in the Canary islands. Possible consequences for paleomagnetic records, *Physics of the Earth and Planetary Interiors* **115**, 109–118.

Walton, D. *et al*. (1993) Microwave magnetisation, *Geophysical Research Letters*, vol. 20, no. 2, 109-111.

Yu, Yongjae, Lisa Tauxe and Agnès Genevey (2004) Toward an optimal geomagnetic field intensity determination technique, *Geochemistry, Geophysics, Geosystems*, vol. 5, no. 2, Q02H07, doi:10.1029/2003GC000630.

APPENDICES

A.1 Curie diagrams and NRM decay curves

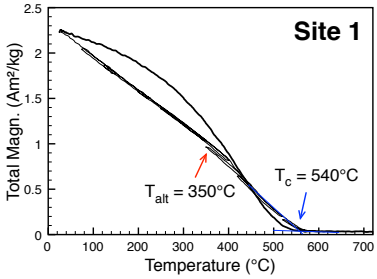

Fig. A1.1a Curie diagram for site 1 (1949). T_c = 540°C, T_{alt} = 350°C. Broad spectrum.

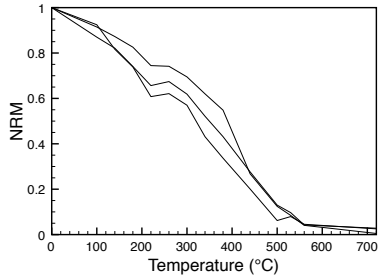

Fig. A1.1b Thermal NRM decay curves for site 1 (1949).

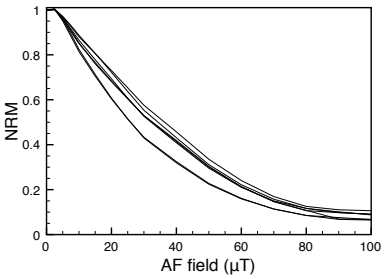

Fig. A1.1c AF NRM decay curves for site 1 (1949).

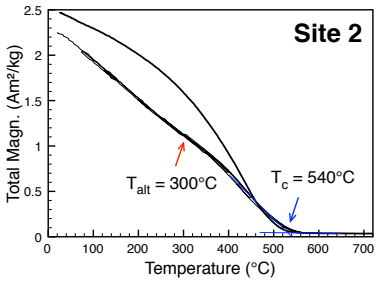

Fig. A1.2a Curie diagram for site 2 (1585). T_c = 540°C; T_{alt} = 300°C (difficult to discern). Broad spectrum.

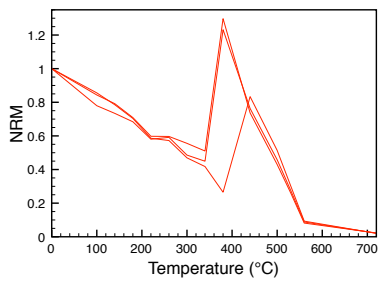

Fig. A1.2b Thermal NRM decay curves for site 2 (1585). All three samples had errors in the range 5-10, which makes the results unreliable.

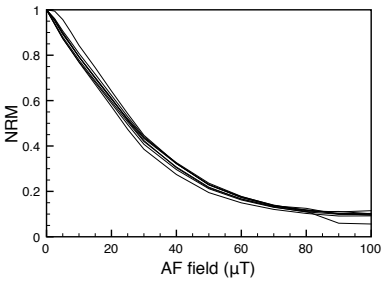

Fig. A1.2c AF NRM decay curves for site 2 (1585).

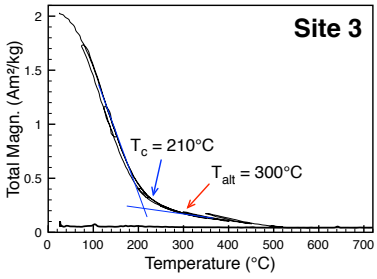

Fig. A1.3a Curie diagram for site 3 (1712). T_c = 210°C, T_{alt} = 300°C.

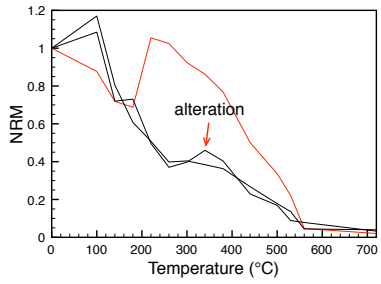

Fig. A1.3b Thermal NRM decay curves for site 3 (1712). The red curve is unreliable because the magnetometer went out of range.

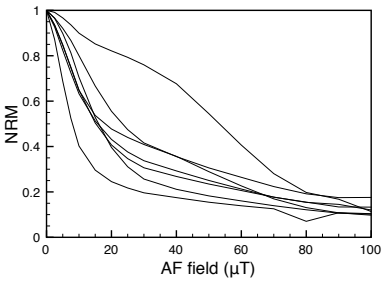

Fig. A1.3c AF NRM decay curves for site 3 (1712). Site 3 shows quite a lot of within-site variation.

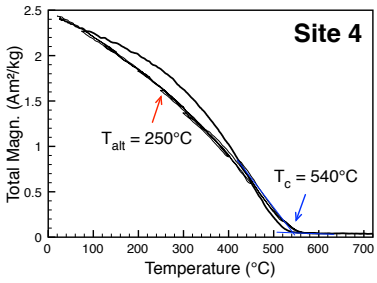

Fig. A1.4a Curie diagram for site 4 (1971, west). T_c = 540°C, T_{alt} = 250°C (difficult to discern).

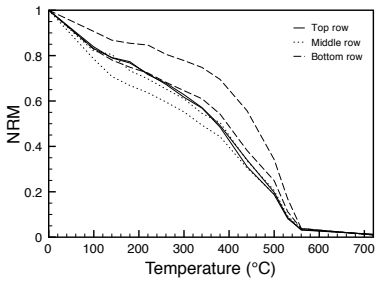

Fig. A1.4b Thermal NRM decay curves for site 4 (1971, west).

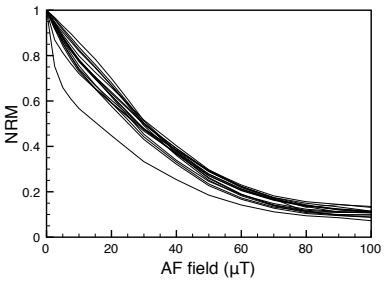

Fig. A1.4c AF NRM decay curves for site 4 (1971, west).

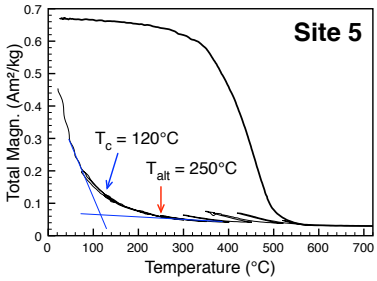

Fig. A1.5a Curie diagram for site 5 (1677). T_c = 120°C, T_{alt} = 250°C.

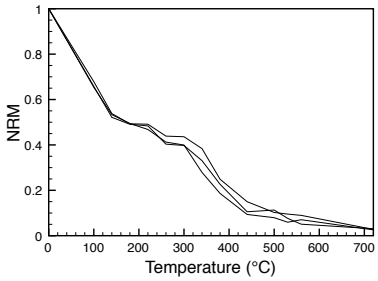

Fig. A1.5b Thermal NRM decay curves for site 5 (1677).

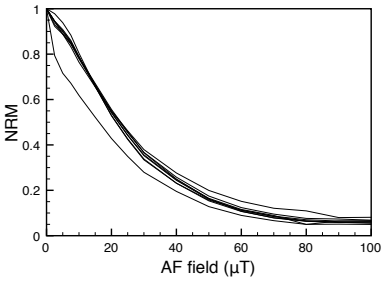

Fig. A1.5c AF NRM decay curves for site 5 (1677).

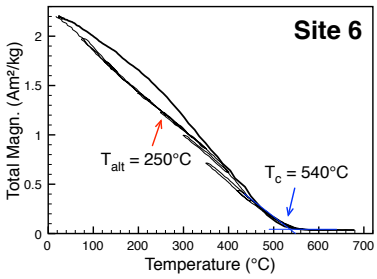

Fig. A1.6a Curie diagram for site 6 (1646). T_c = 540°C, T_{alt} = 300°C. Broad spectrum.

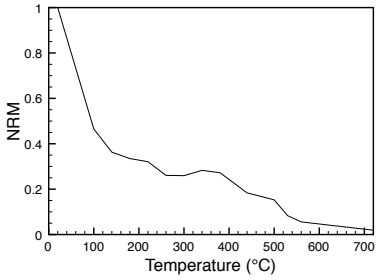

Fig. A1.6b Thermal NRM decay curves for site 6 (1646). The other two samples went out of range. Note the difference between the Curie diagram and the NRM decay curves.

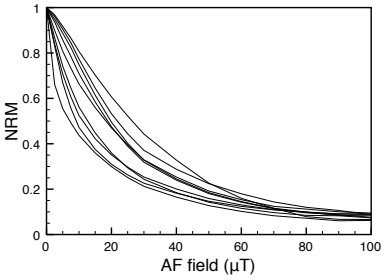

Fig. A1.6c AF NRM decay curves for site 6 (1646).

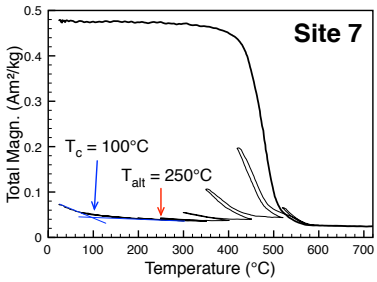

Fig. A1.7a Curie diagram for site 7 (1949, sea). T_c = 100°C, T_{alt} = 250°C. Site 7 shows a lot of alteration.

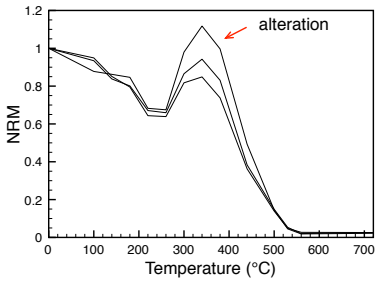

Fig. A1.7b Thermal NRM decay curves for site 7 (1949, sea). The strong alteration visible in the Curie diagram is also visible in these NRM decay curves.

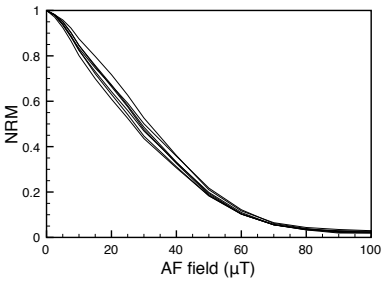

Fig. A1.7c AF NRM decay curves for site 7 (1949, sea).

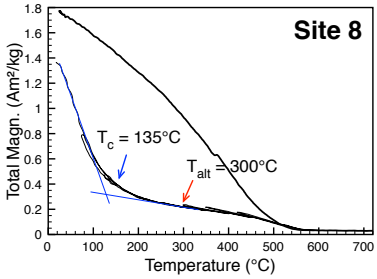

Fig. A1.8a Curie diagram for site 8 (1971, east). T_c = 135°C, T_{alt} = 300°C.

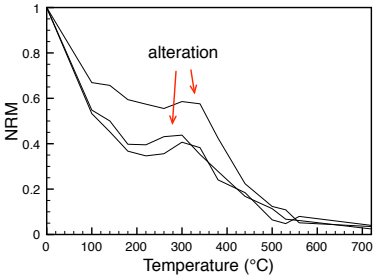

Fig. A1.8b Thermal NRM decay curves for site 8 (1971, east). There is some within-site variation, although the basic shape of the curves is very similar.

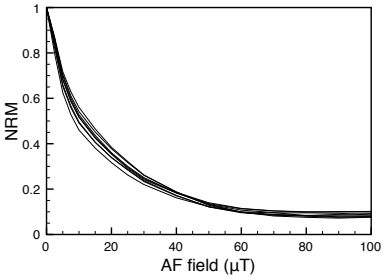

Fig. A1.8c AF NRM decay curves for site 8 (1971, east).

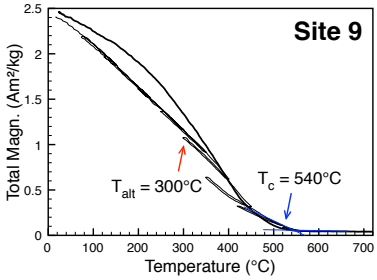

Fig. A1.9a Curie diagram for site 9 (1971, crater). T_c = 540°C, T_{alt} = 300°C. At temperatures > 350°C, site 9 shows quite strong alteration.

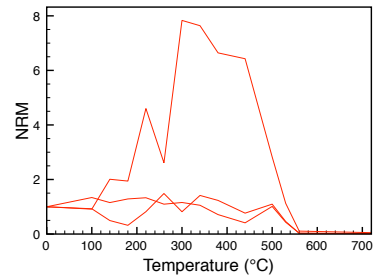

Fig. A1.9b Thermal NRM decay curves for site 9 (1971, crater). All three samples went out of range.

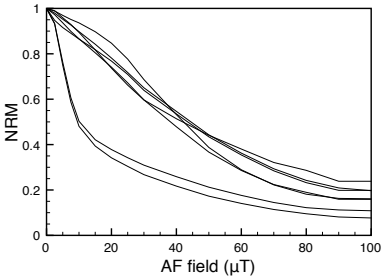

Fig. A1.9c AF NRM decay curves for site 9 (1971, crater). Quite a lot of within-site variation.

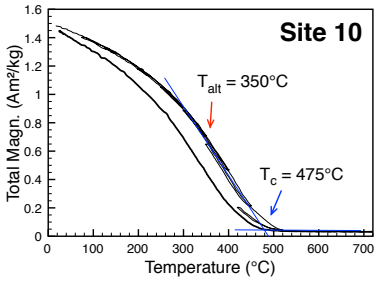

Fig. A1.10a Curie diagram for site 10 (1.09 ± 0.05 ka). T_c = 475°C, T_{alt} = 350°C.

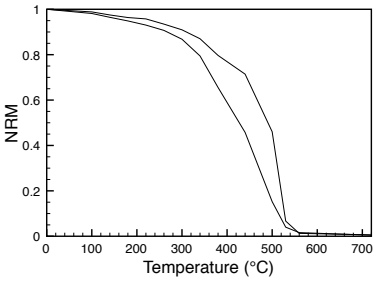

Fig. A1.10b Thermal NRM decay curves for site 10 (1.09 ± 0.05 ka). The curve is quite similar to the Curie diagram. The third sample went out of range.

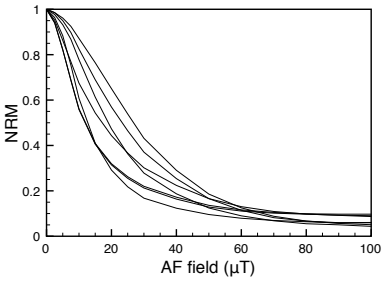

Fig. A1.10c AF NRM decay curves for site 10 (1.09 ± 0.05 ka). Quite a lot of within-site variation.

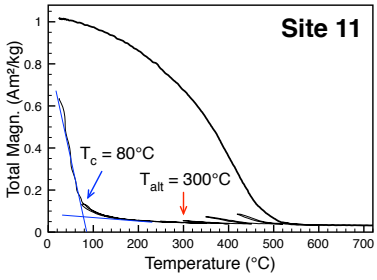

Fig. A1.11a Curie diagram for site 11 (1949, crater). T_c = 80°C, T_{alt} = 300°C.

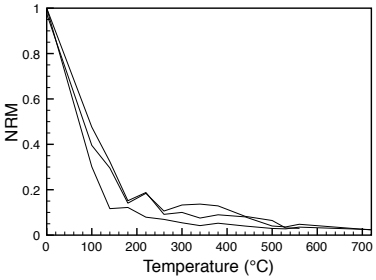

Fig. A1.11b Thermal NRM decay curves for site 11 (1949, crater).

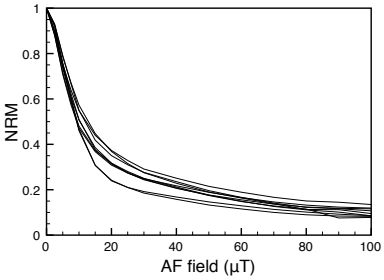

Fig. A1.11c AF NRM decay curves for site 11 (1949, crater).

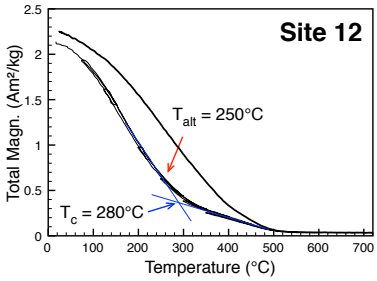

Fig. A1.12a Curie diagram for site 12 (1470-92). T_c = 280°C, T_{alt} = 300°C or possibly 250°C (difficult to discern).

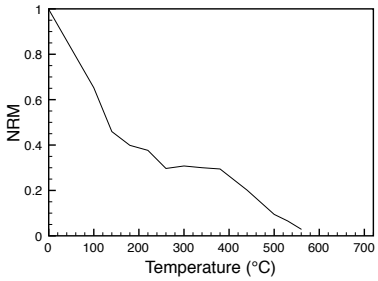

Fig. A1.12b Thermal NRM decay curves for site 12 (1470-92). The other two samples went out of range.

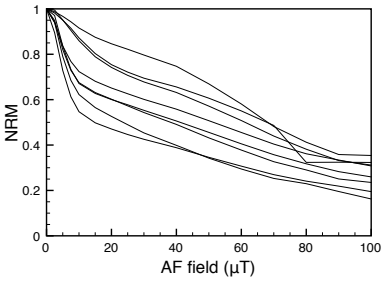

Fig. A1.12c AF NRM decay curves for site 12 (1470-92). Quite a lot of within-site variation.

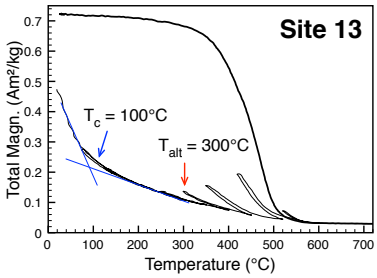

Fig. A1.13a Curie diagram for site 13 (1949, east). Primary T_c = 100°C, T_{alt} = 300°C. Site 13 shows quite strong alteration.

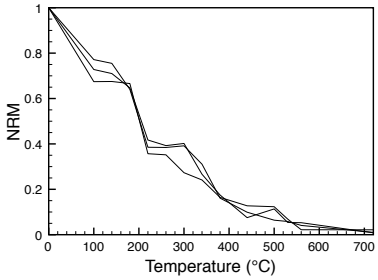

Fig. A1.13b Thermal NRM decay curves for site 13 (1949, east).

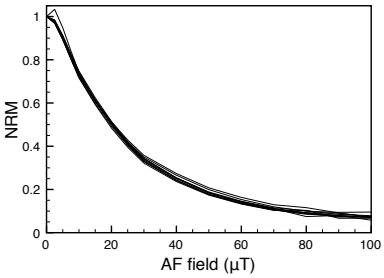

Fig. A1.13c AF NRM decay curves for site 13 (1949, east).

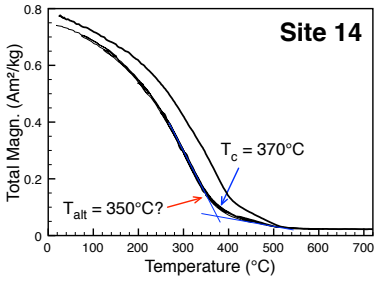

Fig. A1.14a Curie diagram for site 14 (3.2 ± 0.01 ka). T_c = 370°C, T_{alt} = 350°C or possibly higher (very difficult to discern).

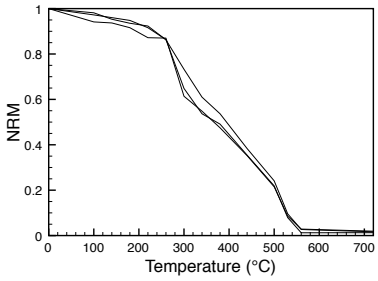

Fig. A1.14b Thermal NRM decay curves for site 14 (3.2 ± 0.01 ka).

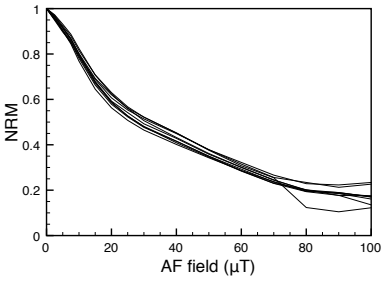

Fig. A1.14c AF NRM decay curves for site 14 (3.2 ± 0.01 ka).

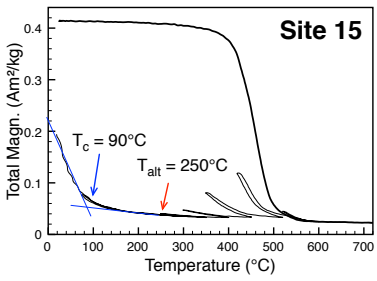

Fig. A1.15a Curie diagram for site 15 (1949). T_c = 90°C, T_{alt} = 250°C. Site 15 shows quite strong alteration and goes out of range on the return curve.

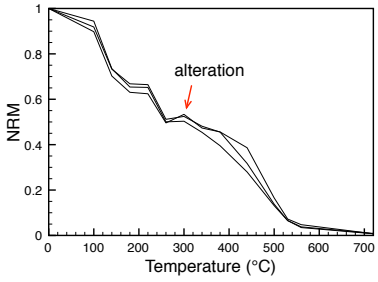

Fig. A1.15b Thermal NRM decay curves for site 15 (1949). Note the difference between its Curie diagram and its thermal NRM decay curve.

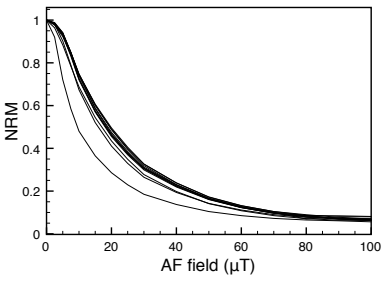

Fig. A1.15c AF NRM decay curves for site 15 (1949).

A2 Susceptibility-versus-temperature diagrams

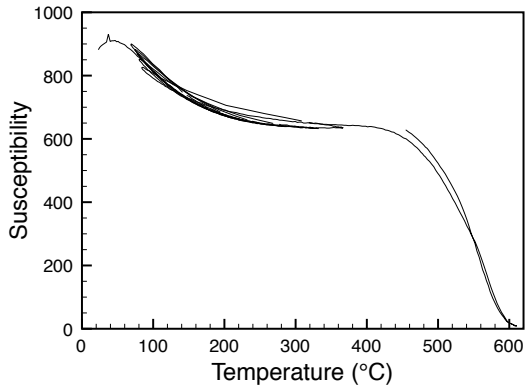

Fig. A2.1 Susceptibility-versus-temperature diagram for site 1 (1949), showing an alteration temperature of ~500°C. The curve is incomplete because the Kappabridge got stuck.

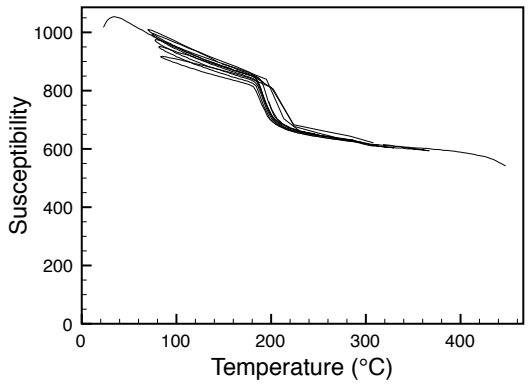

Fig. A2.2 Susceptibility-versus-temperature diagram for site 2 (1585). The curve is incomplete because the Kappabridge got stuck.

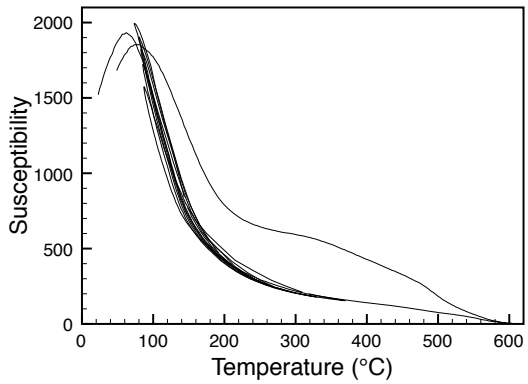

Fig. A2.3 Susceptibility-versus-temperature diagram for site 3 (1712), showing a Curie temperature of ~120°C.

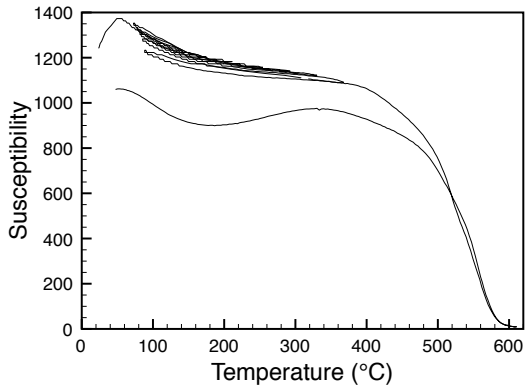

Fig. A2.4 Susceptibility-versus-temperature diagram for site 4 (1971, west), showing a Curie temperature of ~ 500°C.

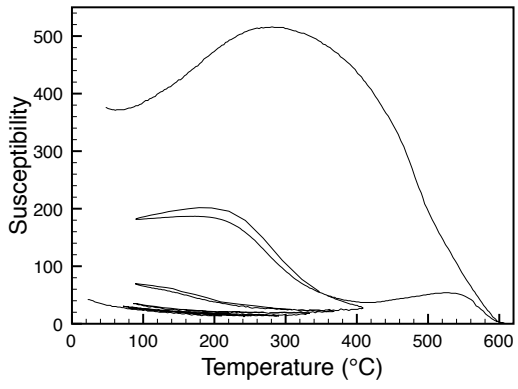

Fig. A2.5 Susceptibility-versus-temperature diagram for site 7 (1949, sea). The plot shows strong alteration when cycling back from 320°C.

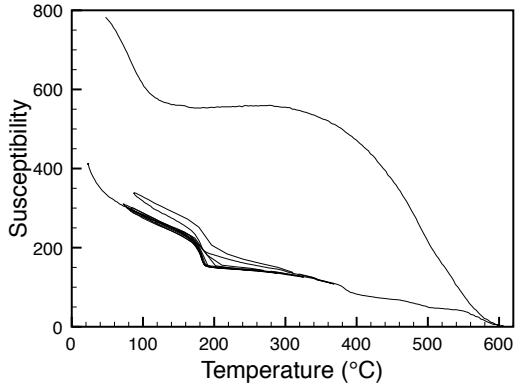

Fig. A2.6 Susceptibility-versus-temperature diagram for site 13 (1949, east). The plot shows alteration when cycling back from 360°C.

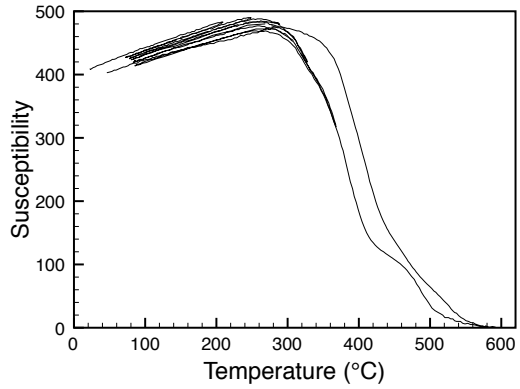

Fig. A2.7 Susceptibility-versus-temperature diagram for site 14 (3.2 ± 0.01 ka), showing a Curie temperature of ~350°C. Alteration is only visible after cycling to 600°C.

A.3 Thellier-Thellier results

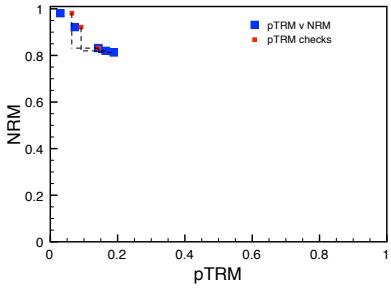

Fig. A3.1a Thellier-Thellier Arai plot for site 1 (1949). The plot shows sagging, making it impossible to extract a PI.

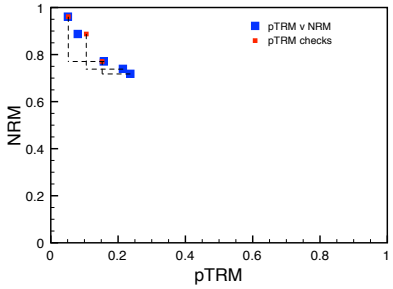

Fig. A3.1b Thellier-Thellier Arai plot for site 1 (1949). The plot shows sagging, making it impossible to extract a PI.

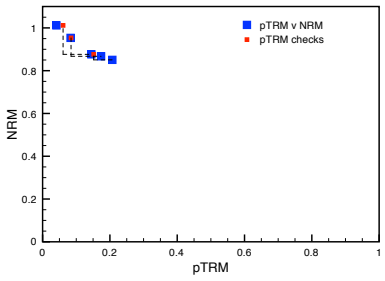

Fig. A3.1c Thellier-Thellier Arai plot for site 1 (1949). The plot shows sagging, making it impossible to extract a PI.

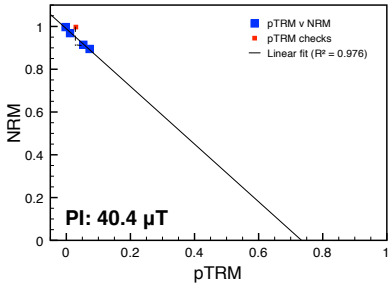

Fig. A3.2a Thellier-Thellier Arai plot for site 2 (1585). PI unreliable because of a failed pTRM check.

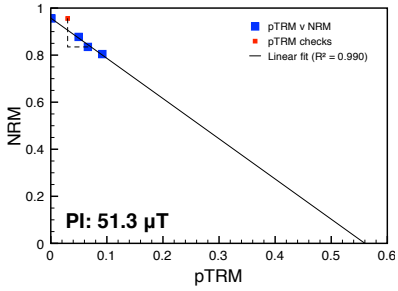

Fig. A3.2b Thellier-Thellier Arai plot for site 2 (1585). PI unreliable because of a failed pTRM check.

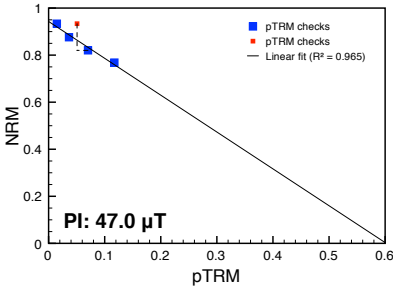

Fig. A3.2c Thellier-Thellier Arai plot for site 2 (1585). PI unreliable because of a failed pTRM check.

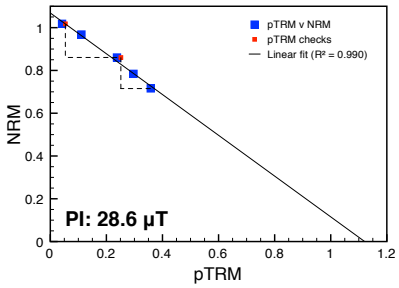

Fig. A3.3a Thellier-Thellier Arai plot for site 3 (1712). Technically good plot, although the specimen loses less than 30% of its NRM.

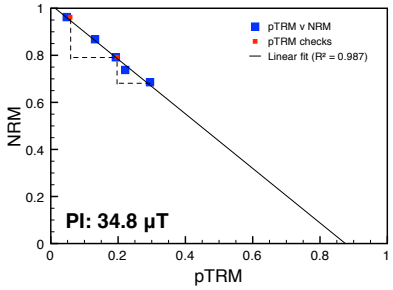

Fig. A3.3b Thellier-Thellier Arai plot for site 3 (1712). Technically good plot, although the specimen loses less than 30% of its NRM.

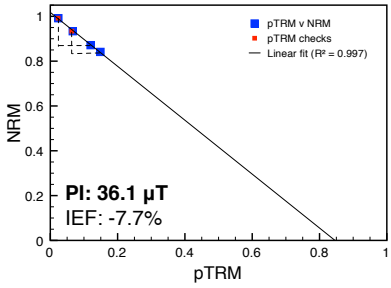

Fig. A3.4a Thellier-Thellier Arai plot for site 4 (1971, west), top row. Technically good plot, except for the small loss of NRM.

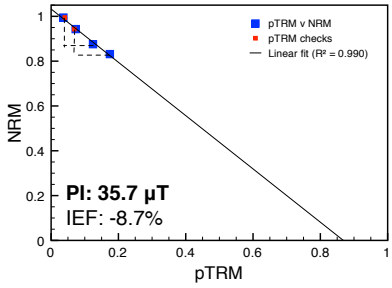

Fig. A3.4b Thellier-Thellier Arai plot for site 4 (1971, west), top row. Technically good plot, except for the small loss of NRM.

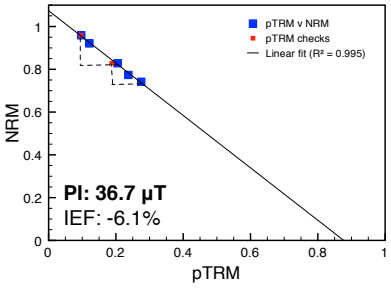

Fig. A3.4c Thellier-Thellier Arai plot for site 4 (1971, west), middle row. Technically good plot, except for the small loss of NRM.

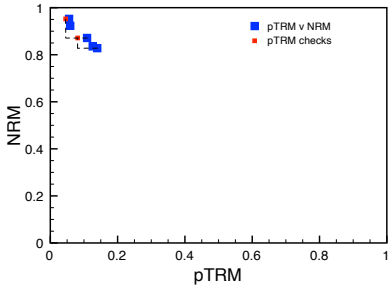

Fig. A3.4d Thellier-Thellier Arai plot for site 4 (1971, west). The Arai plot does not show a straight line and the second pTRM check failed.

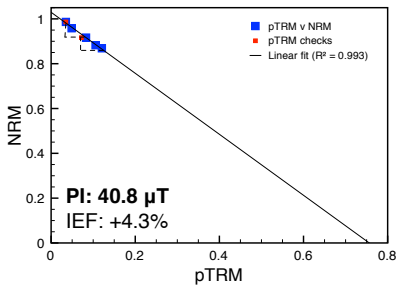

Fig. A3.4e Thellier-Thellier Arai plot for site 4 (1971, west). Technically good plot, except for the small loss of NRM.

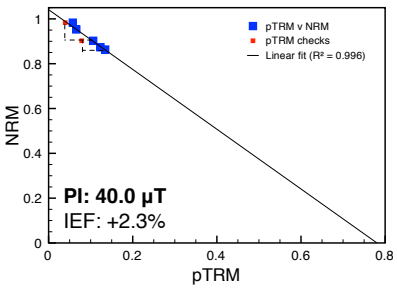

Fig. A3.4f Thellier-Thellier Arai plot for site 4 (1971, west). The pTRM checks are not that good, making the obtained PI unreliable.

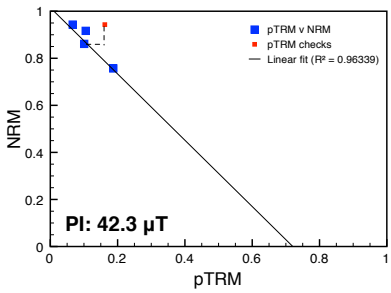

Fig. A3.5a Thellier-Thellier Arai plot for site 5 (1646). Failed pTRM check and data points not on a straight line.

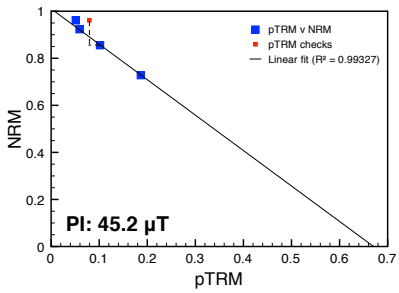

Fig. A3.5b Thellier-Thellier Arai plot for site 5 (1646). Failed pTRM check and data points not on a straight line.

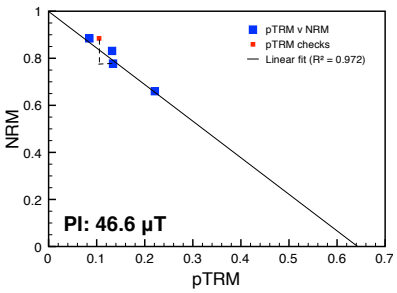

Fig. A3.5c Thellier-Thellier Arai plot for site 5 (1646). Failed pTRM check and data points not on a straight line.

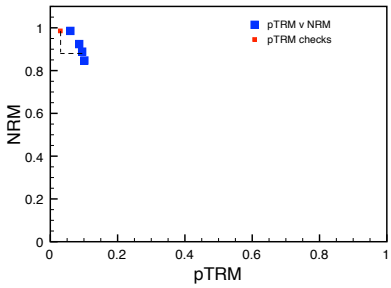

Fig. A3.6a Thellier-Thellier Arai plot for site 6 (1677). This plot was calculated using vector subtraction, as scalar subtraction yielded very odd results, most likely indicating that the specimen was not correctly aligned.

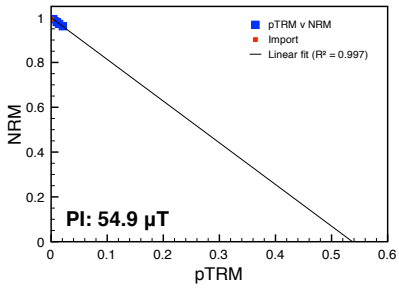

Fig. A3.6b Thellier-Thellier Arai plot for site 6 (1677). Because the specimen loses less than 10% of its NRM, drawing a linear fit through these data points is not really justified.

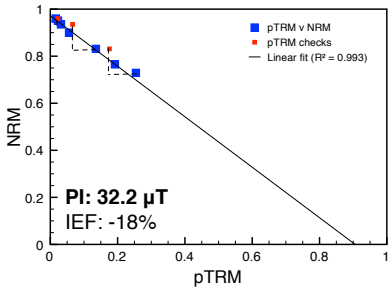

Fig. A3.7a Thellier-Thellier Arai plot for site 7 (1949, sea). PI unreliable because of failed pTRM checks.

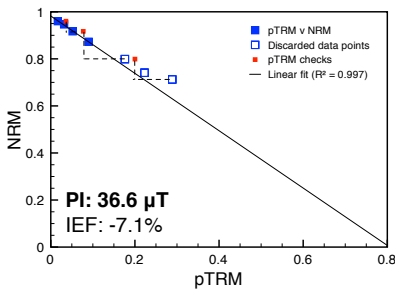

Fig. A3.7b Thellier-Thellier Arai plot for site 7 (1949, sea). The last three data points were discarded because the last two pTRM checks failed, indicating alteration between steps 3 and 5.

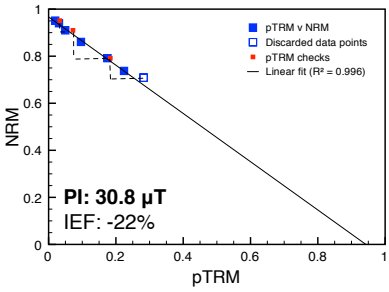

Fig. A3.7c Thellier-Thellier Arai plot for site 7 (1949, sea).

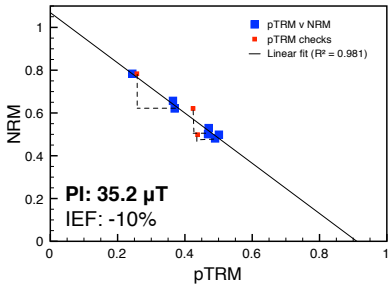

Fig. A3.8a Thellier-Thellier Arai plot for site 8 (1971, east). PI unreliable because the data points are not on a straight line and the last two pTRM checks failed.

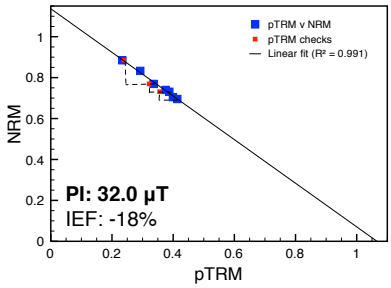

Fig. A3.8b Thellier-Thellier Arai plot for site 8 (1971, east).

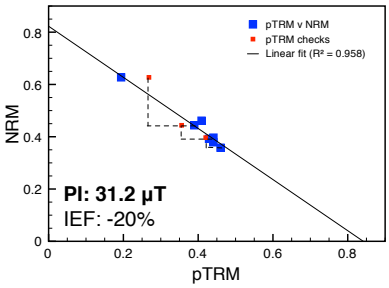

Fig. A3.8c Thellier-Thellier Arai plot for site 8 (1971, east). PI unreliable because the data points are not on a straight line and the last two pTRM checks failed.

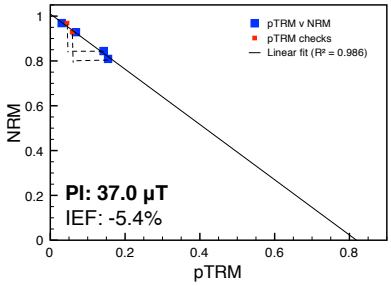

Fig. A3.9a Thellier-Thellier Arai plot for site 9 (1971, crater). Technically good Arai plot, although the very small loss of NRM makes the result less reliable.

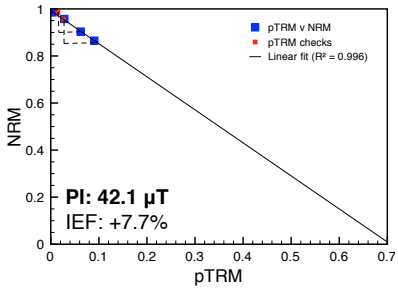

Fig. A3.9a Thellier-Thellier Arai plot for site 9 (1971, crater). Technically good Arai plot, although the very small loss of NRM makes the result less reliable.

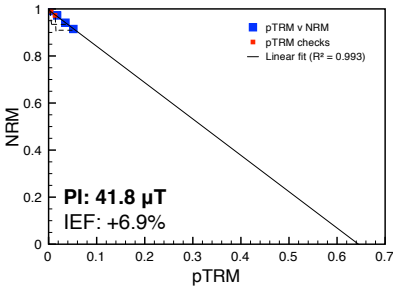

Fig. A3.9a Thellier-Thellier Arai plot for site 9 (1971, crater). Technically good Arai plot, although the very small loss of NRM makes the result less reliable.

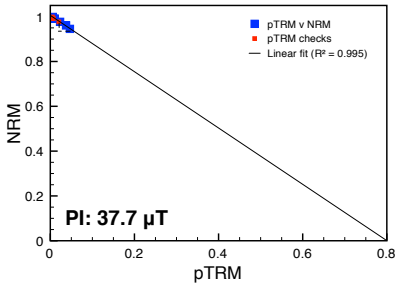

Fig. A3.10a Thellier-Thellier Arai plot for site 10 (1.09 ± 0.05 ka). Technically good Arai plot, although the very small loss of NRM makes the result less reliable.

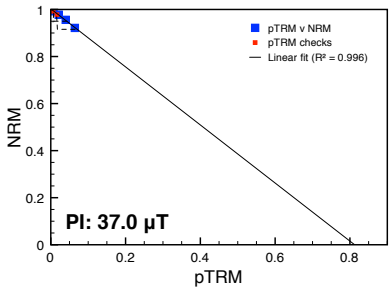

Fig. A3.10b Thellier-Thellier Arai plot for site 10 (1.09 ± 0.05 ka). Technically good Arai plot, although the very small loss of NRM makes the result less reliable.

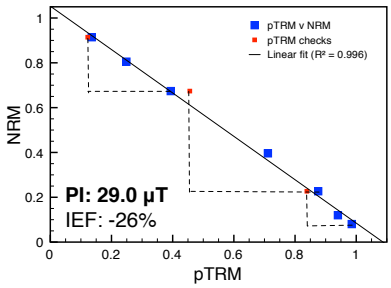

Fig. A3.11a Thellier-Thellier Arai plot for site 11 (1949, crater). Technically very good Arai plot.

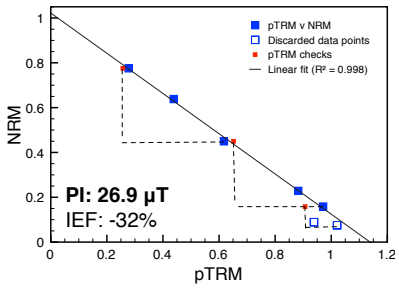

Fig. A3.11b Thellier-Thellier Arai plot for site 11 (1949, crater). Technically very good Arai plot.

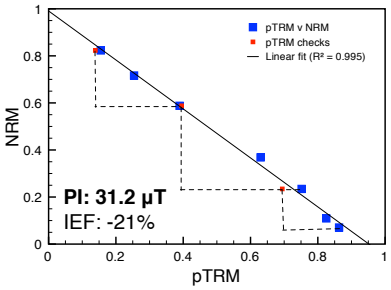

Fig. A3.11c Thellier-Thellier Arai plot for site 11 (1949, crater). Technically very good Arai plot.

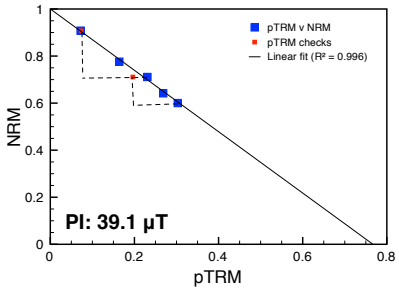

Fig. A3.12 Thellier-Thellier Arai plot for site 12. The second pTRM check may be indicative of alteration between steps 3 and 5.

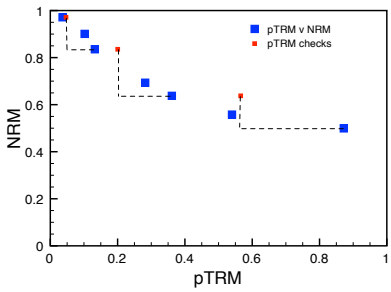

Fig. A3.13a Thellier-Thellier Arai plot for site 13. The Arai plot shows strong sagging and failed pTRM checks.

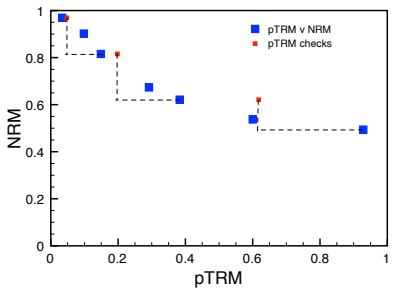

Fig. A3.13b Thellier-Thellier Arai plot for site 13. The Arai plot shows strong sagging and failed pTRM checks.

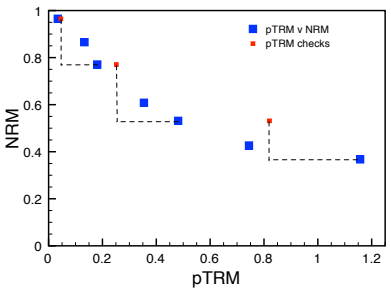

Fig. A3.13c Thellier-Thellier Arai plot for site 13. The Arai plot shows strong sagging and failed pTRM checks.

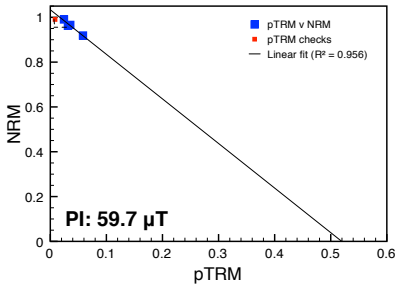

Fig. A3.14a Thellier-Thellier Arai plot for site 14 (3.2 ± 0.01 ka). Technically good Arai plot, although the very small loss of NRM makes the result less reliable.

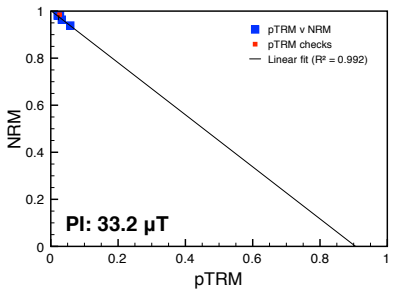

Fig. A3.14b Thellier-Thellier Arai plot for site 14 (3.2 ± 0.01 ka). Technically good Arai plot, although the very small loss of NRM makes the result less reliable.

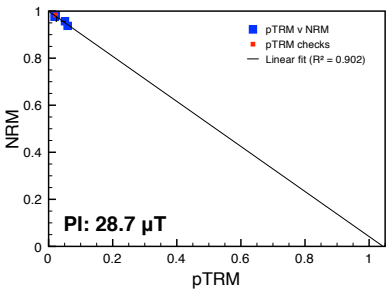

Fig. A3.14c Thellier-Thellier Arai plot for site 14 (3.2 ± 0.01 ka). Technically good Arai plot, although the very small loss of NRM makes the result less reliable.

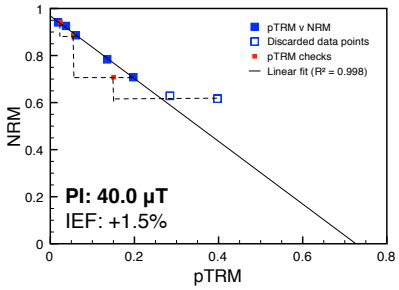

Fig. A3.15a Thellier-Thellier Arai plot for site 15 (1949). The last two data points were discarded based on the third pTRM check, which indicates alteration between steps 5 and 7.

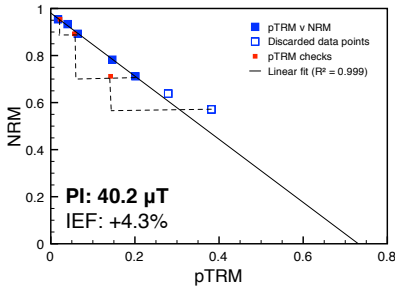

Fig. A3.15b Thellier-Thellier Arai plot for site 15 (1949). The last two data points were discarded based on the third pTRM check, which indicates alteration between steps 5 and 7.

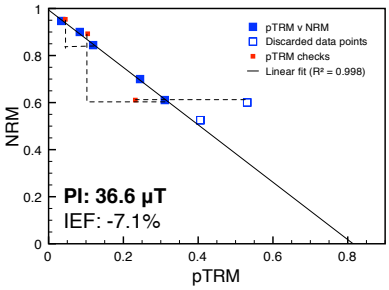

Fig. A3.15c Thellier-Thellier Arai plot for site 15 (1949). The last two data points were discarded based on the third pTRM check, which indicates alteration between steps 5 and 7.

A.4 Microwave results

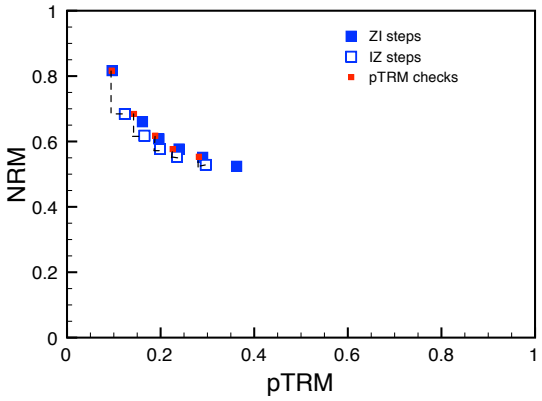

Fig. A4.1 Microwave result for site 1 (1949) using the IZZI antiparallel protocol and H_{lab} = 30 µT. The plot shows strong sagging.

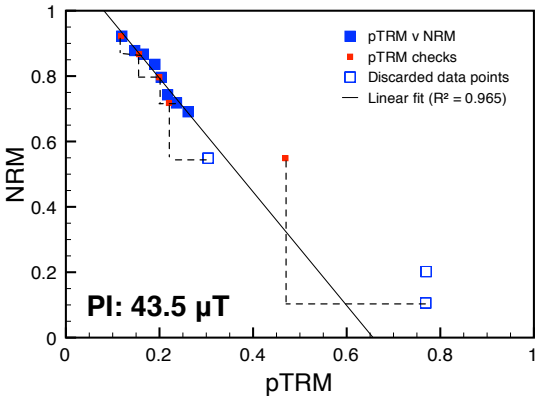

Fig. A4.2 Microwave result for site 2 (1585) using the Aitken parallel protocol and H_{lab} = 25 µT. After the first eight steps, the plot starts showing alteration.

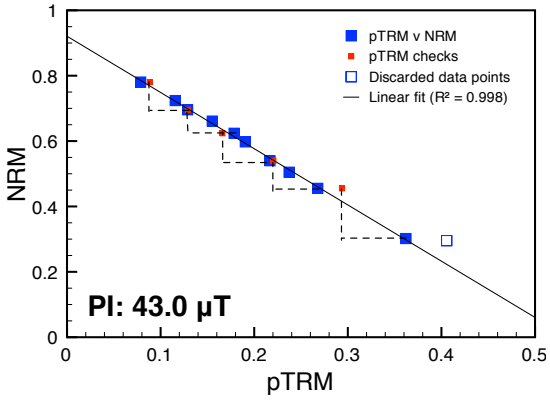

Fig. A4.3 Microwave result for site 3 (1712) using the Aitken parallel protocol and H_{lab} = 25 µT. Straight line and good checks except the last one.

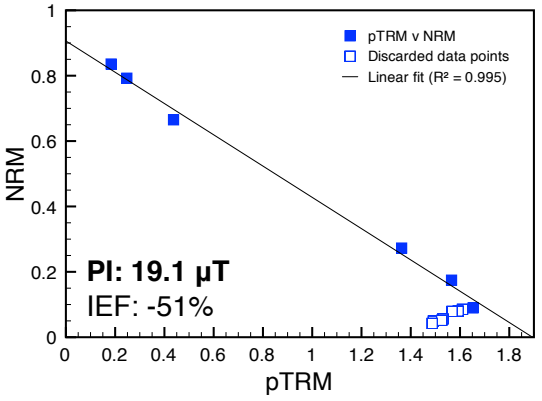

Fig. A4.4 Microwave result for site 4 (1971, west) using the perpendicular protocol and H_{lab} = 40 µT. No pTRM checks.

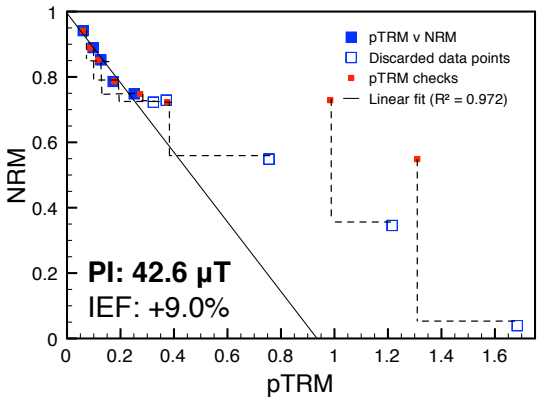

Fig. A4.5 Microwave result for site 4 (1971, west) using the Aitken parallel protocol and H_{lab} = 40 µT. Strong alteration and sagging after the first five steps.

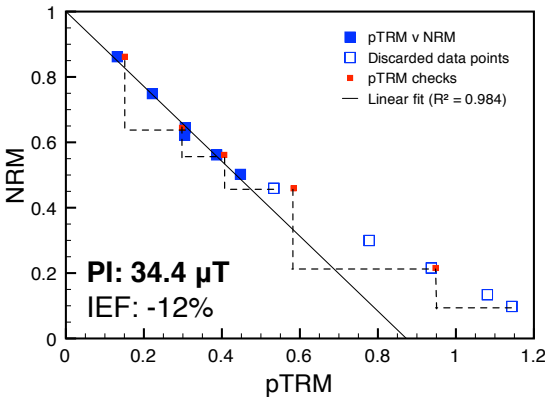

Fig. A4.6 Microwave result for site 4 (1971, west) using the Aitken parallel protocol and H_{lab} = 30 µT, showing alteration and sagging after the first six steps.

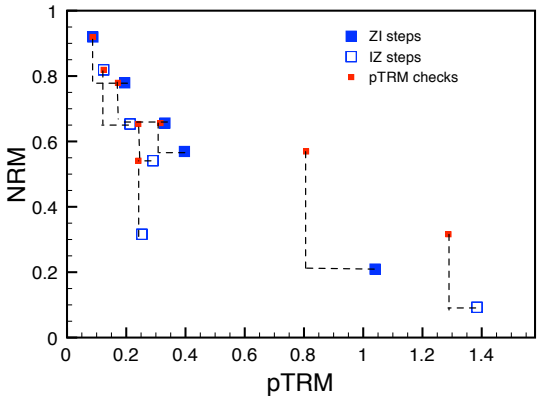

Fig. A4.7 Microwave result for site 4 (1971, west) using the IZZI antiparallel protocol and H_{lab} = 40 μT. Failed checks and sagging.

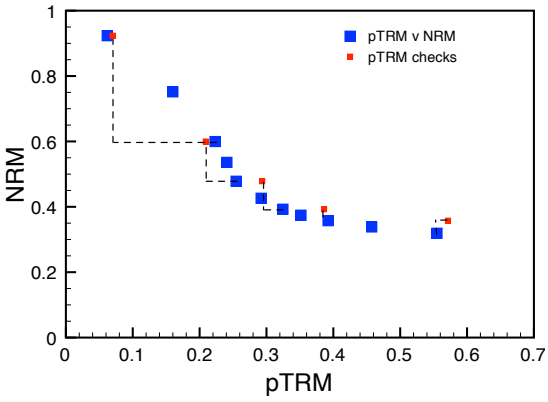

Fig. A4.8 Microwave result for site 5 (1677) using the Aitken parallel protocol and H_{lab} = 25 μT. The plot shows sagging after the third step.

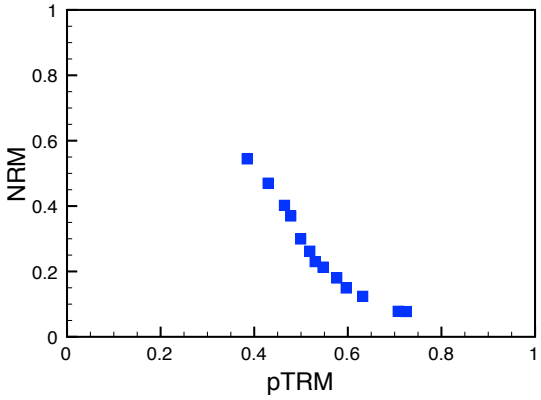

Fig. A4.9 Microwave result for site 7 (1949, sea) using the perpendicular protocol and H_{lab} = 25 μT. The plot shows sagging.

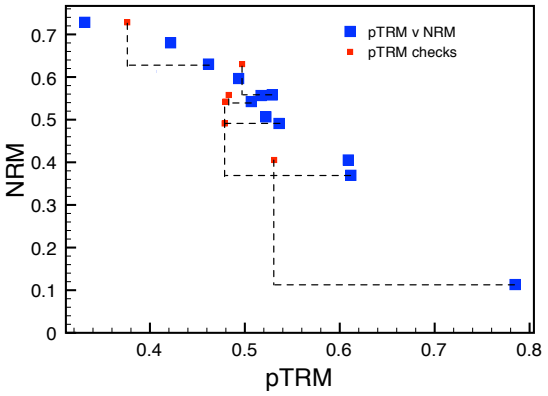

Fig. A4.10 Microwave result for site 8 (1971, east) using the Aitken parallel protocol and H_{lab} = 25 μT. Failed pTRM checks and no straight line.

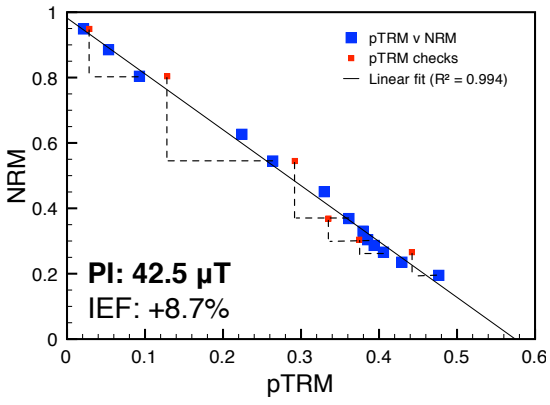

Fig. A4.11 Microwave result for site 9 (1971, crater) using the Aitken parallel protocol and H_{lab} = 25 μT. Straight line, but the checks are not that good.

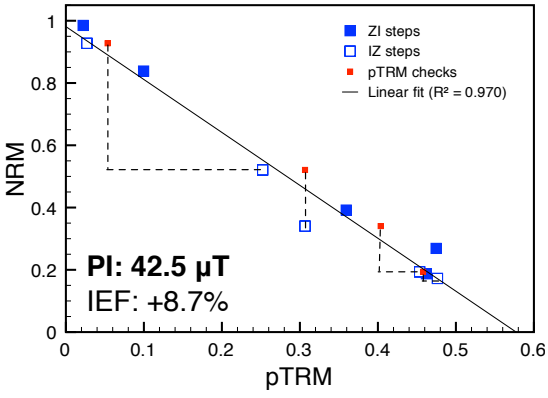

Fig. A4.12 Microwave result for site 9 (1971, crater) using the IZZI antiparallel protocol and H_{lab} = 25 μT. Failed checks, but little zig-zagging indicating MD behaviour.

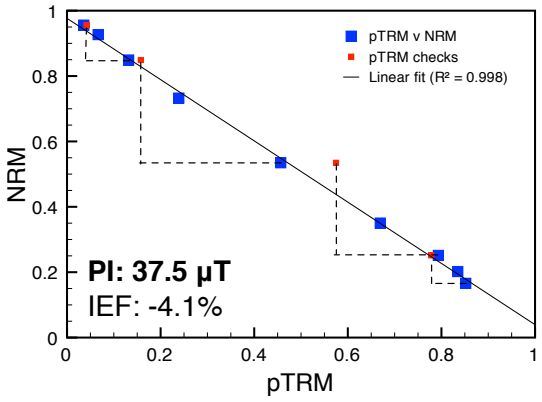

Fig. A4.13 Microwave result for site 9 (1971, crater) using the Aitken parallel protocol and H_{lab} = 40 µT. Straight line and good first two checks.

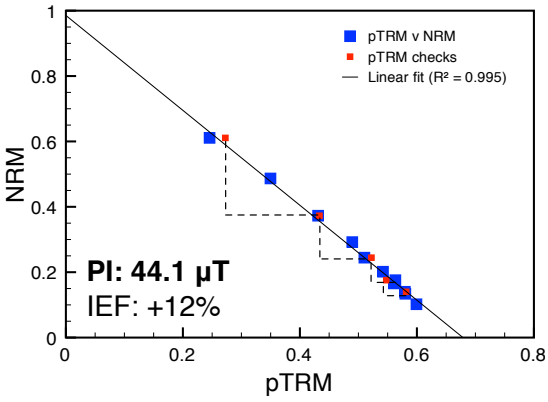

Fig. A4.14 Microwave result for site 11 (1949, crater) using the Aitken parallel protocol and H_{lab} = 25 µT. Straight line and good checks.

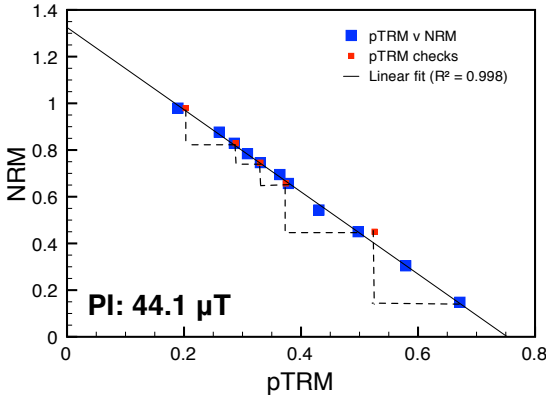

Fig. A4.15 Microwave result for site 12 (1470-92) using the Aitken parallel protocol and H_{lab} = 25 µT. Straight line and good pTRM checks.

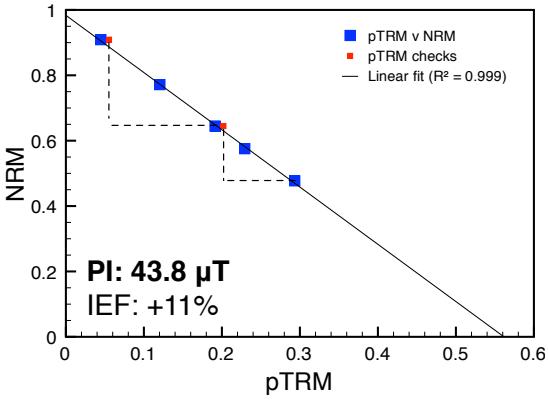

Fig. A4.16 Microwave result for site 13 (1949, east) using the Aitken parallel protocol and H_{lab} = 25 µT. Straight line and good pTRM checks.

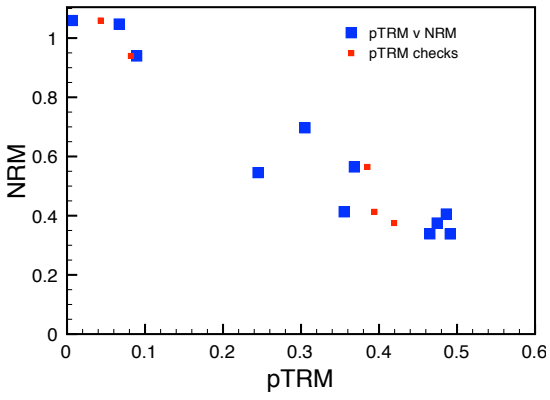

Fig. A4.17 Microwave result for site 14 (3.2 ± 0.01 ka) using the Aitken parallel protocol and H_{lab} = 25 µT. Failed pTRM checks and no straight line.

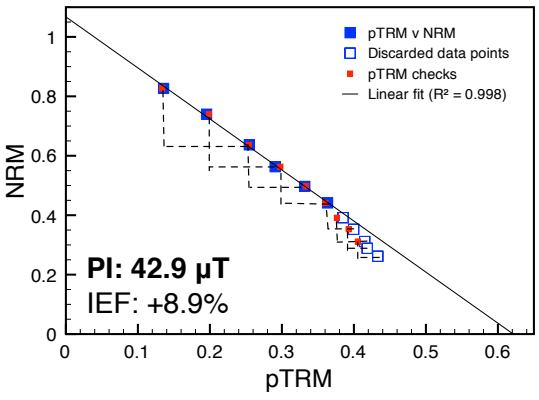

Fig. A4.18 Microwave result for site 15 (1949) using the Aitken parallel protocol and H_{lab} = 25 µT. The first six pTRM checks are extremely good, indicating no alteration in that part of the graph.

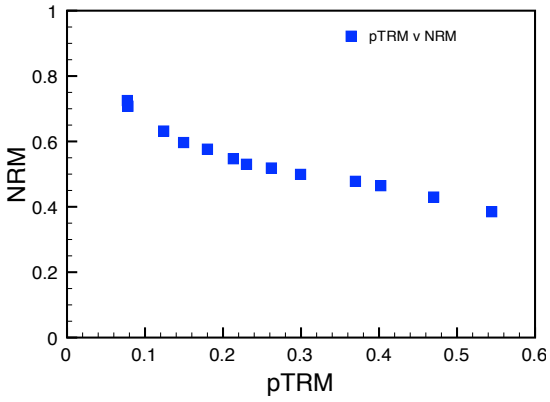

Fig. A4.19 Microwave result for site 15 (1971, east) using the perpendicular protocol and H_{lab} = 25 μT. The plot shows sagging.

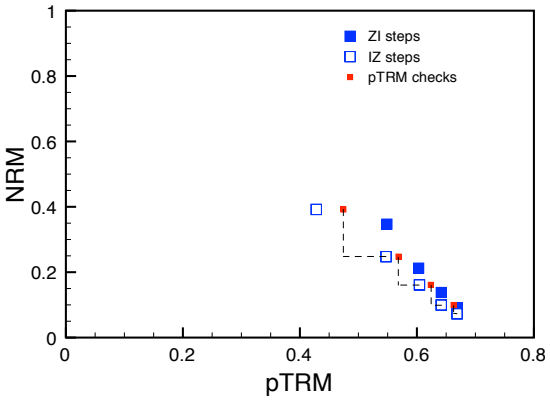

Fig. A4.20 Microwave result for site 8 (1971, east) using the IZZI antiparallel protocol and H_{lab} = 40 μT. Zig-zagging and failed pTRM checks.

A.5 Multispecimen results

Site 1 (1949)

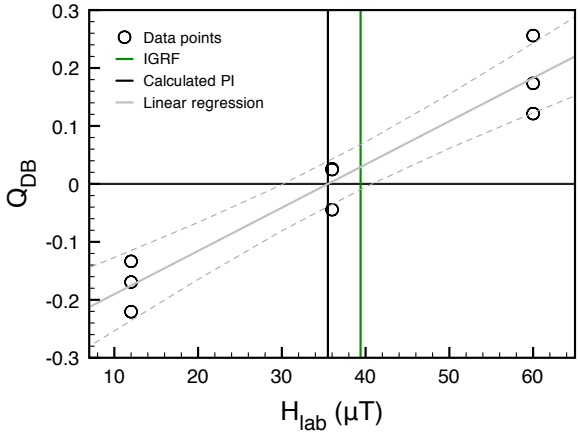

Fig. A5.1a MSP-DB. Small (< 10%) underestimate.

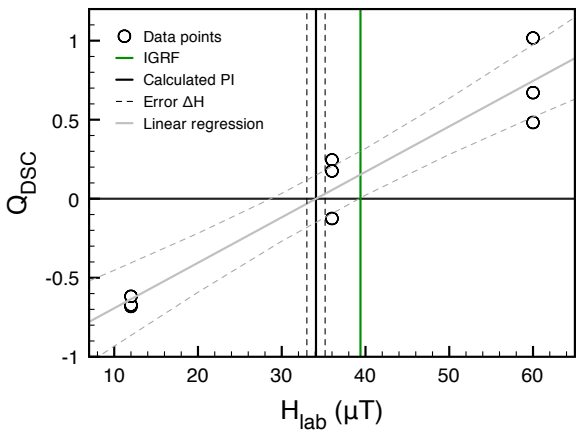

Fig. A5.1b MSP-DSC. The underestimate is lowered further.

H_{lab} (μT)	μ_{DS}	H_{max} (μT)	H_{est} (μT)	ΔH_{est} (μT)	ε_{alt}	Q_{DB}	Q_{FC}	Q_{DSC}	$(\Delta Q_{DS\,c,alt})^2$	$(\Delta Q_{DS\,c,ds})^2$	ΔQ_i	m_2
12	0.029	47.1	37.7	4.6	0.027	-0.134	-0.745	-0.681	0.028	0.001	0.171	+
12	0.040	45.6	36.6	4.4	0.029	-0.169	-0.737	-0.673	0.019	0.001	0.143	+
12	0.032	34.0	31.4	1.5	0.007	-0.221	-0.647	-0.617	0.000	0.000	0.028	+
36	0.046	45.2	41.1	2.2	0.029	-0.044	-0.203	-0.125	0.037	0.002	0.197	+
36	0.072	32.1	28.9	1.7	0.040	0.026	0.122	0.245	0.105	0.005	0.332	+
36	0.086	33.2	30.6	1.5	0.037	0.025	0.083	0.175	0.045	0.003	0.220	+
60	0.039	41.8	40.5	0.8	0.014	0.121	0.434	0.482	0.010	0.001	0.106	+
60	0.083	31.3	29.8	0.9	0.007	0.256	0.918	1.017	0.005	0.003	0.090	+
60	0.095	38.2	35.9	1.3	0.025	0.174	0.571	0.671	0.033	0.003	0.189	+
Ave	**0.058**	**38.7**	**34.7**		**0.024**				**0.031**	**0.002**	**0.164**	
σ	**0.026**	**6.3**	**4.7**		**0.012**				**0.031**	**0.002**	**0.087**	

Site 2 (1585)

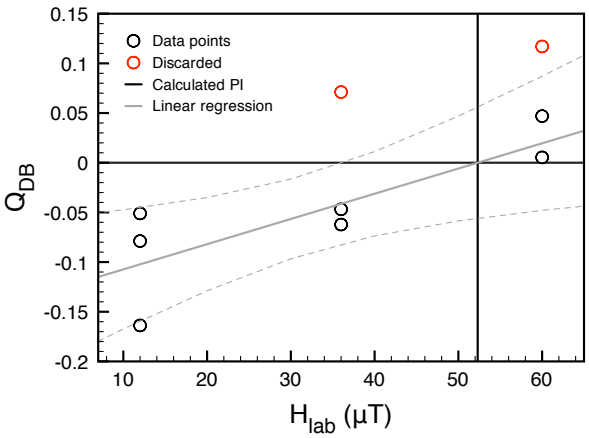

Fig. A5.2a MSP-DB. The plot shows a lot of scatter.

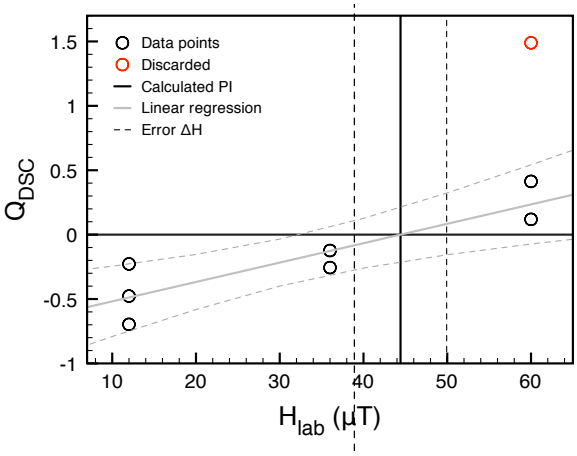

Fig. A5.2b MSP-DSC. Even with the two obvious outliers removed (in red), the plot still shows a large scatter. The discarded data point at 36 μT is not shown because it would distort the plot too much.

H_{lab} (μT)	μ_{DS}	H_{max} (μT)	H_{est} (μT)	ΔH_{est} (μT)	ε_{alt}	Q_{DB}	Q_{FC}	Q_{DSC}	$(\Delta Q_{DS\,c,alt})^2$	$(\Delta Q_{DS\,c,ds})^2$	ΔQ_i	m_2
12	0.057	20.8	15.5	2.4	0.046	-0.051	-0.424	-0.228	0.288	0.013	0.549	+
12	0.028	27.2	23.0	2.2	0.020	-0.079	-0.559	-0.477	0.030	0.002	0.180	+
12	0.038	50.6	39.6	5.3	0.029	-0.164	-0.763	-0.697	0.021	0.001	0.149	+
36	0.360	-375.6	-15.9	13.6	0.032	0.071	-1.096	-3.270	0.774	1.575	1.533	+
36	0.053	59.0	48.4	5.3	0.033	-0.062	-0.389	-0.256	0.078	0.006	0.289	+
36	0.066	49.3	41.1	4.1	0.040	-0.047	-0.269	-0.123	0.113	0.007	0.346	+
60	0.061	47.1	42.5	2.5	0.028	0.047	0.274	0.413	0.094	0.006	0.317	+
60	0.075	27.6	24.1	1.8	0.040	0.117	1.174	1.489	1.104	0.033	1.066	+
60	0.205	59.3	53.6	3.1	0.068	0.005	0.012	0.119	0.063	0.004	0.258	+
Ave	**0.105**	**42.6**	**36.0**		**0.037**				**0.285**	**0.183**	**0.521**	
σ	**0.109**	**15.2**	**13.5**		**0.014**				**0.388**	**0.522**	**0.471**	

Site 3 (1712)

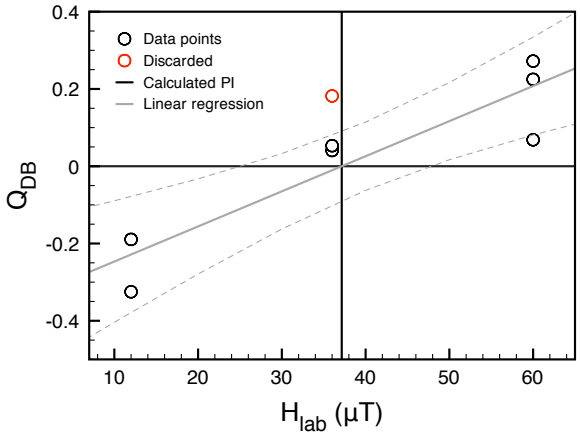

Fig. A5.3a MSP-DB. Large scatter.

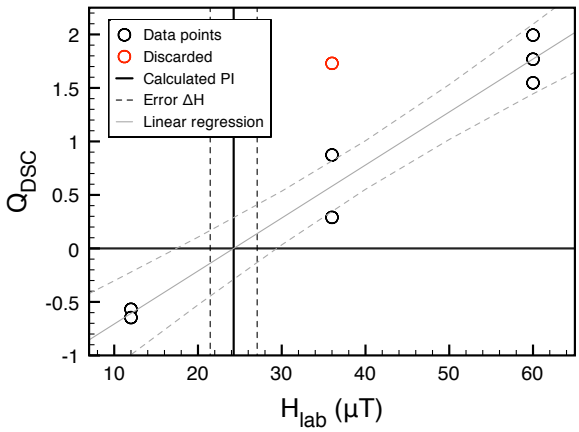

Fig. A5.3b MSP-DSC. The scatter is somewhat reduced compared to the MSP-DB plot.

H_{lab} (μT)	μ_{DS}	H_{max} (μT)	H_{est} (μT)	ΔH_{est} (μT)	ε_{alt}	Q_{DB}	Q_{FC}	Q_{DSC}	$(\Delta Q_{DS\,c,alt})^2$	$(\Delta Q_{DS\,c,ds})^2$	ΔQ_i	m_2
12	0.071	34.2	27.8	3.2	0.049	-0.189	-0.649	-0.569	0.032	0.002	0.185	+
12	0.097	39.6	33.9	2.9	0.069	-0.325	-0.697	-0.646	0.016	0.001	0.132	+
36	0.084	14.7	13.2	0.8	0.037	0.182	1.457	1.730	0.732	0.025	0.870	+
36	0.09	24.7	19.2	2.6	0.047	0.041	0.455	0.874	1.240	0.058	1.140	+
36	0.139	30.9	27.9	1.7	0.051	0.053	0.163	0.290	0.080	0.005	0.292	+
60	0.182	24.6	21.7	1.6	0.051	0.272	1.439	1.769	0.702	0.036	0.859	+
60	0.034	22.9	20.0	1.5	0.022	0.068	1.625	1.994	2.179	0.045	1.492	+
60	0.092	25.6	23.6	1.2	0.037	0.225	1.340	1.548	0.392	0.014	0.637	+
Ave	**0.099**	**27.2**	**23.4**		**0.045**				**0.672**	**0.023**	**0.701**	
σ	**0.045**	**7.6**	**6.4**		**0.014**				**0.743**	**0.022**	**0.483**	

Site 4 (1971, west)

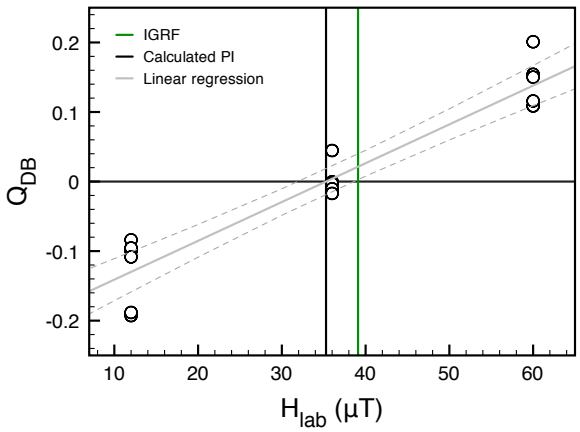

Fig. A5.4a MSP-DB. Small (< 10%) underestimate.

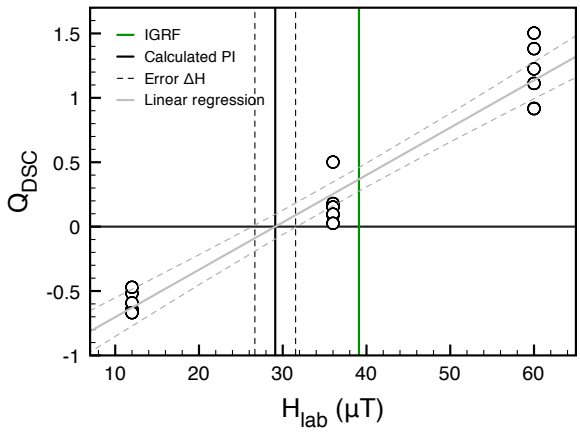

Fig. A5.4b MSP-DSC. The underestimate is further lowered.

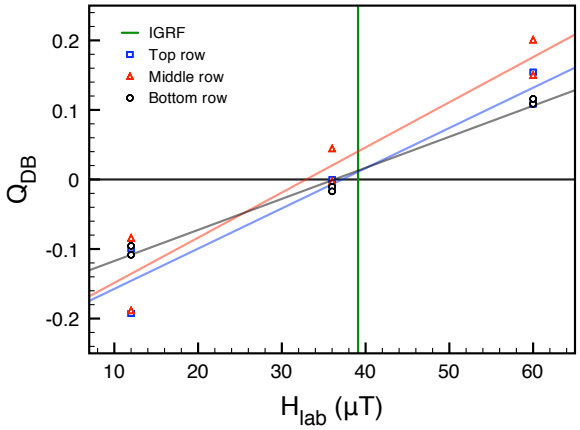

Fig. A5.4c MSP-DB, separated by drilling row. The top row yields the result closest to the IGRF value for site 4.

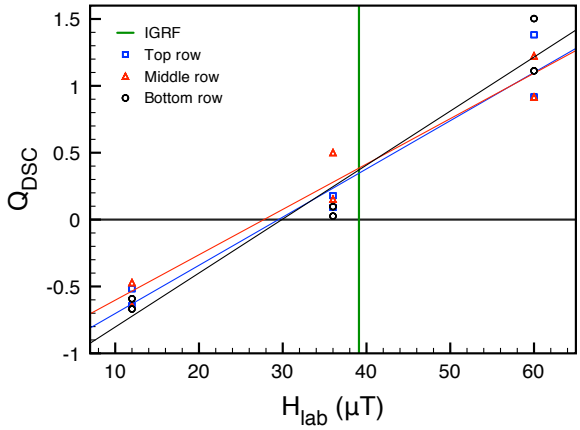

Fig. A5.4d MSP-DSC, separated by drilling row.

H_{lab} (μT)	μ_{DS}	H_{max} (μT)	H_{est} (μT)	ΔH_{est} (μT)	ε_{alt}	Q_{DB}	Q_{FC}	Q_{DSC}	$(\Delta Q_{DS\,c,alt})^2$	$(\Delta Q_{DS\,c,ds})^2$	ΔQ_i	m_2
12	0.051	41.2	33.6	3.7	0.032	-0.193	-0.709	-0.643	0.015	0.001	0.129	+
12	0.041	31.6	24.9	3.2	0.027	-0.100	-0.621	-0.518	0.043	0.004	0.216	+
12	0.040	29.1	22.7	3.1	0.030	-0.084	-0.587	-0.471	0.068	0.005	0.268	+
12	0.055	42.7	33.9	4.3	0.042	-0.188	-0.719	-0.646	0.029	0.002	0.175	+
12	0.029	37.4	29.4	3.8	0.021	-0.096	-0.679	-0.592	0.033	0.003	0.188	+
12	0.026	46.8	36.2	5.0	0.021	-0.108	-0.743	-0.669	0.027	0.002	0.170	+
36	0.116	36.1	30.5	2.8	0.054	-0.000	-0.001	0.179	0.158	0.011	0.411	+
36	0.084	38.1	33.0	2.7	0.046	-0.012	-0.055	0.091	0.122	0.007	0.359	+
36	0.097	36.5	31.2	2.7	0.059	-0.003	-0.013	0.152	0.213	0.009	0.471	+
36	0.086	28.0	24.0	2.1	0.046	0.045	0.287	0.501	0.322	0.015	0.581	+
36	0.059	38.9	32.8	3.1	0.038	-0.010	-0.074	0.097	0.185	0.010	0.442	+
36	0.048	41.9	35.1	3.5	0.032	-0.017	-0.140	0.026	0.165	0.009	0.418	+
60	0.077	34.9	31.3	2.0	0.030	0.109	0.717	0.918	0.192	0.013	0.453	+
60	0.061	27.4	25.2	1.2	0.025	0.154	1.188	1.382	0.254	0.012	0.516	+
60	0.171	30.7	27.0	2.0	0.064	0.201	0.952	1.225	0.618	0.025	0.802	+
60	0.160	35.8	31.3	2.4	0.065	0.150	0.675	0.916	0.455	0.019	0.689	+
60	0.111	33.4	28.4	2.6	0.046	0.109	0.796	1.112	0.638	0.033	0.819	+
60	0.102	28.5	24.0	2.3	0.044	0.116	1.106	1.503	1.225	0.052	1.130	+
Ave	**0.079**	**35.5**	**29.7**		**0.040**				**0.264**	**0.013**	**0.458**	
σ	**0.042**	**5.6**	**4.2**		**0.014**				**0.014**	**0.013**	**0.268**	

Site 5 (1677)

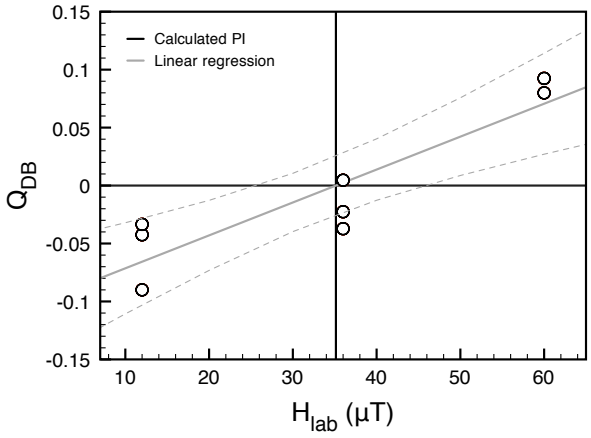

Fig. A5.5a MSP-DB.

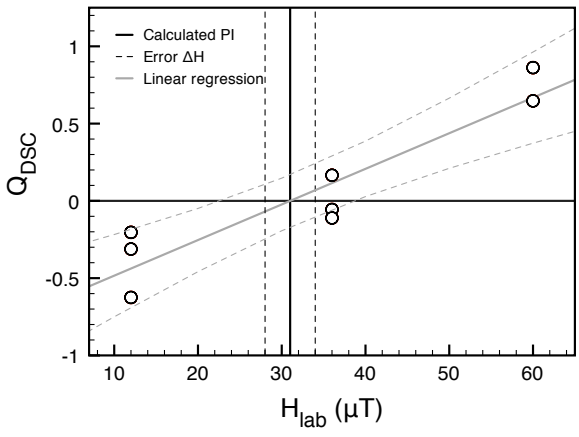

Fig. A5.5b MSP-DSC.

H_{lab} (μT)	μ_{DS}	H_{max} (μT)	H_{est} (μT)	ΔH_{est} (μT)	ε_{alt}	Q_{DB}	Q_{FC}	Q_{DSC}	$(\Delta Q_{DS\,c,alt})^2$	$(\Delta Q_{DS\,c,ds})^2$	ΔQ_i	m_2
12	0.022	39.8	32.0	3.8	0.017	-0.09	-0.699	-0.625	0.025	0.002	0.165	+
12	0.023	20.2	17.4	1.4	0.023	-0.042	-0.406	-0.312	0.093	0.003	0.310	+
12	0.030	18.0	15.1	1.5	0.021	-0.033	-0.334	-0.204	0.088	0.006	0.306	+
36	0.037	34.7	30.9	2.0	0.024	0.005	0.038	0.166	0.107	0.005	0.335	+
36	0.033	41.7	38.1	2.0	0.027	-0.023	-0.136	-0.056	0.060	0.002	0.249	+
36	0.042	44.9	40.5	2.4	0.030	-0.037	-0.198	-0.111	0.054	0.003	0.238	+
60	0.081	37.2	32.2	2.6	0.036	0.08	0.613	0.862	0.355	0.021	0.613	+
60	0.064	21.5	19.7	1.0	0.026	0.186	1.79	2.048	0.592	0.022	0.784	+
60	0.073	40.1	36.4	2.0	0.030	0.092	0.498	0.647	0.114	0.007	0.348	+
60	0.081	12.6	11.6	0.6	0.018	0.315	3.771	4.185	1.079	0.057	1.066	+
Ave	**0.049**	**31.1**	**27.4**		**0.025**				**0.257**	**0.013**	**0.441**	
σ	**0.024**	**11.7**	**10.5**		**0.006**				**0.338**	**0.017**	**0.288**	

Site 6 (1646)

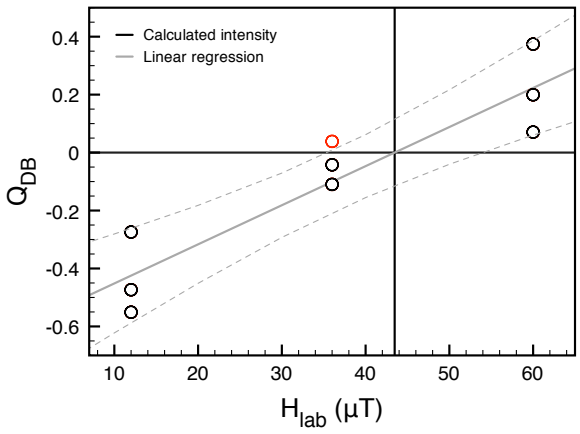

Fig. A5.6a MSP-DB.

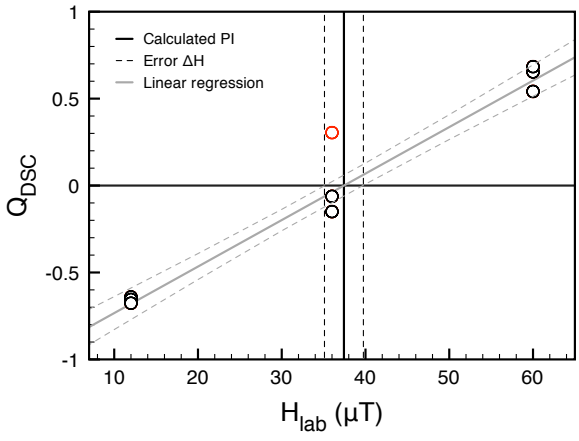

Fig. A5.6b MSP-DSC.

H_{lab} (μT)	μ_{DS}	H_{max} (μT)	H_{est} (μT)	ΔH_{est} (μT)	ε_{alt}	Q_{DB}	Q_{FC}	Q_{DSC}	$(\Delta Q_{DS\,c,alt})^2$	$(\Delta Q_{DS\,c,ds})^2$	ΔQ_i	m_2
12	0.252	38.2	33.4	2.5	0.057	-0.473	-0.686	-0.64	0.003	0.001	0.060	+
12	0.318	38.0	34.8	1.8	0.034	-0.551	-0.684	-0.655	0.001	0.000	0.029	-
12	0.055	42.7	37.1	2.9	0.046	-0.274	-0.719	-0.677	0.013	0.001	0.115	+
36	0.097	31.0	27.6	1.8	0.058	0.039	0.163	0.304	0.187	0.007	0.440	+
36	0.082	47.0	38.4	4.3	0.046	-0.042	-0.234	-0.062	0.144	0.010	0.393	+
36	0.191	48.5	42.3	3.3	0.073	-0.11	-0.258	-0.15	0.053	0.004	0.238	+
60	0.135	45.3	38.9	3.3	0.055	0.071	0.326	0.541	0.244	0.015	0.509	+
60	0.471	38.2	36.3	1.1	0.055	0.374	0.57	0.654	0.047	0.002	0.222	-
60	0.216	39.1	35.6	1.9	0.058	0.199	0.535	0.684	0.125	0.007	0.364	+
Ave	**0.202**	**40.9**	**36.0**		**0.054**				**0.091**	**0.005**	**0.263**	
σ	**0.132**	**5.5**	**4.1**		**0.011**				**0.088**	**0.005**	**0.173**	

Site 7 (1949, sea)

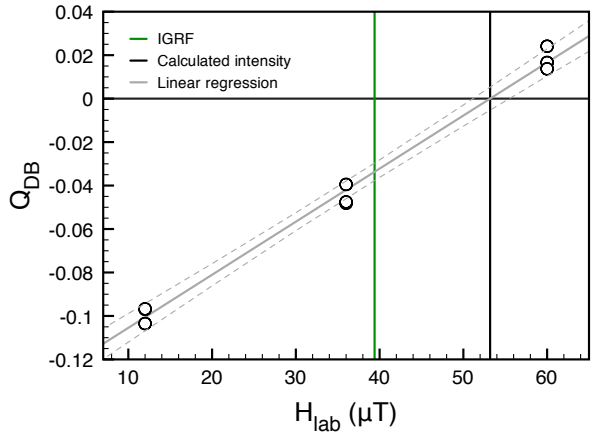

Fig. A5.7a MSP-DB.

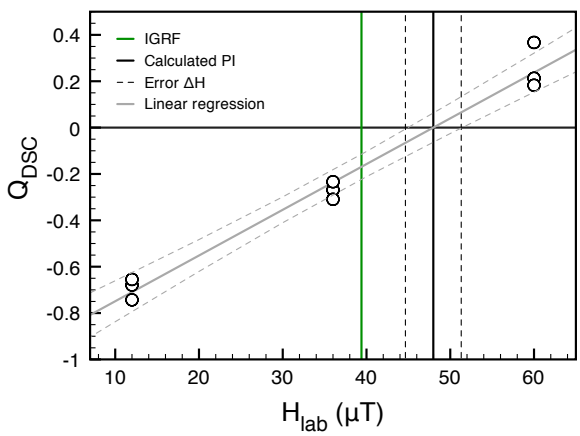

Fig. A5.7b MSP-DSC.

H_{lab} (μT)	μ_{DS}	H_{max} (μT)	H_{est} (μT)	ΔH_{est} (μT)	ε_{alt}	Q_{DB}	Q_{FC}	Q_{DSC}	$(\Delta Q_{DS\,c,alt})^2$	$(\Delta Q_{DS\,c,ds})^2$	ΔQ_i	m_2
12	0.013	56.3	46.7	4.8	0.006	-0.103	-0.787	-0.743	0.002	0.001	0.055	+
12	0.023	49.0	37.4	5.4	0.012	-0.097	-0.755	-0.679	0.011	0.002	0.116	+
12	0.020	42.4	34.8	3.8	0.015	-0.097	-0.717	-0.655	0.017	0.001	0.136	+
36	0.023	54.1	49.2	2.7	0.024	-0.048	-0.335	-0.269	0.052	0.001	0.232	+
36	0.008	53.9	52.1	1.0	0.011	-0.048	-0.332	-0.309	0.011	0.000	0.105	+
36	0.008	48.4	47.0	0.8	0.013	-0.039	-0.256	-0.234	0.014	0.000	0.118	+
60	0.034	48.9	43.9	2.7	0.023	0.024	0.227	0.367	0.157	0.007	0.404	+
60	0.025	53.1	49.5	2.0	0.017	0.017	0.13	0.213	0.049	0.002	0.228	+
60	0.024	54.3	50.7	2.0	0.016	0.014	0.104	0.183	0.040	0.002	0.205	+
Ave	**0.020**	**51.2**	**45.7**		**0.015**				**0.039**	**0.002**	**0.178**	
σ	**0.009**	**4.3**	**6.0**		**0.006**				**0.048**	**0.002**	**0.104**	

Site 8 (1971, east)

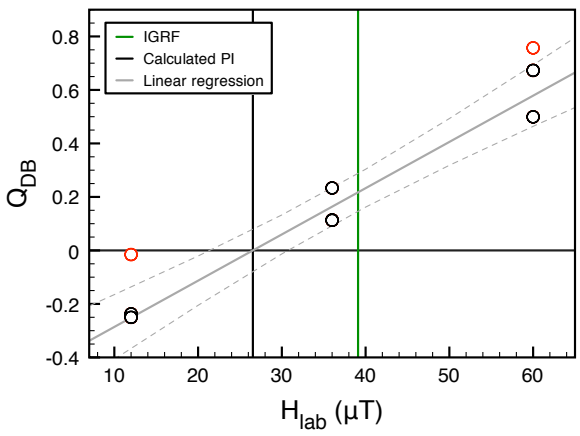

Fig. A5.8a MSP-DB.

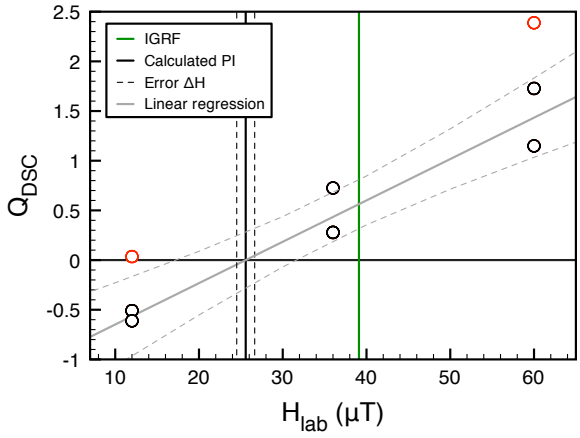

Fig. A5.8b MSP-DSC.

H_{lab} (μT)	μ_{DS}	H_{max} (μT)	H_{est} (μT)	ΔH_{est} (μT)	ε_{alt}	Q_{DB}	Q_{FC}	Q_{DSC}	$(\Delta Q_{DS\,c,alt})^2$	$(\Delta Q_{DS\,c,ds})^2$	ΔQ_i	m_2
12	0.080	27.2	24.5	1.5	0.047	-0.237	-0.559	-0.509	0.013	0.001	0.118	+
12	0.061	13.0	11.6	0.7	0.048	-0.015	-0.074	0.035	0.130	0.004	0.366	+
12	0.056	34.8	30.9	2.1	0.043	-0.25	-0.655	-0.612	0.012	0.001	0.113	+
36	0.084	21.7	20.9	0.5	0.020	0.233	0.655	0.725	0.017	0.002	0.136	+
36	0.141	29.5	28.2	0.8	0.035	0.1139	0.22	0.278	0.017	0.001	0.134	-
36	0.156	29.6	28.2	0.8	0.054	0.1127	0.216	0.278	0.039	0.001	0.200	-
60	0.103	22.6	22.0	0.3	0.032	0.673	1.659	1.727	0.101	0.002	0.321	-
60	0.218	18.7	17.7	0.5	0.017	0.757	2.216	2.388	0.059	0.010	0.262	-
60	0.153	28.9	27.9	0.6	0.022	0.499	1.073	1.149	0.024	0.002	0.160	-
Ave	**0.117**	**25.1**	**23.5**		**0.035**				**0.046**	**0.003**	**0.201**	
σ	**0.054**	**6.7**	**6.2**		**0.014**				**0.043**	**0.003**	**0.094**	

Site 9 (1971, crater)

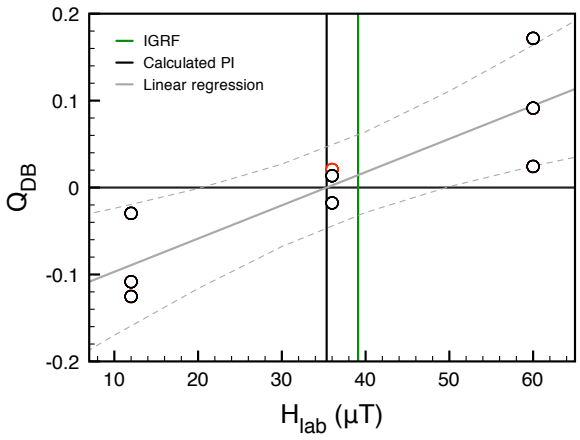

Fig. A5.9a MSP-DB.

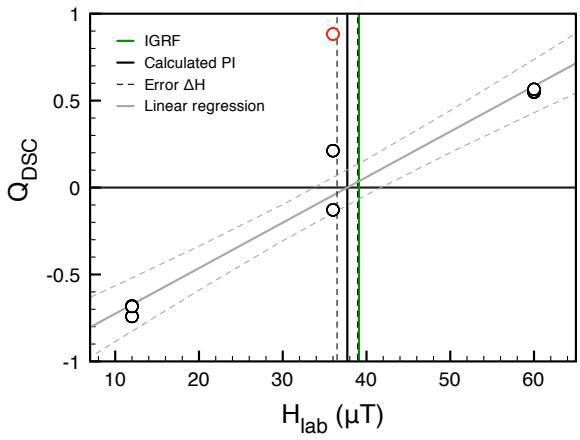

Fig. A5.9b MSP-DSC.

H_{lab} (μT)	μ_{DS}	H_{max} (μT)	H_{est} (μT)	ΔH_{est} (μT)	ε_{alt}	Q_{DB}	Q_{FC}	Q_{DSC}	$(\Delta Q_{DS\,c,alt})^2$	$(\Delta Q_{DS\,c,ds})^2$	ΔQ_i	m_2
12	0.013	54.9	46.4	4.4	0.011	-0.108	-0.781	-0.741	0.008	0.001	0.095	+
12	0.017	43.0	37.6	2.8	0.016	-0.125	-0.721	-0.681	0.010	0.001	0.104	+
12	0.006	49.6	37.9	5.4	0.004	-0.03	-0.758	-0.684	0.019	0.002	0.143	+
36	0.029	32.4	29.7	1.5	0.015	0.014	0.1106	0.2119	0.043	0.003	0.215	+
36	0.018	47.4	41.3	3.2	0.012	-0.018	-0.241	-0.129	0.061	0.004	0.255	+
36	0.016	21.9	19.1	1.5	0.008	0.021	0.643	0.883	0.256	0.019	0.524	+
60	0.025	43.7	38.8	2.6	0.013	0.024	0.375	0.548	0.150	0.010	0.401	+
60	0.046	41.0	38.7	1.3	0.021	0.091	0.462	0.551	0.046	0.003	0.221	+
60	0.074	40.0	38.3	1.0	0.006	0.172	0.5	0.565	0.002	0.001	0.055	+
Ave	**0.027**	**41.5**	**36.4**		**0.012**				**0.066**	**0.005**	**0.224**	
σ	**0.021**	**9.7**	**7.8**		**0.005**				**0.084**	**0.006**	**0.153**	

Site 10 (1.09 ± 0.05 ka)

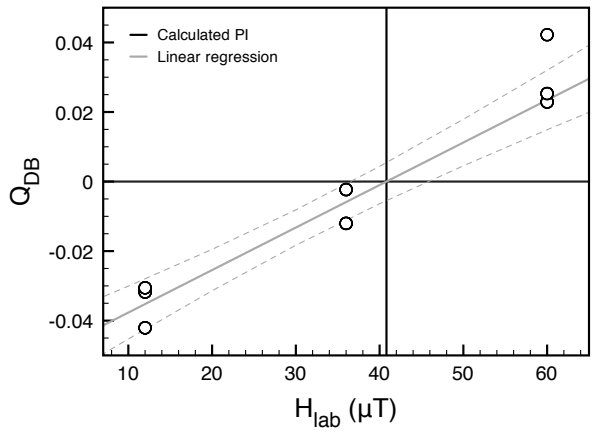

Fig. A5.10a MSP-DB.

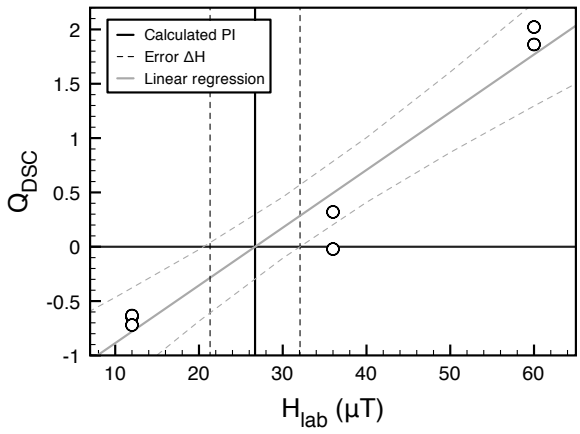

Fig. A5.10b MSP-DSC.

H_{lab} (μT)	μ_{DS}	H_{max} (μT)	H_{est} (μT)	ΔH_{est} (μT)	ε_{alt}	Q_{DB}	Q_{FC}	Q_{DSC}	$(\Delta Q_{DS\,c,alt})^2$	$(\Delta Q_{DS\,c,ds})^2$	ΔQ_i	m_2
12	0.010	49.0	33.6	6.5	0.009	-0.032	-0.755	-0.643	0.079	0.004	0.289	+
12	0.011	49.4	32.7	6.9	0.007	-0.031	-0.757	-0.633	0.051	0.005	0.237	+
12	0.010	63.8	42.9	8.8	0.008	-0.042	-0.812	-0.72	0.032	0.003	0.187	+
36	0.024	39.3	27.3	5.2	0.010	-0.002	-0.083	0.32	0.417	0.054	0.687	+
36	0.024	53.7	36.8	7.2	0.011	-0.012	-0.33	-0.021	0.232	0.032	0.513	+
60	0.025	-0.7	-0.6	0.1	0.014	0.042	-82.66	-106.4	407984	187.526	2019.90	+
60	0.036	28.9	21.0	3.6	0.017	0.023	1.073	1.861	4.306	0.207	2.124	+
60	0.036	27.2	19.9	3.3	0.016	0.025	1.207	2.022	4.676	0.221	2.213	+
Ave	**0.022**	**44.5**	**30.6**		**0.012**				**1.399**	**0.075**	**0.893**	
σ	**0.011**	**13.4**	**8.4**		**0.004**				**2.119**	**0.097**	**0.889**	

Site 11 (1949, crater)

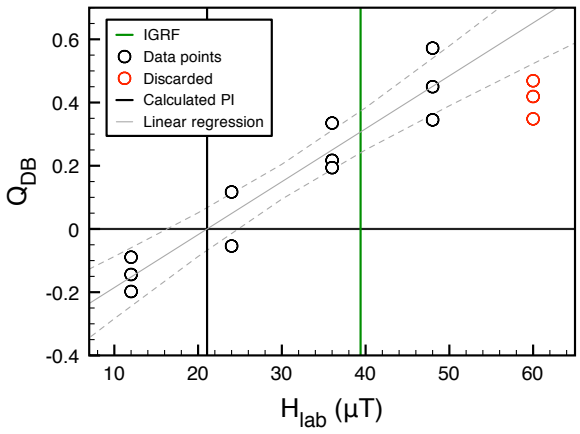

Fig. A5.11a MSP-DB.

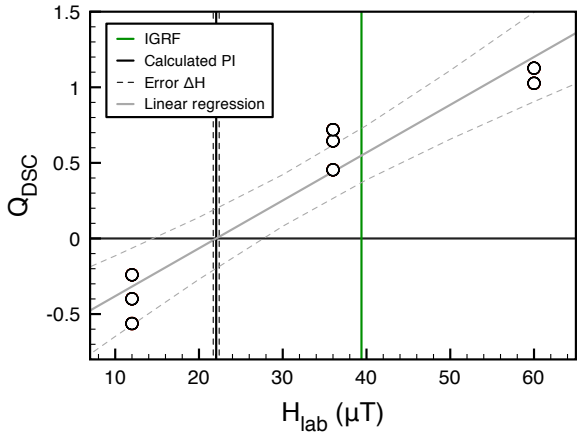

Fig. A5.11b MSP-DSC.

H_{lab} (μT)	μ_{DS}	H_{max} (μT)	H_{est} (μT)	ΔH_{est} (μT)	ε_{alt}	Q_{DB}	Q_{FC}	Q_{DSC}	$(\Delta Q_{DS\,c,alt})^2$	$(\Delta Q_{DS\,c,ds})^2$	ΔQ_i	m_2
12	0.044	30.5	27.4	1.7	0.033	-0.198	-0.607	-0.563	0.012	0.001	0.111	+
12	0.056	22.1	20.0	1.2	0.039	-0.144	-0.457	-0.399	0.022	0.001	0.151	+
12	0.045	16.9	15.8	0.6	0.027	-0.089	-0.289	-0.24	0.014	0.001	0.121	+
24	-	-	-	-	-	-0.054	-	-	-	-	-	
24	-	-	-	-	-	0.117	-	-	-	-	-	
36	0.091	22.3	21.9	0.3	0.015	0.335	0.611	0.645	0.005	0.000	0.074	-
36	0.112	22.2	20.9	0.7	0.029	0.217	0.625	0.72	0.037	0.003	0.200	+
36	0.123	25.8	24.8	0.6	0.031	0.194	0.397	0.454	0.018	0.001	0.138	-
48	-	-	-	-	-	0.345	-	-	-	-	-	
48	-	-	-	-	-	0.45	-	-	-	-	-	
48	-	-	-	-	-	0.572	-	-	-	-	-	
60	0.274	29.9	28.2	1.0	0.017	0.469	1.004	1.126	0.014	0.005	0.136	-
60	0.101	30.8	29.6	0.7	0.003	0.348	0.948	1.027	0.001	0.002	0.052	-
60	0.392	21.0	18.0	1.6	0.021	0.419	1.859	2.342	0.127	0.078	0.453	+
Ave	**0.138**	**24.6**	**23.0**		**0.024**				**0.028**	**0.01**	**0.160**	
σ	**0.118**	**4.9**	**4.8**		**0.011**				**0.039**	**0.025**	**0.118**	

Site 12 (1470-92)

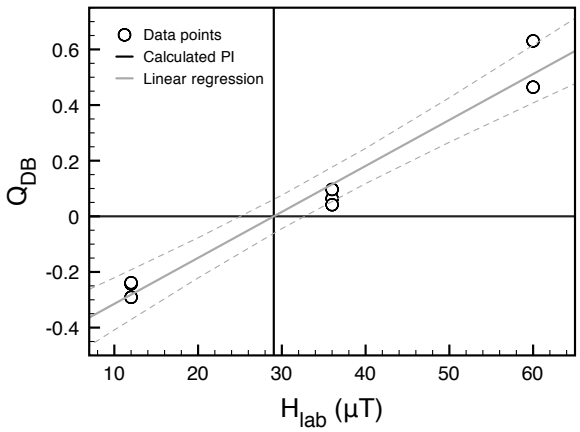

Fig. A5.12a MSP-DB.

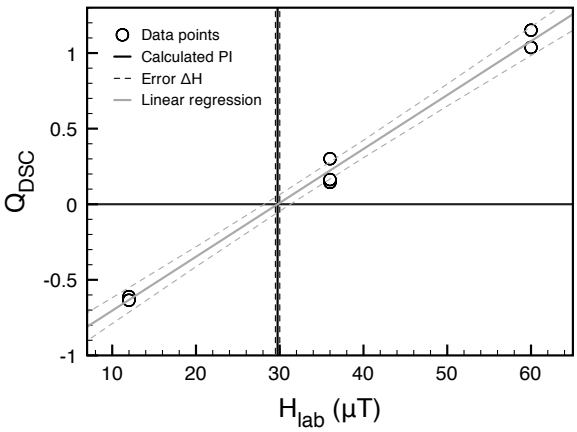

Fig. A5.12b MSP-DSC.

H_{lab} (μT)	μ_{DS}	H_{max} (μT)	H_{est} (μT)	ΔH_{est} (μT)	ε_{alt}	Q_{DB}	Q_{FC}	Q_{DSC}	$(\Delta Q_{DS\,c,alt})^2$	$(\Delta Q_{DS\,c,ds})^2$	ΔQ_i	m_2
12	0.002	31.8	31.7	0.1	0.006	-0.243	-0.623	-0.621	0.000	0.000	0.015	+
12	0.003	31.1	30.9	0.1	0.005	-0.239	-0.614	-0.611	0.000	0.000	0.012	+
12	0.022	34.1	32.9	0.7	0.004	-0.291	-0.648	-0.635	0.000	0.000	0.011	+
36	0.070	32.2	31.4	0.5	0.000	0.064	0.117	0.145	0.000	0.000	0.016	-
36	0.030	31.2	31.0	0.1	0.016	0.097	0.154	0.163	0.002	0.000	0.047	-
36	0.036	29.4	27.7	1.0	0.014	0.042	0.225	0.301	0.018	0.002	0.140	+
60	0.033	29.7	29.5	0.2	0.020	0.464	1.018	1.037	0.018	0.000	0.136	-
60	0.168	28.6	27.9	0.4	0.004	0.631	1.098	1.151	0.000	0.001	0.038	-
Ave	**0.045**	**31.0**	**30.4**		**0.009**				**0.005**	**0.000**	**0.052**	
σ	**0.054**	**1.8**	**1.9**		**0.007**				**0.008**	**0.001**	**0.055**	

Site 13 (1949, east)

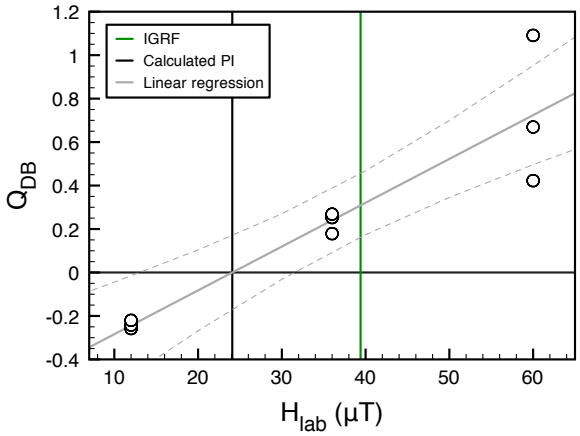

Fig. A5.13a MSP-DB.

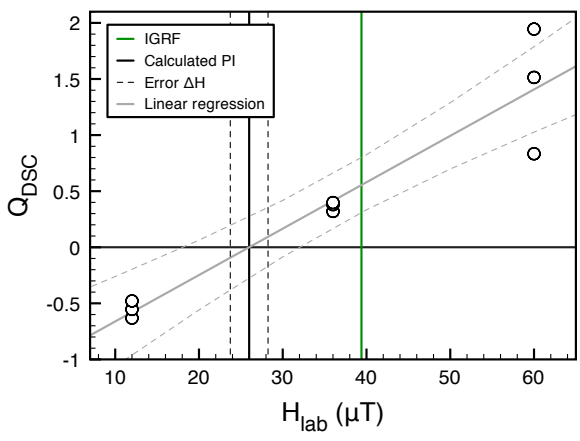

Fig. A5.13b MSP-DSC.

H_{lab} (μT)	μ_{DS}	H_{max} (μT)	H_{est} (μT)	ΔH_{est} (μT)	ε_{alt}	Q_{DB}	Q_{FC}	Q_{DSC}	$(\Delta Q_{DS\,c,alt})^2$	$(\Delta Q_{DS\,c,ds})^2$	ΔQ_i	m_2
12	-0.025	31.1	32.6	0.9	0.036	-0.258	-0.614	-0.632	0.007	0.000	0.084	+
12	-0.030	25.8	26.9	0.7	0.047	-0.242	-0.535	-0.554	0.011	0.000	0.105	+
12	-0.047	21.9	23.0	0.7	0.061	-0.22	-0.453	-0.479	0.018	0.000	0.134	+
36	-0.109	25.9	27.3	0.9	0.080	0.179	0.393	0.32	0.130	0.002	0.363	-
36	-0.168	24.6	26.1	1.0	0.099	0.253	0.465	0.38	0.165	0.002	0.410	-
36	-0.096	25.2	25.8	0.4	0.093	0.268	0.43	0.398	0.112	0.000	0.336	-
60	-0.115	31.4	32.7	0.8	0.099	0.422	0.909	0.834	0.366	0.002	0.607	-
60	-0.222	19.5	20.4	0.5	0.104	1.091	2.073	1.945	1.149	0.005	1.074	-
60	1.631	26.7	23.9	1.5	0.100	0.669	1.247	1.514	0.525	0.024	0.741	-
Ave	**0.091**	**25.8**	**26.5**		**0.080**				**0.276**	**0.004**	**0.428**	
σ	**0.581**	**3.8**	**4.1**		**0.026**				**0.371**	**0.008**	**0.330**	

Site 14 (3.2 ± 0.01 ka)

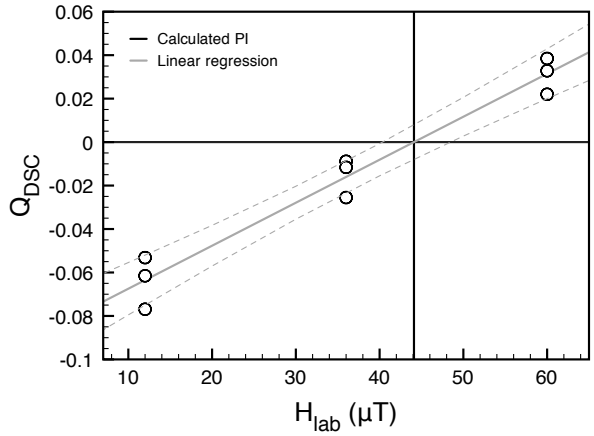

Fig. A5.14a MSP-DB.

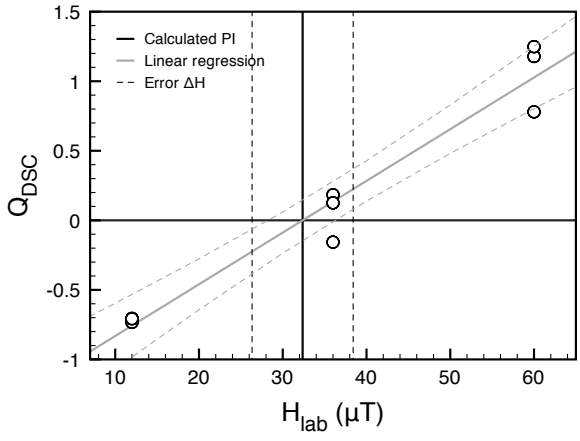

Fig. A5.14b MSP-DSC.

H_{lab} (μT)	μ_{DS}	H_{max} (μT)	H_{est} (μT)	ΔH_{est} (μT)	ε_{alt}	Q_{DB}	Q_{FC}	Q_{DSC}	$(\Delta Q_{DSC,alt})^2$	$(\Delta Q_{DSC,ds})^2$	ΔQ_i	m_2
12	0.016	59.5	40.7	8.0	0.011	-0.062	-0.798	-0.705	0.031	0.003	0.185	+
12	0.009	57.7	44.9	6.1	0.007	-0.053	-0.792	-0.733	0.014	0.001	0.123	+
12	0.025	68.7	41.0	10.5	0.020	-0.077	-0.825	-0.708	0.063	0.005	0.260	+
36	0.042	42.7	30.4	5.4	0.030	-0.009	-0.158	0.183	0.767	0.039	0.898	+
36	0.043	44.2	32.0	5.5	0.029	-0.012	-0.186	0.126	0.571	0.032	0.777	+
36	0.033	57.0	42.7	6.6	0.024	-0.026	-0.368	-0.157	0.256	0.015	0.520	+
60	0.074	36.6	27.5	4.2	0.038	0.038	0.640	1.178	2.019	0.097	1.455	+
60	0.061	35.6	26.7	4.1	0.029	0.033	0.683	1.248	1.972	0.107	1.442	+
60	0.064	44.7	33.7	5.1	0.039	0.022	0.342	0.780	1.504	0.064	1.252	+
Ave	**0.041**	**49.6**	**35.5**		**0.025**				**0.800**	**0.040**	**0.768**	
σ	**0.022**	**11.4**	**6.9**		**0.011**				**0.826**	**0.040**	**0.531**	

Site 15 (1949)

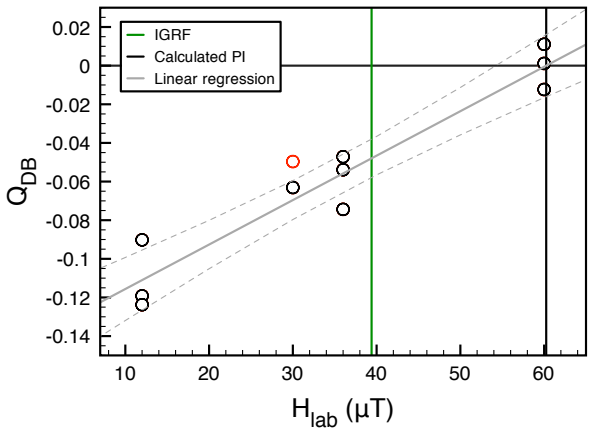

Fig. A5.15a MSP-DB.

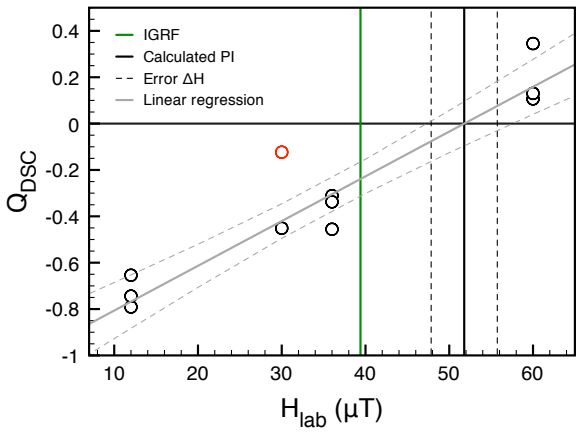

Fig. A2-15b MSP-DSC.

H_{lab} (μT)	μ_{DS}	H_{max} (μT)	H_{est} (μT)	ΔH_{est} (μT)	ε_{alt}	Q_{DB}	Q_{FC}	Q_{DSC}	$(\Delta Q_{DS\,c,alt})^2$	$(\Delta Q_{DS\,c,ds})^2$	ΔQ_i	m_2
12	0.010	66.4	57.5	4.7	0.006	-0.119	-0.819	-0.791	0.002	0.000	0.051	+
12	0.031	44.1	34.7	4.5	0.021	-0.124	-0.728	-0.654	0.020	0.002	0.147	+
12	0.018	65.7	46.9	8.3	0.015	-0.090	-0.817	-0.744	0.024	0.002	0.161	+
30	0.020	62.7	54.7	4.2	0.011	-0.063	-0.521	-0.451	0.013	0.002	0.122	+
30	0.060	38.5	34.2	2.3	0.035	-0.050	-0.220	-0.123	0.051	0.003	0.232	+
36	0.018	73.1	66.1	3.8	0.018	-0.074	-0.507	-0.456	0.024	0.001	0.157	+
36	0.022	57.6	52.3	2.9	0.015	-0.054	-0.375	-0.311	0.019	0.001	0.143	+
36	0.024	63.6	54.3	4.8	0.014	-0.047	-0.434	-0.338	0.032	0.003	0.187	+
60	0.064	54.5	44.6	4.9	0.011	0.011	0.101	0.345	0.034	0.020	0.233	+
60	0.062	66.6	54.2	6.1	0.014	-0.012	-0.099	0.107	0.032	0.014	0.214	+
60	0.035	59.4	53.1	3.4	0.023	0.001	0.009	0.130	0.098	0.005	0.321	+
Ave	**0.033**	**59.3**	**50.2**		**0.017**				**0.032**	**0.005**	**0.179**	
σ	**0.020**	**10.3**	**9.5**		**0.008**				**0.025**	**0.006**	**0.071**	

A.6 Scilab code

To process my MSP data, I wrote a Scilab code that takes the vector intensities measured by the DC SQUID magnetometer and calculates the DB and DSC ratios and a range of parameters. The program calculates and plots linear regressions through the data points and their intersection with the *x*-axis (i.e. the PI). The Scilab function (`dataDSC`) takes the following arguments:

Parameter	Description

m	`aantal` × 16 matrix, consisting of the comma-separated *a, b* and *c* values of the intensities m_0 to m_4 (colums 1 to 15) and the laboratory field H_{lab} (column 16). The data file can be copy-pasted into Scilab:
	`m=[a,b,c,a,b,c,a,b,c,a,b,c,a,b,c,Hlab`
	`a,b,c,a,b,c,a,b,c,a,b,c,a,b,c,Hlab`
	`a,b,c,a,b,c,a,b,c,a,b,c,a,b,c,Hlab];`

aantal	The number of samples
alfa	The value of *α* used in the calculations
plotje	Specifies the way in which Scilab plots the results: 1 Only plots Q_{DB} against the lab field 2 Only plots Q_{DSC} against the lab field other Generates four subplots: Q_{DB}, Q_{DSC}, H_{est} and H_{max} against the lab field
IGRF	IGRF value of the palaeointensity. Only used to generate files that are directly plottable by Plot

The Scilab code calculates the following parameters and writes them to a multicolumn data file:

Column	Output	Description
1	H_{lab}	The lab field
2-6	m_0 **to** m_4	Calculated intensities m_0 to m_4; m_2 is multiplied by $\frac{\mathbf{m}_0 \cdot \mathbf{m}_2}{\lvert\mathbf{m}_0 \cdot \mathbf{m}_2\rvert}$ which equals +1 when m_2 is in the same direction as m_0, but -1 when it is pointing in the opposite direction
7	μ_{DS}	Estimate of the domain state: $\mu_{DS} = \frac{m_1 - m_3}{m_3 - \frac{1}{2}(m_1 + m_2)}$
8	H_{max}	Single-specimen estimate of the maximum palaeointensity: $H_{\max} = \frac{2m_0 - m_1 - m_2}{m_1 - m_2} H_{lab}$

Column	Output	Description
9	H_{est}	Single-specimen estimate of the palaeointensity: $H_{est} = \frac{2m_0 - m_1 - m_2}{(1+2\alpha)m_1 - 2\alpha m_3 - m_2} H_{lab}$
10	ΔH_{est}	Mean deviation from H_{est} when choosing $\alpha = 0.2$ or $\alpha = 0.8$, respectively: $\Delta H_{est} = \left\lvert H_{est}(\alpha = 0.2) - H_{est}(\alpha = 0.8) \right\rvert$
11	ε_{alt}	Relative alteration error: $\varepsilon_{alt} = \left\lvert \frac{m_1 - m_4}{m_1} \right\rvert$
12	Q_{DB}	MSP-DB ratio: $Q_{DB} = \frac{m_1 - m_0}{m_0}$
13	Q_{FC}	*f*-corrected MSP-FC ratio: $Q_{FC} = 2\frac{m_1 - m_0}{2m_0 - m_1 - m_2}$
14	Q_{DSC}	Domain-state-corrected MSP-DSC ratio: $Q_{DSC} = 2\frac{(1+\alpha)m_1 - m_0 - \alpha m_3}{2m_0 - m_1 - m_2}$
15	$(\Delta Q_{DSC,alt})^2$	Alteration error squared: $\left(\Delta Q_{DSC,alt}\right)^2 = \varepsilon_{alt}^2 \sum_{k=1,2,3} \left(m_k \partial_{m_k} Q_{DSC}\right)^2$
16	$(\Delta Q_{DSC,ds})^2$	Domain-state error squared: $\left(\Delta Q_{DSC,ds}\right)^2 = \left(\partial_\alpha Q_{DSC} \Delta\alpha\right)^2 \approx \frac{1}{3}\left(\frac{m_3 - m_1}{2m_0 - m_1 - m_2}\right)^2$
17	ΔQ_I	Total error: $\left(\Delta Q_i\right)^2 = \left(\Delta Q_{DSC,alt}\right)^2 + \left(\Delta Q_{DSC,ds}\right)^2$
18	sgn(m_2)	$\frac{\mathbf{m}_0 \cdot \mathbf{m}_2}{\lvert \mathbf{m}_0 \cdot \mathbf{m}_2 \rvert}$ 1 if m_2 positive, -1 if m_2 is negative (for reference purposes)

And produces the following data files (alphabetically):

File name	Description
`DB_IGRF.dat`	Plottable IGRF intensity for MSP-DB
`DB_int.dat`	Plottable calculated palaeointensity MSP-DB
`DB_LF.dat`	Plottable linear fit for MSP-DB
`DB_plot.dat`	Plottable file containing H_{lab} and Q_{DB}
`DSC_data.dat`	18-column data file containing all data
`DSC_H_est.dat`	Plottable file containing H_{lab}, H_{est} and ΔH_{est}
`DSC_H_max.dat`	Plottable file containing H_{lab} and H_{max}
`DSC_H.dat`	Contains the average values and standard deviations of H_{est} and H_{max}
`DSC_IGRF.dat`	Plottable IGRF intensity for MSP-DSC
`DSC_int.dat`	Plottable calculated palaeointensity MSP-DSC
`DSC_LF.dat`	Plottable linear fit for MSP-DSC
`DSC_max.dat`	Plottable maximum palaeointensity MSP-DSC (PI + ΔH)
`DSC_min.dat`	Plottable minimum palaeointensity MSP-DSC (PI - ΔH)
`DSC_plot.dat`	Plottable file containing H_{lab} and Q_{DSC}
`DSC_reglin.dat`	Contains the parameters for the linear fits of Q_{DB}, Q_{FC} and Q_{DSC} (a, b, σ, the calculated palaeointensity and ΔH
`FC_plot.dat`	Plottable file containing H_{lab} and Q_{FC}

Most of these files are only generated to facilitate easy plotting in programs like Plot. The Q_{DB} file, the linear fit and the calculated and IGRF intensities can be imported in one go and easily edited, instead of doing the fits and drawing the x-intersection manually. The same goes for the MSP-DSC plot. Because the vertical axes are different for the DB and DSC plots, Scilab generates two plottable IGRF files.